

Disorder and interference: localization phenomena

Cord A. Müller* and Dominique Delande†

Chapter 9 in: “Les Houches 2009 - Session XCI: Ultracold Gases and Quantum Information”, C. Miniatura, L.-C. Kwek, M. Ducloy, B. Grémaud, B.-G. Englert, L.F. Cugliandolo, A. Ekert, eds. (Oxford University Press, Oxford 2011)

Contents

1	Introduction	3
1.1	Anderson localization with atomic matter waves	4
2	Transfer-matrix description of transport and Anderson localization in 1d systems	7
2.1	Scattering matrix	7
2.2	Transfer matrix	8
2.2.1	Chaining transfer matrices	9
2.2.2	Incoherent transmission: Ohm’s law	10
2.2.3	Phase-coherent transmission: strong localization	11
2.3	Scaling equations	12
2.4	Fokker-Planck equation and log-normal distribution	12
2.5	Full distribution function	14
3	Scaling theory of localization	16
3.1	What is a scaling theory?	16
3.2	Dimensionless conductance	17
3.3	Scaling in 1D systems	19
3.4	Quasi-1D systems	21
3.5	Scaling in any dimension	21
3.6	$d = 2$	22
3.7	$d = 3$	23
3.8	$d > 3$	24

*Centre for Quantum Technologies, National University of Singapore, Singapore 117543

†Laboratoire Kastler-Brossel, Université Pierre et Marie Curie, Ecole Normale Supérieure, CNRS; 4 Place Jussieu, F-75005 Paris, France

4	Key numerical and experimental results	25
4.1	$d = 1$	25
4.1.1	Localization of cold atoms	25
4.1.2	Localization of light: a ten-Euro experiment	26
4.1.3	Fluctuations	28
4.1.4	The Anderson model: a free (numerical) experiment	28
4.2	$d = 2$	32
4.3	$d = 3$	35
5	Microscopic description of quantum transport	38
5.1	Diagrammatic perturbation theory	38
5.1.1	Quantum propagator	40
5.1.2	Ensemble average	41
5.1.3	Gaussian disorder	42
5.1.4	Speckle	42
5.1.5	Average propagator: self-energy	44
5.2	Intensity transport	47
5.2.1	Density response	47
5.2.2	Quantum intensity transport	48
5.2.3	Diffusion	49
5.2.4	Localization length in 1d systems	50
5.2.5	Weak-localization correction	51
6	Coherent backscattering (CBS)	52
6.1	Theory	53
6.2	Live experiment	57
6.3	Dephasing/decoherence	60
6.3.1	Polarization	61
6.3.2	Residual velocity of the scatterers	62
6.3.3	Non-linear atom-light interaction	63
6.3.4	Internal atomic structure/spin-flip	63
7	Weak localization (WL)	65
7.1	$d = 1$	66
7.2	$d = 2$	66
7.3	$d = 3$	68
7.4	Self-consistent theory of localization	68
7.4.1	$d = 1$	69
7.4.2	$d = 2$	70
7.4.3	$d = 3$	72
8	Kicked rotor	73
8.1	The classical kicked rotor	74
8.2	The Quantum Kicked Rotor	74
8.3	Dynamical Localization	75
8.4	Link between dynamical and Anderson localizations	76
8.5	The quasi-periodically kicked rotor	77

1 Introduction

Although complex systems are ubiquitous in nature, physicists tend to prefer “simple” systems. The reason is of course that simple systems obey simple laws, which can be represented by simple mathematical equations, as expressed by Goldenfeld and Kadanoff [1]:

One of the most striking aspects of physics is the simplicity of its laws. Maxwell’s equations, Schrödinger’s equation, and Hamiltonian mechanics can each be expressed in a few lines. The ideas that form the foundation of our worldview are also very simple indeed: The world is lawful, and the same basic laws hold everywhere. Everything is simple, neat, and expressible in terms of everyday mathematics, either partial differential or ordinary differential equations.

Everything is simple and neat—except, of course, the world.

Even though the world obviously is not simple, many systems can be split, be it only in *Gedanken*, into simple components, each obeying simple laws. This is the viewpoint of standard reductionism, upon which modern science has been built [2]:

The reductionist hypothesis may still be a topic for controversy among philosophers, but among the great majority of active scientists I think it is accepted without question. The workings of our minds and bodies, and of all the animate or inanimate matter of which we have any detailed knowledge, are assumed to be controlled by the same set of fundamental laws, which except under certain extreme conditions we feel we know pretty well.

Reductionism was a key ingredient for the development of physics in the 19th and the first half of the 20th century, when (classical and quantum) mechanics, electromagnetism, relativity, thermodynamics, etc. came to huge success. But is there anything fundamental beyond the simple laws of physics, or can one always reconstruct the properties of composed systems from the workings of their parts? This credo of “constructivism” has been challenged by P. W. Anderson, the author of the preceding quotation and one of the physicists who played a major role in the analysis of complex physical systems:

The ability to reduce everything to simple fundamental laws does not imply the ability to start from those laws and reconstruct the universe. In fact, the more the elementary particle physicists tell us about the nature of the fundamental laws, the less relevance they seem to have to the very real problems of the rest of science, much less to those of society.

The constructionist hypothesis breaks down when confronted with the twin difficulties of scale and complexity. The behavior of large and complex aggregates of elementary particles, it turns out, is not to be understood in terms of a simple extrapolation of the properties of a few particles. Instead, at each level of complexity, entirely new properties appear, and the understanding of the new behaviors requires research which I think is as fundamental in its nature as any other.

which he summarized shortly with:

More Is Different.

It is one aim of these lectures to show—in a restricted context—how intricate the interplay between the small and the large can be in complex systems. We did not yet give a precise definition of the word “complex”. It turns out that the very same word may be used in different contexts with different meanings. In these lectures, we will address a specific example of complexity, viz., *disorder*. In physics as in everyday life, disorder is associated with some lack of regularity. In a disordered material, atoms are not arranged in crystalline periodic patterns, but appear in more or less *random* positions. Randomness occurs because some agents, called “degrees of freedom” by physicist, are not under control, either because we cannot or chose not to control them. It means that we have to learn to deal not with a single specific complex system—that is called a single *realization* of the disorder—but with a whole family of systems whose properties are described in terms of distribution laws, correlation functions, etc. The goal of the game is not to describe as accurately as possible a single system, but rather to predict global properties shared by (almost) all systems, i.e. to acquire knowledge of universal features independent of the precise realization of the disorder. These are instances of the “new behaviors” mentioned by Anderson. And this is also the viewpoint taken long ago by classical thermodynamics where one forfeits the microscopic description of a gas in terms of all positions and momenta, concentrating instead on new concepts like entropy and temperature, which prove to be the relevant, and therefore fundamental, concepts at this level of complexity.

The specific problem we address in these lectures is the problem of transport and localization in disordered systems, when *interference* is present, as characteristic for waves. A wave propagates in some medium (be it vacuum), and interference occurs when different waves overlap, for example scattered from different positions with various wavevectors. The “simple laws” are the wave equation in the homogeneous medium together with a microscopic description of scattering by the impurities. The complex behavior we want to describe is, for example, the propagation of the wave over long distances and for long times. Physical situations of this type cover the propagation of sound in a concert hall with complicated shape, seismic waves multiply scattered inside the earth, electronic matter waves in dirty semiconductor crystals, atomic matter waves in the presence of a disordered potential, etc. In this context, it is good to keep in mind a warning issued by W. Thirring [3]:

It is notoriously difficult to obtain reliable results for quantum mechanical scattering problems. Since they involve complicated interference phenomena of waves, any simple uncontrolled approximation is not worth more than the weather forecast.

1.1 Anderson localization with atomic matter waves

To start with a specific, state-of-the-experimental-art example, imagine a one-dimensional non relativistic particle evolving in a potential $V(z)$ as depicted in Fig. 1. The evolution of the wavefunction $\psi(z, t)$ is given by Schrödinger’s equation:

$$i\hbar\partial_t\psi(z, t) = H\psi(z, t) \tag{1}$$

with the single-particle Hamiltonian

$$H = \frac{p^2}{2m} + V(z). \quad (2)$$

Let us assume that the particle is initially prepared in a Gaussian wave-packet. In the absence of any potential, the Gaussian wave-packet will show ballistic motion, where the center of mass moves at constant velocity while the width increases linearly with time at long times. In the presence of a certain realization $V(z)$ of the disorder, the wave function will take a certain form $\psi(z, t)$. For different realizations, different wave functions will be obtained. But we are not interested in the fine details of each wave function. Rather, we wish to understand the generic, if not universal, properties of the final stationary density distribution $|\psi(z)|^2$ obtained at long times. We will see that not only averages, but also their fluctuations contain important information.

Let us forget for a moment interference effects and try to guess what happens to a classical particle. If its kinetic energy is much larger than the typical strength of the disorder V_0 , the particle will fly above the potential landscape, and the motion is likely to be ballistic on the average. If on the other hand V_0 is larger than the kinetic energy, the particle will be trapped inside a potential well and transport over long distance is suppressed, i.e. localization takes place.

Quantum mechanics modifies this simple picture fundamentally: waves can both tunnel through potential hills higher than the kinetic energy and be reflected even by small potential fluctuations. So the initial wavepacket will split on each potential fluctuation into a transmitted part and a reflected part, no matter how large the kinetic energy with respect to the potential strength may in detail be. After many scattering instances, this looks like a random walk and one naively expects that, on average, the motion at long times will be diffusive, with a diffusion constant depending on some microscopic properties of particle and potential.

This simple model system has been recently realized experimentally [4] using a quasi-one-dimensional atomic matter wave, interacting with an effective optical potential created by a speckle pattern, see Fig. 1. The experimental result is the following: at short times, the wavepacket spreads as expected, but at long times, its average dynamics freeze, and the wavepacket takes a characteristic exponential shape:

$$|\psi(z)|^2 \propto \exp\left(-\frac{|z|}{\xi_{\text{loc}}}\right) \quad (3)$$

where ξ_{loc} is called the localization length.¹ Moreover, if a different realization of the disorder is used (i.e. a microscopically different, but statistically equivalent speckle pattern), an almost identical shape is obtained, meaning that the phenomenon is robust versus a change of the microscopic details.

This surprising phenomenon is known as Anderson localization, sometimes also called strong localization. Although it was predicted on theoretical grounds in the late 50's—most famously by P.W. Anderson himself [5]—it has only been observed directly rather recently. Cold atoms, where an *in situ* direct

¹In the literature, the localization length is defined as the characteristic length for the decay of either $|\psi|^2$ or of $|\psi|$. The two quantities of course differ by a factor 2. Usage of one or the other definition depends on the community, but may also fluctuate from paper to paper. One has to live with this source of disorder.

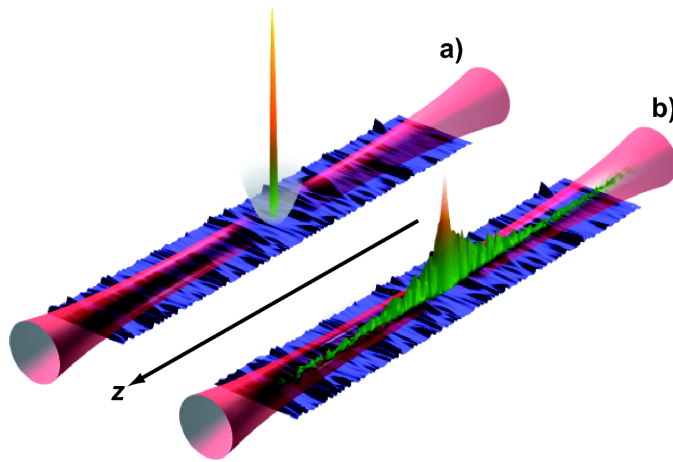


Figure 1: Direct experimental observation of one-dimensional Anderson localization of an atomic matter wave in a disorder potential. The disorder potential (represented in blue in the lower part of the figure) is created by a speckle pattern. (a) An initially localized wave packet (prepared in a harmonic trap at the center) evolves freely, diffuses and eventually freezes at long times in a characteristic exponential shape (b). The pink tube represents the transverse-confinement laser beam that ensures an effectively one-dimensional dynamics. Reprinted from [4] (courtesy of Ph. Bouyer).

observation of the wavefunction is possible, are from that point of view highly valuable.

In these lecture notes, we present an introduction to transport properties in disordered systems, with a strong emphasis on Anderson localization. As an appetizer, we show in section 2 how the one-dimensional case can be exactly solved, providing us with useful physical pictures. We then introduce in section 3 the scaling theory of localization, a typical illustration of the appearance of new concepts and parameters relevant at the long distance and long time scale. After reviewing some of the most important experimental and numerical results in section 4, we develop a microscopic description of quantum transport in section 5, several applications of which are discussed in sections 6, 7 and 8.

Many other, interesting questions will not be touched upon, foremost the impact of *interaction* between several identical particles. However, technically speaking averages over disorder introduce an effective interaction. The relevant diagrammatic approach, originally introduced in the context of quantum electrodynamics, is quite versatile and used equally well to describe, e.g., interacting electrons in solid state samples or interacting atoms in Bose-Einstein condensates. In these lecture notes, we restrict the discussion to non-interacting particles in a disordered medium, but the general framework and the technical tools introduced should provide our readers with solid foundations to follow also more advanced developments. Understanding the combined effects of interaction and disorder has been, still is, and doubtlessly will remain the subject of fascinating research for a long time to come.

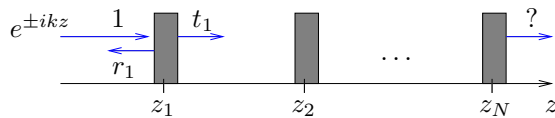


Figure 2: One-dimensional waveguide with randomly placed scatterers. We know the reflection and transmission coefficients r_j and t_j of each scatterer. What is the total transmission T_N across the whole ensemble?

2 Transfer-matrix description of transport and Anderson localization in 1d systems

In order to develop some intuition on transport in disordered systems, it is useful to study solvable models, where one can identify relevant phenomena and mechanisms. It turns out that a one-dimensional system, with the specific choice of δ point scatterers put at random positions, provides such a solvable model, that is moreover sufficiently rich to teach us useful lessons for more realistic disorder and higher dimensions.

Consider therefore a spinless particle confined to a 1d wave-guide geometry by tight transverse trapping to its ground state. Free propagation along the z -direction with wave vector k is described by amplitudes $\psi_{\pm k}(z) = \exp\{\pm ikz\}$. In the following, we discuss the transmission of a single, fixed k -component through a series of obstacles $j = 1, 2, \dots, N$, well separated and placed at randomly chosen distances $\Delta z_j = z_j - z_{j-1}$ as pictured in Fig. 2.

2.1 Scattering matrix

Each obstacle shall be described by a potential $V_j(z)$. To fix ideas, we may assume that it is sufficiently short-ranged to be well approximated by a δ -type impurity, $V_j(z) = V(z - z_j) = \sigma_0 V_0 \delta(z - z_j)$, with an internal length scale σ_0 that is not resolved by the propagating wave, $k\sigma_0 \ll 1$. Furthermore, we suppose that the obstacles are well separated, i.e., their density $n = N/L$ is small compared to the wavelength, $n \ll k$.

Consider first scattering by a single impurity at $z = 0$. We can decompose the wave functions to the left (L, $z < 0$) and right (R, $z > 0$) into left- and right-moving components:

$$\psi_L(z) = \psi_L^{\text{in}} e^{+ikz} + \psi_L^{\text{out}} e^{-ikz} \quad (4)$$

$$\psi_R(z) = \psi_R^{\text{out}} e^{+ikz} + \psi_R^{\text{in}} e^{-ikz}. \quad (5)$$

The outgoing amplitudes are linked to the incident amplitudes by the reflection and transmission coefficients r and t from the left, and r' , t' from the right:

$$r \psi_L^{\text{in}} + t' \psi_R^{\text{in}} = \psi_L^{\text{out}} \quad (6)$$

Writing these relations in matrix form introduces the scattering or S-Matrix:

$$\begin{pmatrix} \psi_L^{\text{out}} \\ \psi_R^{\text{out}} \end{pmatrix} = \mathbf{S} \begin{pmatrix} \psi_L^{\text{in}} \\ \psi_R^{\text{in}} \end{pmatrix} \quad \text{with} \quad \mathbf{S} = \begin{pmatrix} r & t' \\ t & r' \end{pmatrix}. \quad (7)$$

For the present setting of a single-mode wave guide, the reflection and transmission coefficients are complex numbers, and the probabilities for reflection and transmission from the left are $R = |r|^2$ and $T = |t|^2$, respectively, and similarly from the right. In a more general setting of multi-mode scattering with m modes or “channels” on the left and m' modes on the right, r and t are matrices with $m \times m$ and $m' \times m$ entries, respectively. And for example, the total transmission probability “all channels in to all channels out” then reads $T = \sum_{m,m'} t_{m'm} t_{m'm}^* = \sum_{m'} (tt^\dagger)_{m'm'} =: \text{tr}\{tt^\dagger\}$. Within this section, we have only use for the single-channel notation and refer to the literature for the general case [6, 7, 8, 9]

Probability flux conservation requires that \mathbf{S} be unitary, $\mathbf{S}^\dagger = \mathbf{S}^{-1}$. From $\mathbf{S}^\dagger \mathbf{S} = \mathbb{1}$, it follows directly that reflection and transmission probabilities add up to unity: $R + T = 1$ and $R' + T' = 1$. One also finds $r^* t' + t^* r' = 0$ and its complex conjugate $r t'^* + t r'^* = 0$. From this, it follows for the single-channel case that $R = R'$, $T = T'$: the reflection and transmission probabilities are the same from both sides.

Time reversal exchanges the roles of “in” and “out” states. For a time-reversal invariant potential $V(z)$, this implies $\mathbf{S}^* = \mathbf{S}^{-1}$. With unitarity, this is equivalent to $\mathbf{S}^t = \mathbf{S}$ or $t = t'$, a symmetry called *reciprocity*. This setting defines the so-called “orthogonal” symmetry class of random matrix theory. Reciprocity is typically violated in presence of an external magnetic field or magnetic impurities (see Secs. 6.3 and 7 below).

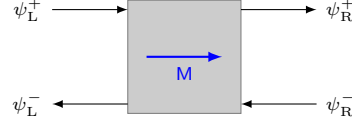
Exercise 1 – Consider an elementary impurity with $V(z) = \sigma_0 V_0 \delta(z)$. Solve the Schrödinger eigenvalue equation $-\psi'' + (2m/\hbar^2)V\psi = k^2\psi$ at fixed k (use the continuity of the free wave function and compute its derivative discontinuity at $z = 0$) and show that the S-Matrix in terms of $f = m\sigma_0 V_0/\hbar^2 k$ is given by [10]

$$\mathbf{S} = \frac{1}{1 + if} \begin{pmatrix} -if & 1 \\ 1 & -if \end{pmatrix}. \quad (8)$$

2.2 Transfer matrix

If we now have several impurities in series, in principle the total transmission can be calculated from the S-matrix of the whole system. But the total S-matrix is not simply linked to the individual S-matrices. Since the transmission depends on the incident amplitudes from both left and right, adding a scatterer requires to recompute the entire sequence. So instead of distinguishing in/out amplitudes, one prefers to decompose the wave function into right-/left moving amplitudes, respectively: $\psi(z) = \psi^+ e^{+ikz} + \psi^- e^{-ikz}$, and this on both sides R/L of the obstacles. The transfer matrix \mathbf{M} then maps the amplitudes from

the left side of the obstacle to the right:



or $\begin{pmatrix} \psi_R^+ \\ \psi_R^- \end{pmatrix} = \mathbf{M} \begin{pmatrix} \psi_L^+ \\ \psi_L^- \end{pmatrix}. \quad (9)$

One can easily determine its matrix elements in terms of t, t', r, r' . For instance, $\psi_L^{\text{out}} = r\psi_L^{\text{in}} + t'\psi_R^{\text{in}}$ rewrites as $\psi_L^- = r\psi_L^+ + t'\psi_R^-$, which we can immediately solve for $\psi_R^- = \frac{1}{t'}\psi_L^- - \frac{r}{t'}\psi_L^+$, and similarly for ψ_R^+ . Eliminating r', t' with unitarity relations in favor of r, t and their complex conjugates yields a simple form:

$$\mathbf{M} = \begin{pmatrix} 1/t^* & -r^*/t^* \\ -r/t & 1/t \end{pmatrix}. \quad (10)$$

Exercise 2 – Check the following interesting properties of the transfer matrix:

- (i) $\det \mathbf{M} = 1$.
- (ii) Current conservation (unitarity of \mathbf{S}) implies now that $\mathbf{M}\sigma_z\mathbf{M}^\dagger = \sigma_z$, with $\sigma_z = \begin{pmatrix} 1 & 0 \\ 0 & -1 \end{pmatrix}$ the third Pauli matrix.
- (iii) Equivalently, $\mathbf{M}^{-1} = \sigma_z\mathbf{M}^\dagger\sigma_z$.
- (iv) $(\mathbf{M}^\dagger\mathbf{M})^{-1} = \sigma_z\mathbf{M}^\dagger\mathbf{M}\sigma_z$. Thus, the hermitian matrices $(\mathbf{M}^\dagger\mathbf{M})^{-1}$ and $\mathbf{M}^\dagger\mathbf{M}$ have the same (real) eigenvalues. Verify this property by computing the eigenvalues directly using (10). Since these eigenvalues must also be each other's inverses, they can only be of the form $\lambda_+ = 1/\lambda_- = e^{2x}$.
- (v) As a matrix, $2 + (\mathbf{M}^\dagger\mathbf{M})^{-1} + \mathbf{M}^\dagger\mathbf{M} = 4/T$. Thus, the total transmission probability is $T = 1/(\cosh x)^2$.

2.2.1 Chaining transfer matrices

By construction, the transfer matrix maps the amplitudes from left to right across each scatterer. Therefore, the total transfer matrix across N scatterers is obtained by multiplying them:

$$\mathbf{M}_{12\dots N} = \mathbf{M}_N \dots \mathbf{M}_2\mathbf{M}_1. \quad (11)$$

Consider the simplest case of two obstacles $j = 1, 2$ in series, for which $\mathbf{M}_{12} = \mathbf{M}_2\mathbf{M}_1$. After matrix multiplication, one finds the transmission coefficient

$$t_{12} = \frac{t_1 t_2}{1 - r_1' r_2} \quad (12)$$

This transmission amplitude contains the entire series of repeated internal reflection between the two scatterers: $t_{12} = t_2 t_1 + t_2 r_1' r_2 t_1 + t_2 (r_1' r_2)^2 t_1 + \dots$. The transmission probability reads

$$T_{12} = \frac{T_1 T_2}{|1 - \sqrt{R_1 R_2} e^{i\theta}|^2} \quad (13)$$

where θ is the total phase accumulated during one complete internal reflection. Since the scatterers are placed with a random distance $k\Delta z \gg 2\pi$, the phase θ

will also be randomly distributed in $[0, 2\pi]$, independently of the details of the random distribution of distance between consecutive scatterers or their reflection phases. One can calculate expectation values of any function of θ by

$$\langle f(\theta) \rangle = \int_0^{2\pi} \frac{d\theta}{2\pi} f(\theta). \quad (14)$$

But as we will see in the following, a very important question is: “what quantity $f(\theta)$ should be averaged?”

2.2.2 Incoherent transmission: Ohm’s law

The most natural thing seems to average directly the transmission probability (13). One finds

$$\langle T_{12} \rangle = \frac{T_1 T_2}{1 - R_1 R_2}. \quad (15)$$

The same transmission probability is obtained for a purely classical model where only reflection and transmission *probabilities* are combined:

Exercise 3 – Show that the rule (15) is also obtained if one uses an S-matrix propagating probabilities instead of amplitudes, $\hat{S} = \begin{pmatrix} R & T \\ T & R \end{pmatrix}$, by determining the corresponding transfer matrix \hat{M} and chaining it.

In this case, the distance Δz of ballistic propagation between the two scatterers is completely irrelevant, and T_{12} is given by (15). This classical description applies to systems that are subject to strong decoherence, where the phase of the particle is completely scrambled by coupling to an external degree of freedom, while traveling between scatterers 1 and 2.

The so-called element resistance of the obstacles, $(1 - T)/T$, calculated with the classical transmission, is additive:

$$\frac{1 - T_{12}}{T_{12}} = \frac{1 - T_1}{T_1} + \frac{1 - T_2}{T_2}. \quad (16)$$

Therefore, the classical resistance across N identical impurities distributed with linear density $n = N/L$ along a wire of length L grows like

$$\frac{R}{T}(L) = N \frac{R_1}{T_1} =: \frac{L}{l_1} \quad (17)$$

where $l_1 = T_1/(nR_1)$ is a length characterizing the backscattering strength of a single impurity.

Within the context of electronic conduction, the result (17) is known as Ohm’s law, stating that the total classical resistance of a wire grows linearly with its length L . Obviously, averaging the transmission itself at each step has wiped out completely the phase-coherence and left us with a purely classical transport process. This process can be formulated equivalently as a persistent random walk on a lattice where the particle has uniform probability T_1 to continue in the same direction at each time step and probability R_1 to make a U-turn. For long times, this random walk leads to diffusive motion with diffusion constant [11]

$$D = v l_0 \frac{T_1}{2R_1}. \quad (18)$$

Here v is the velocity of the particle and $l_0 = 1/n$ the distance between consecutive scatterers. Since the diffusion constant is related to the transport mean free path l by the general relation $D = vl/d$, with $d = 1$ the dimension of the system, one can identify l_1 as twice the transport mean free path, $l_1 = 2l$.

2.2.3 Phase-coherent transmission: strong localization

The relation (15) cannot be easily generalized to more than two scatterers. Indeed, already for three scatterers, the average of the complicated product of transmission matrices even over independent, random phases θ_{12} and θ_{23} becomes very complicated. In order to predict the behavior of transmission across long samples, it is advantageous to find a quantity that is additive as new scatterers are added to the wire. There is such a quantity that becomes additive under ensemble-averaging, namely the so-called extinction coefficient $\kappa = -\ln T = |\ln T|$. When averaging the logarithm of (13), the denominator drops out since

$$\int_0^{2\pi} \frac{d\theta}{2\pi} \ln \left| 1 - \sqrt{R_1 R_2} e^{i\theta} \right| = 0 \quad (19)$$

due to the analyticity of the complex logarithm for all $0 \leq R_1 R_2 < 1$. Thus, one immediately finds that the average extinction across two consecutive scatterers is strictly additive:

$$\langle \ln T_{12} \rangle = \ln(T_1) + \ln(T_2). \quad (20)$$

The generalization to many scatterers is now easy because $\langle \ln T \rangle$ is additive: the total extinction of a channel of length L grows on average like $|\langle \ln T \rangle| = nL |\ln T_1|$. With this scaling behavior, one obtains that the log-averaged transmission

$$\exp\{\langle \ln T \rangle\} = e^{-L/\xi_{\text{loc}}} \quad (21)$$

drops exponentially fast with increasing sample length L . In the absence of absorption, this is a hallmark of strong localization by disorder, and we have found the localization length $\xi_{\text{loc}} = 1/(n |\ln T_1|)$. In a weak scattering situation where $nl_1 = T_1/R_1 \gg 1$, we approximate $|\ln T_1| \approx 1/nl_1$ and thus find the localization length as $\xi_{\text{loc}} = l_1 = 2l$.

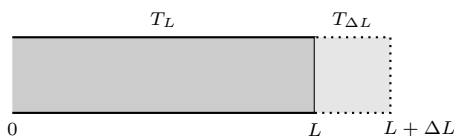
What is the meaning of the log-averaged transmission (21)? It is important to realize that the transmission T as a function of the microscopic realization of disorder is a *random variable*. We will show in the following sections that T itself is not a self-averaging quantity, meaning that its average $\langle T \rangle$ has no resemblance to the most likely found value of T , called the *typical* transmission T_{typ} . We will shortly see that for long samples, the probability distribution of $\ln T$ is very close to a normal distribution (see (32) below), which is centered at $\langle \ln T \rangle = \ln T_{\text{typ}}$. And since the logarithm is monotonic, the *most probable value* of the transmission is indeed $T_{\text{typ}} = \exp\{\langle \ln T \rangle\} = e^{-L/\xi_{\text{loc}}}$.

How does one go about to identify a properly self-averaging quantity in the first place? — By observing that the transmission matrices of several obstacles multiply, see eq. (11). Thus, their logarithm is additive: $\ln M_{12\dots N} = \sum_{j=1}^N \ln M_j$. Summing a large number of these random log-transmission matrices therefore realizes a variant of the central limit theorem, from which we know that the limiting probability distribution is a normal (Gaussian) distribution with a width that decreases with the number of addends. And really, many

of the rigorous results available for (quasi-)1D Anderson localization make use of Furstenberg's theorem on products of random matrices [12]. Thus, the extinction or log-averaged transmission is indeed a good candidate for a self-averaging quantity.

2.3 Scaling equations

In order to substantiate the previous arguments, we should find the full distribution function $P(T, L)$ that permits to derive expectation values for arbitrary functions of T at length L . This distribution function can be found exactly by solving recursion relations that describe how the transmission is changed when a small bit ΔL is added to a sample of length L :



We know already that the transfer matrices multiply, $M_{L+\Delta L} = M_{\Delta L}M_L$. The composition law (13) then gives

$$T_{L+\Delta L} = \frac{T_L T_{\Delta L}}{|1 - e^{i\theta} \sqrt{R_L R_{\Delta L}}|^2}. \quad (22)$$

The idea is now to study the change in the expectation values of T as the “time” $t = L/l_1$ grows. For this, we assume that the added part ΔL is long enough such that an independent disorder average $\langle \dots \rangle_{\Delta L}$ in this section is meaningful. We also assume that the scatterers are weak such that the backscattering probability remains small:

$$R_{\Delta L} = \Delta L/l_1 =: \Delta t \ll 1. \quad (23)$$

These assumptions are verified if ΔL is of the order of $n^{-1} = l_1 R_1$ with a single weak scatterer on average. We may now expand (22) using $T_{\Delta L} = 1 - \Delta t$ to leading order in Δt , finding for the change

$$\Delta T = T_{L+\Delta L} - T_L = T_L \left[2\sqrt{R_L \Delta t} \cos \theta + (4R_L \cos^2 \theta - 1 - R_L) \Delta t \right]. \quad (24)$$

Thus, to order Δt , we find by averaging $\langle \dots \rangle_{\Delta L} = \langle \dots \rangle_{\theta}$ that

$$\frac{\langle \Delta T \rangle_{\theta}}{\Delta t} = -T_L^2, \quad \frac{\langle (\Delta T)^2 \rangle_{\theta}}{\Delta t} = 2T_L^2(1 - T_L), \quad \frac{\langle (\Delta T)^n \rangle_{\theta}}{\Delta t} = 0 \quad (n \geq 3) \quad (25)$$

So only the first two moments of fluctuations contribute. From the first relation we can read off that the transmission decreases with increasing length, an expected result. But the second relation shows that the relative fluctuations, while small in the beginning where $1 - T = R \ll 1$, will grow for long samples where $T \ll 1$.

2.4 Fokker-Planck equation and log-normal distribution

The above equations (25) describe a random quantity $T(t)$ whose first two moments obey the equations $\partial \langle T \rangle / \partial t = \langle A(T) \rangle$ and $\partial \langle T^2 \rangle / \partial t = \langle 2TA(T) + B(T) \rangle$

with $A(T) = -T^2$ and $B(T) = 2T^2(1 - T)$. Here, we use the continuous notations $\Delta t \rightarrow dt$ and $\Delta T \rightarrow dT$ while bearing in mind the coarse-grained character of the averaged quantities. The theory of Brownian motion [13] then teaches us that the probability distribution $P(T, t)$ of T at time t obeys the Fokker-Planck equation

$$\partial_t P = -\partial_T[AP] + \frac{1}{2}\partial_T^2[BP]. \quad (26)$$

This equation of motion can be seen as a continuity equation, $\partial_t P + \partial_T J = 0$, for the locally conserved probability density with current $J = AP - \frac{1}{2}\partial_T(BP)$. Here, A describes the drift, whereas $B/2$ plays the role of a diffusion constant.

By standard terminology, the Fokker-Planck equation (26) is called “non-linear”, because $B(T)$ and $A(T)$ depend non-linearly on T . By changing the variable, one can try to simplify these coefficients. A first option consists in using $T = 1/(\cosh x)^2$ (remember exercise 2(v)). In the remainder of this section, let us explore the consequences of this choice. Knowing that the change of variables for a probability density requires

$$P(T, t)dT = P((\cosh x)^{-2}, t) \left| \frac{dT}{dx} \right| dx = \tilde{P}(x, t)dx, \quad (27)$$

we find the corresponding Fokker-Planck equation:

$$\partial_t \tilde{P}(x, t) = -\frac{1}{2}\partial_x [\coth(2x)\tilde{P}] + \frac{1}{4}\partial_x^2 \tilde{P} \quad (28)$$

with initial condition $\tilde{P}(x, 0) = \delta(x)$. With this choice of variable, the second derivative describing the fluctuations has become most simple. Although this equation is still (too) difficult to solve exactly, we can extract the limiting distribution for long samples in the limit $t \gg 1$ as follows. First we rewrite the equation as

$$\left[\partial_t + \frac{1}{2} \coth(2x)\partial_x \right] \tilde{P}(x, t) = \frac{1}{(\sinh 2x)^2} \tilde{P} + \frac{1}{4}\partial_x^2 \tilde{P} \quad (29)$$

We may interpret the derivatives on the left hand side as a Lagrangian derivative $\partial_t + \dot{x}_0 \partial_x = D_t$ in a co-moving frame defined by $\dot{x}_0(t) = \frac{1}{2} \coth(2x_0)$, which is solved by $x_0(t) = \frac{1}{2} \operatorname{arcosh}(e^t) \approx \frac{1}{2}t$, for large t . Developing all terms for small deviations $\Delta = x - x_0(t)$ from this point of reference, we find a very simple equation for $\tilde{F}(\Delta, t) = \tilde{P}(x_0(t) + \Delta, t)$:

$$\partial_t \tilde{F}(\Delta, t) = \frac{1}{4}\partial_\Delta^2 \tilde{F}(\Delta, t). \quad (30)$$

This is the elementary diffusion equation, and the solution, perhaps best known as the heat kernel, is readily obtained by Fourier transformation:

$$\tilde{F}(\Delta, t) = \frac{1}{2\sqrt{\pi t}} \exp \left\{ -\frac{\Delta^2}{4t} \right\} \quad (31)$$

Going back to the transmission using $\ln T = -2x$ valid for large x , we thus find the limiting distribution

$$F_{\log\text{-norm}}(\ln T, t) = \frac{1}{2\sqrt{\pi t}} \exp \left\{ -\frac{(\ln T + t)^2}{4t} \right\} \quad (32)$$

for small deviations around the most probable value $\ln T_0(t) = -2x_0(t) = -t$. We have successfully demonstrated that indeed the logarithm of the transmission is a normally distributed random quantity. It is characteristic for disordered channels that the two defining moments

$$|\langle \ln T \rangle| = t, \quad \text{var}(\ln T) = \langle (\ln T)^2 \rangle - \langle \ln T \rangle^2 = 2t \quad (33)$$

are determined by a single parameter, namely the length $t = L/2l = L/\xi_{\text{loc}}$ of the one-dimensional wire in units of the localization length. Clearly, the relative fluctuations $\text{var}(\ln T)/\langle \ln T \rangle^2 = 2/t$ decay with system size. Thus we are assured that the transmission logarithm is a self-averaging quantity, with moreover a normal probability distribution whose most probable value is equal to the mean.

But careful! Even in the limit $t \gg 1$, this does unfortunately *not* imply that one may use the log-normal distribution (32) indiscriminately to calculate moments of the transmission. A striking counterexample is

$$\langle T \rangle_{\text{log-norm}} = \langle e^{\ln T} \rangle_{\text{log-norm}} = \int dy F_{\text{log-norm}}(y, t) e^y = 1 \quad (\text{wrong}), \quad (34)$$

and quite obviously so. What goes wrong here? We will have a second look at the end of the next section once we know the exact solution.

2.5 Full distribution function

Another choice of variable is $\rho = T^{-1}$, the dimensionless total resistance of the channel. The Fokker-Planck equation (26) for its probability distribution $W(\rho, t) = P(\rho^{-1}, t)\rho^{-2}$ reads

$$\partial_t W = \partial_\rho [\rho(\rho - 1)\partial_\rho W] \quad (35)$$

with initial condition $W(\rho, 0) = \delta(\rho - 1)$, i.e., a wire of zero length has perfect transmission. The solution can be calculated in closed form [14]:

$$W(\rho, t) = \frac{\exp\{-t/4\}}{\sqrt{\pi}t^{3/2}} \int_{\text{arccosh}\sqrt{\rho}}^{\infty} \frac{\exp\{-y^2/t\}d(y^2)}{\sqrt{(\cosh y)^2 - \rho}}. \quad (36)$$

Figure 3 shows how the distribution function $F(\kappa, t) = W(e^\kappa, t)e^\kappa$ for the extinction $\kappa = \ln \rho = -\ln T$ moves from a δ -distribution with growing system size t to the log-normal distribution (32), drawn as a dashed line at $t = 10$.

The full distribution function permits to calculate all moments $\langle \rho^{-n} \rangle = \langle T^n \rangle$ of the transmission [14]. For $t \gg 1$, one finds the asymptotic expression

$$\langle T^n \rangle = \frac{\pi^{3/2}\Gamma(n - \frac{1}{2})^2}{2\Gamma(n)^2} t^{-3/2} e^{-t/4}, \quad (37)$$

showing that *all* moments decay with the same dependence $t^{-3/2}e^{-t/4}$. The first two moments are then

$$\langle T \rangle = \frac{\pi^{5/2}}{2} t^{-3/2} e^{-t/4}, \quad \langle T^2 \rangle = \frac{1}{4} \langle T \rangle \ll 1. \quad (38)$$

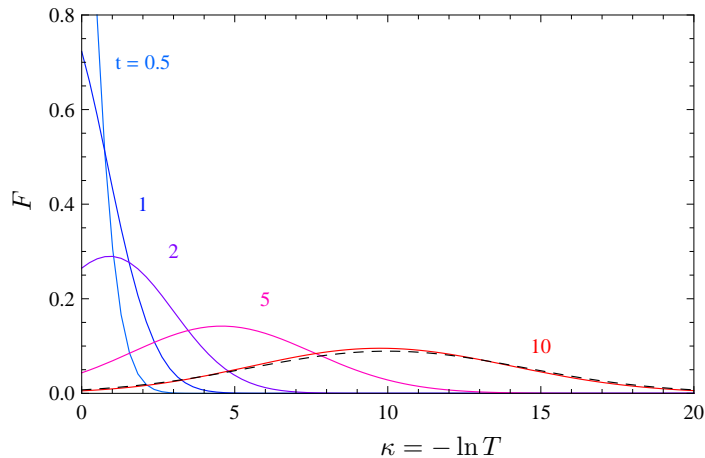


Figure 3: Probability distribution function $F(\kappa, t) = W(e^\kappa, t)e^\kappa$ for the extinction $\kappa = \ln \rho = -\ln T$ across a one-dimensional channel of length $t = L/\xi_{\text{loc}} = 0.5, 1, 2, 5, 10$. Dashed line at $t = 10$: log-normal distribution (32).

Although the average transmission and its fluctuations decay exponentially, as expected for a strongly localizing system, the *relative* fluctuations of the transmission itself grow very quickly: $\text{var}(T)/\langle T \rangle^2 \propto t^{3/2}e^{t/4}$.

And why does the blind application (34) of the limiting log-normal distribution (32) predict $\langle T \rangle_{\text{log-norm}} = 1$ instead of the correct decrease (38)? Well, in (34), we have used the normal distribution on the entire real axis for $y = \ln T$, without paying attention to the constraint that the physically admissible transmission is $T \leq 1$. To take this into account, a popular recipe consists in using a *truncated* log-normal distribution on the half-line $\kappa \geq 0$ [9, 15]

$$F_{\text{log-norm}}^+(\kappa, t) = \frac{\Theta(\kappa)}{C(t)\sqrt{\pi t}} \exp\left\{-\frac{(\kappa - t)^2}{4t}\right\} \quad (39)$$

with a normalization $C(t) = 1 + \text{erf}(\sqrt{t}/2) \approx 2$. The moments of this distribution depend entirely on the value at truncation, $\lim_{\kappa \rightarrow 0^+} F_{\text{log-norm}}^+(\kappa, t) = (2\sqrt{\pi})^{-1}t^{-1/2}e^{-t/4}$, that is the probability for perfect transmission $T = 1$. The transmission moments for $t \gg 1$ are predicted to be

$$\langle T^n \rangle_{\text{log-norm}}^+ \approx \frac{1}{(2n-1)\sqrt{\pi}} t^{-1/2} e^{-t/4}. \quad (40)$$

Comparing them with the exact moments (37), we see that the truncated log-normal distribution can describe the *leading exponential decay*, but fails to capture the algebraic dependence correctly. Mathematically, this is due to the fact that the log-normal distribution overestimates the probability of perfect transmission $T = 1$, which is really only $W(1, t) = (\pi^{3/2}/2)t^{-3/2}e^{-t/4}$ for $t \gg 1$.

On physical grounds, this limited applicability of the log-normal distribution emphasizes the difficulties one faces when dealing with broad distributions. Figure 4 shows the transmission probability distributions at different lengths $t = L/l$. It is instructive to look at the last curve for the altogether moderate

system size $t = 10$. The *most probable* or “typical” value for the transmission is quite small, $T_{\text{typ}} = \exp\{\langle \ln T \rangle\} = e^{-10} \approx 4.5 \cdot 10^{-5}$. The exact *average value* is much bigger, $\langle T \rangle \approx 1.06 \cdot 10^{-2}$, indicating that this average is to a large extent determined by very rare events with anomalously large transmission. The truncated log-normal distribution, shown in dashed, overestimates the frequency of large transmissions and predicts $\langle T \rangle \approx 1.28 \cdot 10^{-2}$.

Let us close this section by emphasizing once more that the typical transmission — averaged over all possible relative phases accumulated between consecutive scatterers — displays exponential decay at large distance as stated in eq. (21). This is in sharp contrast to the classical transmission (17), where classical probabilities, not amplitudes, are combined to an algebraic decay. Clearly, averaging over disorder implies averaging over quantum mechanical phases globally, but is not equivalent to removing phase-coherence and interference effects locally from the very start. This is a striking example of a *mesoscopic* effect, a rather counter-intuitive phenomenon, where microscopic phase coherence has macroscopic physical consequences that survive averaging over quenched disorder.

3 Scaling theory of localization

3.1 What is a scaling theory?

A scaling theory describes the relevant properties of physical systems by considering their behavior under changes of size $L \mapsto bL$. Quantitative scaling arguments were invented in quantum field theory in the context of renormalization. Scaling arguments became widely popular in statistical physics by the mid-60’s for describing phase transitions and critical phenomena [16]. The immense success of renormalization-group techniques developed in the 70’s [17] rapidly radiated to the field of disorder-induced phase transitions that Ander-

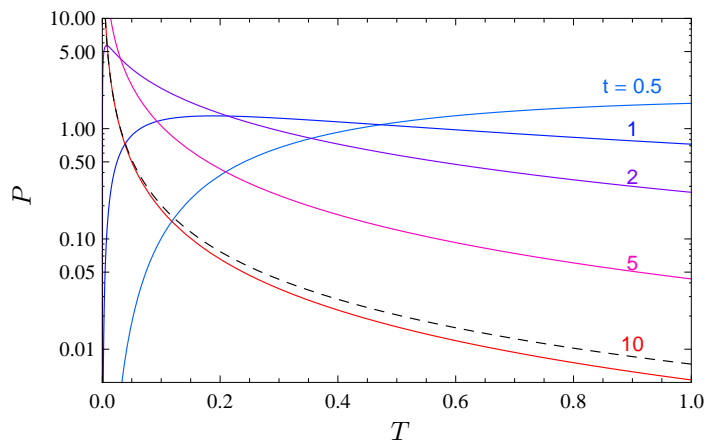
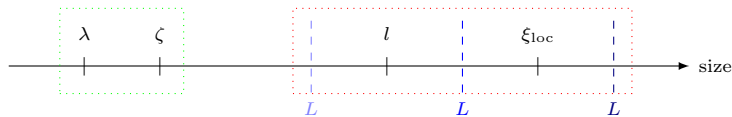


Figure 4: Probability distribution function $P(T, t)$ for the transmission T across a one-dimensional channel of length $t = L/\xi_{\text{loc}}$. Dashed line at $t = 10$: log-normal distribution (32).

son’s celebrated paper had founded [5]. After pioneering work by Wegner [18], a scaling theory of localization was formulated by Abrahams, Anderson, Licciardello, and Ramakrishnan [19], a quartet that became known as the “gang of four”.

A scaling theory can hope to capture those features that are important on macroscopic scales, but will be insensitive to microscopic details. This means that its predictions are only semi-quantitative, in the sense that it cannot furnish the precise location of a critical point in parameter space nor provide any system-specific data. In return, if one feeds it with the microscopic data (such as the transport mean-free path), it can give general, and surprisingly accurate, predictions of universal character.

Let us have a look at the different lengths characterizing quantum transport in a disordered material:



As short-scale lengths (in the left dotted box) one has the wavelength $\lambda = 2\pi/k$ of the propagating object and the correlation length ζ of the disorder. If $\zeta \ll \lambda$, the details of the disorder are unimportant, and models of δ -correlated scatterers are appropriate. If $\zeta \gg \lambda$, the disorder correlation can be resolved by the wave; this is typically the case for our example of optical speckle potentials probed with ultracold atoms [4].

As larger scales (in the right dotted box) one has the transport mean free path l and the localization length ξ_{loc} . We have already seen in section 2.2.3 that in $d = 1$ these two lengths are practically identical, $\xi_{\text{loc}} = 2l$. In $d = 2$ the localization length is much larger than the transport length, as will be discussed in sections 3.6 and 7.4 below, and in $d = 3$ it may well be infinite. Depending on the system size L , one can distinguish three basic transport regimes: *ballistic* transport through small samples with $L < l$, *diffusive* transport for $l < L < \xi_{\text{loc}}$ with, possibly, weak-localization corrections, and finally *strong localization* for large samples with $\xi_{\text{loc}} < L$. In $d = 1$, there is no room for diffusion between l and ξ_{loc} , and strong localization is basically a single-scattering effect.² The scaling theory of localization has the purpose of describing the transition between these regimes as function of system size L [22].

3.2 Dimensionless conductance

Traditionally, the scaling theory of localization is formulated in terms of a channel’s *proper conductance*, a dimensionless parameter defined as $g = T/R$ by transmission and reflection probabilities. Equivalently, one may consider the channel’s *proper resistance* g^{-1} . A perfectly transmitting channel $T = 1$ has a proper conductance of $g = \infty$, and a perfectly resisting channel with $T = 0$ has $g = 0$, which seems a rather sensible definition. Moreover, we have seen in section 2.2.2 that this resistance is additive when classical subsystems are chained in series. Alternatively, one could define the total resistance as $\rho = 1/T = 1 + g^{-1}$,

²See [20, 21] for a situation where backscattering of an atom by a smooth speckle potential is zero at lowest order, but localization still prevails due to higher orders in perturbation theory.

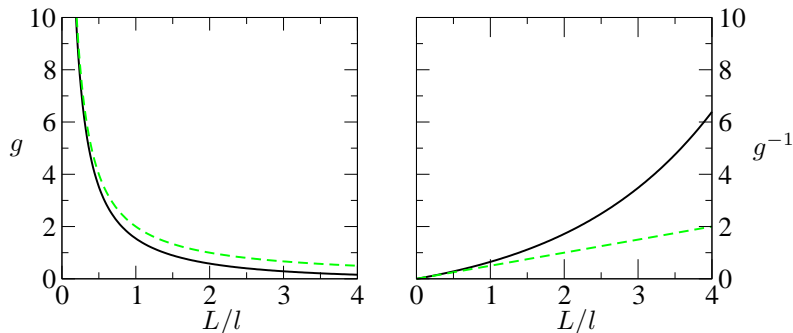


Figure 5: Typical conductance (left panel) and resistance (right panel) of a 1d channel as function of sample length L/l . Short channels have a resistance that grows linearly as expected by Ohm’s law (green dashed, eqn (41)), whereas long channels show exponentially large resistance (full line, eqn (42)).

where the additional 1 represents the “contact resistance” due to the leads connecting the sample to the external world.

In the previous section, we also learned that the transmission of a disordered channel is a random variable with a broad distribution around a most probable, typical value $T_{\text{typ}} = \exp \langle \ln T \rangle$. Therefore also $g = T/(1 - T)$ is a broadly distributed random variable, fluctuating around the *typical conductance* $g_{\text{typ}} = T_{\text{typ}}/(1 - T_{\text{typ}})$. In all of the following, we discuss the behavior of g_{typ} , but in order not to overburden the notation, we will simply write $g_{\text{typ}} = g$.

In order to get used to this vocabulary, let us reformulate the results of section 2 for the typical conductance. The exact exponential behavior (21) of the typical transmission translates into

$$g(L) = \frac{1}{\exp\{L/2l\} - 1} = \begin{cases} 2l/L, & L \ll l, \\ \exp\{-L/2l\} & L \gg l. \end{cases} \quad (41)$$

$$(42)$$

This conductance together with the resistance g^{-1} is plotted in Fig. 5. Only the conductance of short, ballistic channels is given by the classical expression (41), that we have already encountered as Ohm’s law in section 2.2.2.

The results of scaling for the conductance can be reformulated for other quantities if those seem more convenient. One of the most popular, and useful, quantities is the *diffusion constant* $D = vl/d$, the product of velocity and transport mean free path divided by the number of dimensions d , a convention whose rationale will become clearer below. For matter waves with wave vector k , the velocity is $v = \hbar k/m$, and the diffusion constant can also be written $D = \frac{\hbar}{dm} kl$, i.e., the product of an elementary diffusion constant (\hbar/dm) by the dimensionless quantity $kl = 2\pi l/\lambda$. This ratio describes the effective disorderiness of the medium: $kl \gg 1$ means that the wave can travel over many periods before suffering scattering. We will see in Sec. 7 below that kl is a crucial parameter for transport and localization properties.

In a metallic sample with usual electrical conductivity, the Drude formula $\bar{\sigma} = ne^2\tau/m$ establishes the direct proportionality between the conductivity $\bar{\sigma}$ and the classical diffusion constant $D = v^2\tau/d$ of charge carriers with mean free

path $l = v\tau$. We are thus led to define a dimensionless classical conductivity³

$$\hat{\sigma} = \frac{2mD}{\hbar}. \quad (43)$$

The conductance \hat{g} of a sample of linear size L in d dimensions is the ratio of $\hat{\sigma}$ to L^{2-d} . To see this, picture a metallic block where the voltage U is applied along one dimension to give $E = U/L$, whereas the current density $j = \bar{\sigma}E$ over the transverse area L^{d-1} yields the total current $I = L^{d-1}j$, which results in the dimension-full conductance $G = I/U = L^{d-2}\bar{\sigma}$. In order to define a dimensionless conductance \hat{g} , one has to compensate the factors of L with another length scale. The simplest choice is the inverse of the wave number k . One can thus define a classical dimensionless conductance as

$$\hat{g}(L) = (kL)^{d-2}\hat{\sigma} \quad (44)$$

In 1d, this definition gives $\hat{g}(L) = 2l/L$, i.e., is fully compatible with the known exact result at short distance, eq. (41) (this is the reason for the factor 2 introduced in eq. (43)). It is of course no accident that the two definitions of dimensionless conductance — through the diffusion constant or through the transmission across a sample — coincide. The Landauer formula [23] makes the connection explicit.

In any dimension, the classical dimensionless conductance can be rewritten as:

$$\hat{g}(L) = \frac{2kl}{d}(kL)^{d-2} \quad (45)$$

In particular, in dimension 2 we have $\hat{g} = kl$ itself, independently of the system size.

3.3 Scaling in 1D systems

Since we wish to follow how the dimensionless conductance g evolves with system size, we make use of the β -function,

$$\beta = L \frac{d \ln g}{dL} = \frac{d \ln g}{d \ln(L/L_0)}. \quad (46)$$

$\beta = 0$ means that g does not change with L . Actually, $\beta = cst$ implies purely algebraic dependence $g(L) \propto L^\beta$. The celebrated function $\beta(g)$ has been introduced originally by Callan and Symanzik to describe the change of a coupling constant under a change of scale within quantum field theory [24]. Let us familiarize ourselves with the β -function, arguably the most important single object of scaling theory, in the case $d = 1$, for which we know already everything exactly. It is a matter of elementary calculus to find

$$\beta(L) = -\frac{L}{2l} \frac{1}{1 - \exp\{-L/2l\}}. \quad (47)$$

Since $g(L)$ is a monotonous function of $L/2l$, one can easily invert this dependence and express β as function of the conductance alone:

$$\beta(g) = -(1 + g) \ln [1 + g^{-1}]. \quad (48)$$

³This definition, as well as (44), uses \hbar/m available for quantum matter waves. It should be adapted to any other specific transport problem under study, along the same lines. The somewhat arbitrary factor of 2 is included for future convenience.

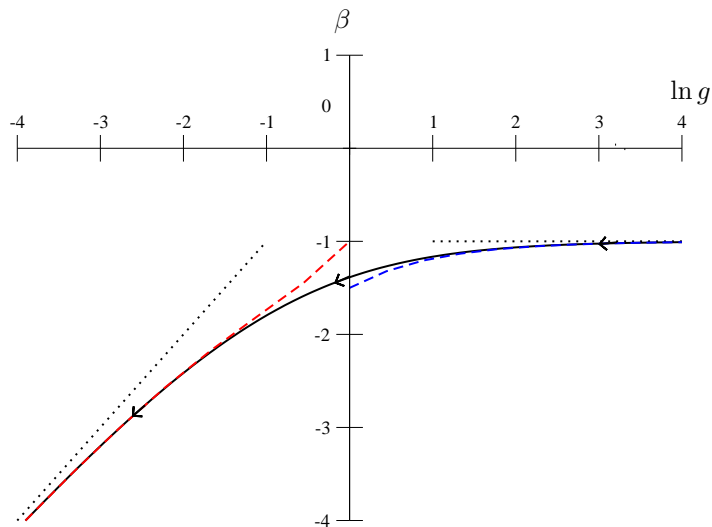


Figure 6: Conductance scaling β -function in $d = 1$, eq. (48). Arrows show the flow from the Ohmian behavior (49) for $g \gg 1$ in short samples to the exponential localization (50) for $g \ll 1$ in long samples.

This result can also be derived directly as follows: the linear scaling of the typical-transmission logarithm implies $T_{\text{typ}}(bL) = [T_{\text{typ}}(L)]^b = \exp\{b \ln T_{\text{typ}}(L)\}$. Writing $T_{\text{typ}}^{-1} = 1 + g^{-1}$, differentiating with respect to b , and setting $b = 1$ at the end leads to (48). The fact that $\beta(g)$ can be expressed as function of g instead of the original length scale L does not seem very profound in $d = 1$ [14]. However, in field theory this property is vital for renormalizability [24], and in statistical physics it guarantees that $\beta(g)$ can describe universal behavior close to a phase transition.

Figure 6 shows the β -function for $d = 1$, plotted as function of $\ln(g)$ together with its asymptotics. For short samples $L \ll l$, the conductance $g \propto L^{-1}$ is large, and $\lim_{g \rightarrow \infty} \beta(g) = -1$. More precisely, one has the following asymptotic behavior:

$$\beta(g) = -1 - \frac{1}{2g} + O(g^{-2}) \quad (49)$$

which shows a *weak-localization* correction (see section 7 below). In the opposite limit of a large sample, $g \ll 1$ is exponentially small, and

$$\beta(g) = \ln g - g(|\ln g| + 1) + O(g^2). \quad (50)$$

The transition between the two asymptotic regimes occurs around $g = 1$. The function $\beta(g)$ entirely describes how the dimensionless conductance evolves with system size L . Indeed, if g is known for some small size L , it can be deduced for any other size by solving the differential equation (46), moving along the arrows shown on the curve of figure 6. This is the so-called “renormalization flow” followed by the system when its size is increased towards macroscopic scales. For $d = 1$, β is always negative, implying that g always decreases with increasing system size, and thus the renormalization flow is unidirectional from right to left. Characteristically, when g decreases, β becomes more negative,

which makes g decrease even faster, until it finishes by dropping exponentially fast.

A crucial asset of scaling theory is that its predictions are valid for an arbitrary 1d system, although the specific form of $\beta(g)$ was deduced using a specific model. Suppose you have a large-size complex disordered system and that you want to study its conductance. You may start with a small system for which you can calculate the conductance microscopically using a method of your choice. By following the renormalization flow, you are then provided, almost magically, with the conductance at any scale. Moreover, you find the localization length ξ_{loc} as the system size for which $g(\xi_{\text{loc}}) = O(1)$. Of course, there is no real magic here: your initial calculation yields the mean free path l and, as this is the only macroscopic length scale relevant for transport in a 1d system, you finally have everything.

3.4 Quasi-1D systems

The previous results may also be applied to quasi-one-dimensional systems that consist of several parallel channels $i = 1, \dots, N_{\perp}$. One may either have in mind channels that are literally built parallel to each other [25] or a multi-mode waveguide with spatially overlapping transverse modes. If there is no coupling between channels, then the purely 1d description of section 2 applies. For weakly coupled channels, which arises naturally by the disorder present, an equation of motion for the full distribution function of transmission eigenvalues very similar to (35) has been derived by Dorokhov and independently by Mello, Pereyra, and Kumar, known as the DMPK equation [9]. Also the scaling picture remains essentially the same. Keeping the number of transverse modes N_{\perp} fixed, the short-scale conductance is $g = N_{\perp} 2l/L$, as expected for parallel resistors. Thus, the initial condition for the scaling flow on the curve $\beta(g)$ is changed, but the transition to the localized regime is the same. Since the crossover again occurs at $L = \xi_{\text{loc}}$ with $g(\xi_{\text{loc}}) = O(1)$, we simply find that the localization length is increased toward $\xi_{\text{loc}} = 2N_{\perp} l$.

3.5 Scaling in any dimension

In arbitrary dimension d , one changes the system size $L \mapsto bL$ in *all* directions, but still looks at the transmission along one chosen direction. In the ballistic regime $L \ll l$, we start again from the classical behavior, eq. (45), where $g(L) \propto L^{d-2}$. One therefore expects to find $\lim_{g \rightarrow \infty} \beta(g) = d - 2$, and

$$\beta(g) = d - 2 - \frac{c_d}{g} + O(g^{-2}) \quad (51)$$

where a microscopic calculation is required to find the coefficient c_d that describes weak localization corrections.

In the strongly localized regime $L \gg \xi_{\text{loc}}$, exponential localization prevails. And since adding parts to the system beyond the localization length in the perpendicular direction cannot change its longitudinal transport, we still expect the power law $T_{\text{typ}}(bL) = [T_{\text{typ}}(L)]^b$ to hold in each channel. Thence follows the asymptotic behavior

$$\beta(g) = \ln(g/g_d) \quad (52)$$

in the strongly localized regime in any dimension, with a constant g_d of order unity.

Taking into account that the number of transverse channels scales as b^{d-1} , we would obtain the simple scaling relation $T_{\text{typ}}(bL) \approx b^{d-1}[T_{\text{typ}}(L)]^b$, if there were strictly no coupling between the channels. Then, the same calculation than for 1d would give

$$\beta(g) = (d-1) - (1+g) \ln [1 + g^{-1}], \quad (53)$$

that is a simple vertical shift of (48) by $d-1$. In particular, this would imply that the weak localization correction $-c_d/g$ is the same in all dimensions, a result known to be wrong, see Sec. 7. It nevertheless remains true that the shape of the true $\beta(g)$ curves, interpolating smoothly between the known asymptotics, is qualitatively given by (53), see also Fig. 7. Although the scaling description encompasses arbitrary dimensions, its consequences are radically different in $d=2$ and $d=3$, meriting a separate discussion.

3.6 $d=2$

In the ballistic limit of short samples with typical conductance $g \gg 1$, $\beta(g) \approx 0$ describes scale-independent conductance of $N_{\perp} \propto L$ transverse channels, each with element conductance $g \propto L^{-1}$. But then, $\beta(g)$ is not exactly zero. Starting the flow at the finite conductance g_0 of a sample of length L_0 , a slightly negative $\beta(g) = -c_2/g$ makes g decrease with size (it will be shown in section 7 below that $c_2 = 2/\pi$). We can integrate the flow equation

$$\beta(g) = -\frac{c_2}{g} = \frac{1}{g} \frac{dg}{d \ln(L/L_0)} \quad (54)$$

by elementary means to find

$$g(L) = g_0 - c_2 \ln(L/L_0). \quad (55)$$

To fix ideas, we can chose $L_0 = l$, a scale on which transport is classical, such that, from eq. (45), $g(L_0) = \dot{g} = kl \gg 1$. The transition to the strong localization regime occurs at $g(\xi_{\text{loc}}) = O(1)$. Together with (55), this predicts an exponentially large localization length

$$\xi_{\text{loc}} \sim L_0 \exp\{g_0/c_2\} = l \exp\{kl/c_2\}. \quad (56)$$

The prediction of scaling theory for noninteracting particles in $d=2$ is therefore that all states are localized. This transcends also from the scaling flow depicted in figure 7. However, the localization length can be extremely large if the system is only weakly disordered with $kl \gg 1$. Let us take some figures from the Orsay experiment [4]. With $l = 100 \mu\text{m}$ and $k = 2.5 \mu\text{m}^{-1}$, one finds the rather large localization length $\xi_{\text{loc}} \approx l e^{400}$, which would surely overstretch the possibilities of even the most capable experimentalist. The take-home message here is: In order to observe 2d localization, kl should be chosen as close to unity as possible. In turn, this implies that the classical diffusion constant $D = \hbar kl/2m$ must be of the order of \hbar/m , which for a typical cold atomic gas is a rather small quantity of the order of $10^{-9} \text{m}^2/\text{s}$. In order to observe 2d Anderson localization with atomic matter waves, the experimentalist must be capable to observe the dynamics for a long time while keeping phase coherence, a challenging task indeed.

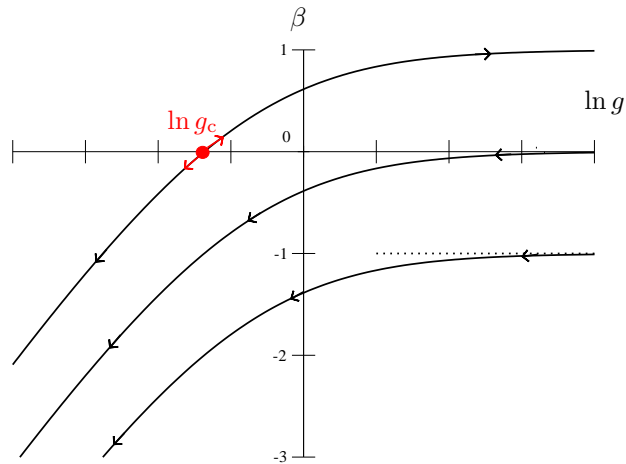


Figure 7: Schematic plot of the β -function in $d = 1, 2, 3$, showing a smooth interpolation from the metallic regime (51) for $g \gg 1$ in short samples to the localized regime (52) for $g \ll 1$ in long samples. Note the existence of an unstable fix-point at critical g_c in $d = 3$.

3.7 $d = 3$

In $d = 3$, we encounter a qualitatively new situation: the β -function is positive for large g . So if we start with some $g \gg 1$, the conductance flow will take us to even larger values of g . In renormalization-group terms, the behavior of the system in the thermodynamic limit $L \rightarrow \infty$ is described by the “infra-red stable fix-point” $g = \infty$ (as in statistical physics, but in contrast to quantum field theory, we are interested in the large-distance behavior, i.e., the infra-red asymptotics with respect to momentum). Since large conductance characterizes a good conductor, this is also known as the “metallic” fix-point.

By contrast, if we start with some $g \ll 1$, the negative β -function will drive the system towards the stable insulating fix-point $g = 0$ with exponentially small conductance at finite length. Between these two extrema, the β -function, assumed to be continuous, must have a zero at some g_c . A zero of $\beta(g) \propto dg/dL$ is also a fix-point, but in this case an unstable one. This unstable fix-point $\beta(g_c) = 0$ marks the critical point and shows the possibility of a *metal-insulator phase transition* at some critical strength of disorder. Although a scaling theory, with its roughly interpolating β -function, cannot predict the precise position of the critical point, it can give a semi-quantitative estimate. Indeed, a microscopic calculation of the transport mean free path l provides us with the dimensionless conductance $g(l)$. At such a scale, interference effect are unimportant, and thus, eq. (45) can be used, giving $g(l) \approx 2(kl)^2/3$. As the critical point is such that $g_c \sim 1$, we obtain that the threshold for Anderson localization is given by:

$$kl \sim 1 \quad (57)$$

an equation known as the Ioffe-Regel criterion for localization. The precise value of the critical kl depends on microscopic details and is thus not universal.

Let us assume that the microscopic physics involves disorder whose strength

is measured by some parameter W , typically the width of the disorder probability distribution (cf. Sec. 4.1.4). Even though scaling theory does not predict the precise position of the critical point, the behavior of the β -function around the critical point yields precious information about the large-scale physics: it permits to calculate *critical exponents* that are the hallmark of universality. In their 1979 paper [19], Abrahams et al. showed that the localization length diverges close to the transition for $W > W_c$ as

$$\xi_{\text{loc}} \sim (W - W_c)^{-\nu}, \quad (58)$$

where the critical exponent $\nu = 1/s$ is determined by the slope of the β -function at the transition, $s = [d\beta/d \ln g]_{g_c}$.

The calculation leading to this prediction is elementary, but quite instructive in order to appreciate the power of a scaling description. Let us start at some length L_0 with some value $g_0 < g_c$ on the localized side of the fix-point. The β -function always allows us to calculate any other $g(L)$ implicitly by integration:

$$\ln \left(\frac{L}{L_0} \right) = \int_{\ln g_0}^{\ln g} \frac{d \ln g'}{\beta(g')}. \quad (59)$$

Using the linearized form $\beta(g) = s \ln(g/g_c)$ around the fix-point leads to

$$\left(\frac{L}{L_0} \right)^s = \frac{\ln(g_c/g)}{\ln(g_c/g_0)}. \quad (60)$$

Now we are free to choose $L_0 = \xi_{\text{loc}}$ for which $g_0 = O(1)$ such that $\xi_{\text{loc}} \sim L [\ln(g_c/g)]^{-1/s}$. Because the microscopic physics on small scales ignores the critical behavior on large scales and can involve only smooth dependencies, one can always write $\ln(g/g_c) \approx (g - g_c)/g_c \propto (W_c - W)$ close enough to the critical conductance g_c , and we finally end up with (58).

For the simplest possible interpolation (53), one finds $\nu \approx 1.68$. This value is not disastrously far from the true value $\nu = 1.58 \pm 0.01$ that is known today from extensive numerical simulations [26, 27], cf. Sec. 4.3.

The “metallic” side of the transition can also be studied using a similar approach, but following the metallic branch $\beta > 0$ of the renormalization flow. For smaller-than-critical disorder strength $W < W_c$, the microscopically computed g at some size L_0 will be slightly larger than g_c . It is left as an exercise for the reader to show that this results at large scale in a diffusive (i.e., metallic) behavior with a diffusion constant

$$D \propto (W_c - W)^\nu. \quad (61)$$

The continuous (algebraic) vanishing of diffusion constant and conductance on the metallic side of the Anderson transition is characteristic of a continuous second order phase transition.

3.8 $d > 3$

The Anderson transition is expected to take place in any dimension $d \geq 3$. According to the simple scaling theory sketched above, the transition point will shift to lower and lower g_c , requiring a more strongly scattering medium to

observe localization, and thus a Ioffe-Regel criterion, eq. (57), with a smaller constant.

Contrary to conventional phase transitions, the Anderson metal-insulator transition does not have a finite upper critical dimension above which fluctuations would be unimportant and critical exponents simply given by their mean-field values [15]. This is compatible with the observation that as the dimension d increases, the zero of the β -function must shift more and more to the asymptotic $\ln(g)$ -wing where the slope tends towards $s = 1$. Thus, from the scaling description it is tempting to surmise that the critical exponent tends towards $\nu = 1$ only continuously as $d \rightarrow \infty$. We will see in section 8 below that this observation is not only a theoretician's spleen but may be put to experimental testing.

4 Key numerical and experimental results

Over the past 50 years, a wealth of numerical and experimental results has been accumulated on localization phenomena, especially on Anderson localization in dimension 1, 2, 3 and beyond. In the following, we present a selection, necessarily subjective and limited, of the most remarkable results.

4.1 $d = 1$

Anderson localization is a generic feature in phase-coherent 1d and quasi-1d systems, as explained in Section 2.2.3 above. Any amount of disorder, even very small, will eventually localize a wavepacket, independently of how large its energy is. Of course, the localization length can be huge if the energy is large compared to the disorder; see Section 5.2.4 for a quantitative estimate.

4.1.1 Localization of cold atoms

Concerning the experiment described in the Introduction, there is thus no surprise that a quasi-1d atomic wavepacket displays localization in an optical speckle potential. Figure 8a) shows the experimentally measured spatial shape of the wavepacket at various times. One clearly distinguishes an exponential decrease in the wings, from which a localization length is extracted by a fit to $\exp\{-2|z|/L_{\text{loc}}\}$. As shown in b), this localization length first increases with time, then settles for a stationary value after about 500 ms. In the stationary regime, the wavepacket displays spatial fluctuations which are different for each single realization of the disorder. In addition, there remains a large fraction of the atoms still trapped near the original location of the wavepacket.

How can we understand these experimental results? The initial wavepacket is not monochromatic at all: it contains plane waves with a large dispersion in the wave-vector k and consequently in the kinetic energy $\hbar^2 k^2/2m$ (the added optical potential also contributes to the total energy, but is a small correction here). The initial, free expansion of an interacting Bose-Einstein condensate released from a harmonic trap leads to a population of the various k classes that is given by an inverted parabola [28]:

$$\Pi_0(k) = \frac{3(k_{\text{max}}^2 - k^2)}{4k_{\text{max}}^3} \Theta(k_{\text{max}} - |k|), \quad (62)$$

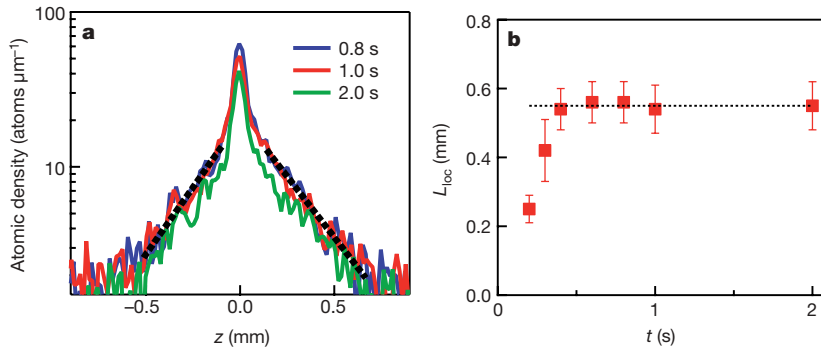


Figure 8: a) The atomic density of a BEC expanding in a quasi-1d optical speckle potential, shown in logarithmic scale at various times, displays clear exponential localization in the wings, from which the localization length is extracted by a fit (dashed line). b) The localization length first increases linearly with time, then saturates in the stationary regime. Reprinted from [4] (courtesy of Ph. Bouyer).

where k_{\max} is the maximum k value, related to the initial chemical potential by $\mu = \hbar^2 k_{\max}^2 / 2m$.

Because the disordered is “quenched” or stationary, energy is conserved, and each k -component of the wavepacket evolves independently. When averaged over time, the interference terms between different energy components will be smoothed out, leaving the averaged wavepacket as the *incoherent* superposition of all energy components. From Section 2.2.3, we know that each k -component localizes with a localization length $\xi_{\text{loc}}(k)$ equal to twice the transport mean free path. For the fastest atoms, this localization length is much larger than the initial spatial extension of the wave packet. Thus, we predict the stationary spatial distribution once localization sets in to be roughly given by

$$\langle |\psi(z)|^2 \rangle = \int_{-k_{\max}}^{k_{\max}} \frac{\Pi_0(k) \xi_{\text{loc}}(k)}{2} \exp\left(-\frac{|z|}{\xi_{\text{loc}}(k)}\right) dk. \quad (63)$$

Since $\xi_{\text{loc}}(k)$ is an increasing function of $|k|$, see section 5.2.4, the asymptotic decrease at large distance is dominated by the largest $|k|$ values, such that $\langle |\psi(z)|^2 \rangle \propto \exp[-|z|/\xi_{\text{loc}}(k_{\max})]$. The low- k components have short localization lengths and thus produce the large bump near the origin in the final density. Using only the wings of the experimentally measured density, it is possible to estimate the localization length, for which we derive in Sec. 5.2.4 a theoretical prediction.

4.1.2 Localization of light: a ten-Euro experiment

The reasoning in section 2.2.3 is entirely based on the construction of a 2×2 transfer matrix which can be chained; any randomness in the transfer matrix then leads to localization. The fact that our starting point was a quantum matter wave and the underlying wave-particle duality of quantum mechanics are not central to this argument. Indeed, the transfer-matrix description applies to all physical situations governed by a 1d (or quasi-1d) linear wave equation. Consequently, Anderson localization has been observed for many different types

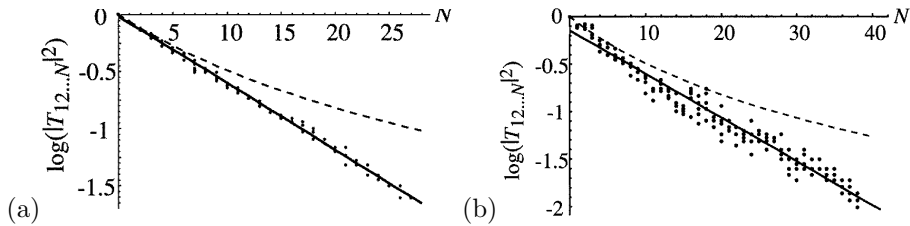


Figure 9: Logarithmic transmitted intensity across stacks of N plastic films with mean thickness (a) 0.25 mm; (b) 0.1 mm. Dots: experimental data. Full curve: best fit to the data. Dashed curve: prediction of incoherent transmission (Ohm's law). Reprinted from [29] (courtesy of M.V. Berry).

of non-quantum waves: microwaves, elastic waves in solids, optical waves, to cite a few.

Even a poor man's experiment using viewgraph transparencies, i.e., plastic films made of polyester carbonate, allows to observe Anderson localization. A stack of several transparencies parallel to each other, separated by air layers of randomly varying thickness, realizes the simple model shown in fig. 2. The transmission and reflection coefficients for an individual film can be computed from its index of refraction and its thickness. If the randomness in the film spacing is larger than an optical wavelength, we have a truly disordered system. Transport and localization can be observed by illuminating the stack of transparencies with a plane light wave (or rather a good approximation of a plane wave, namely, the light from a simple commercial He-Ne laser) and recording the transmission. Fig. 9 shows the transmission vs. the number N of films or thickness of the sample. It displays a clear exponential decay, one of the signatures of Anderson localization, and markedly differs from the linear decay (Ohm's law) predicted for the incoherent transport of intensities.

It is important to realize that absorption in the transparencies would also result in an exponential decay of the transmitted intensity. In all Anderson localization experiments, it is crucial to ensure that absorption is negligible, especially when working with electromagnetic waves. In this specific case, the bulk absorption coefficient of polyester carbonate is known to be negligible here. In principle, one could also double-check that no photon is lost by measuring the reflection coefficient of the sample and verifying that $R + T = 1$. In condensed-matter experiments with electrons or cold atoms, number conservation of massive particles makes absorption less relevant and simpler to monitor.

Another crucial requirement in the experiment is that it remains a 1d system, i.e., that there is a single transverse electromagnetic mode involved. Light polarization is not an issue (for perpendicular incidence, scattering is independent of polarization), but surface roughness or lack of parallelism can cause scattering into other transverse modes. This coupling into loss channels eventually destroys localization. Some indication of this loss is visible in Fig. 9(b): the decay is not really exponential, but bent upwards, towards the prediction for incoherent transmission.

The experimental data show fluctuations of the transmission for various realizations of the experiment. This is not surprising, on the contrary, according to Section 2.5, the fluctuations are even expected to be large. However, it turns

out that the observed fluctuations are smaller than predicted: in the plot, the transmission logarithm should appear as a cloud of points whose variance, eqn. (33), increases like N , which is not clearly the case. Most probably, this is due to the experimental imperfections mentioned above that couple several transverse modes and consequently attenuate the fluctuations.

4.1.3 Fluctuations

As already emphasized several times, the existence of large fluctuations of the transmission is a characteristic feature of Anderson localization. A key advantage of measuring relative fluctuations is that they are not much affected by absorption, which merely induces a global decay of the whole transmission distribution. Consequently, in the last few years, much progress has been made in calculating and measuring fluctuations in diffusive and localized systems. Fluctuations provide us with an unambiguous way of characterizing Anderson localization, even in the presence of absorption.

In order to illustrate this claim, we show in Fig. 10 the transmission of microwaves across a quasi-1d sample composed of aluminium spheres randomly disposed in a long copper tube (cooled with liquid nitrogen so that absorption is negligible), as a function of the microwave frequency [30]. The transport mean free path depends on the resonant scattering cross section of the aluminium spheres, and thus varies strongly with frequency, implying large changes in the relative sample length $t = L/l$. Plot (a) is obtained in the diffusive regime, where the localization length is longer than the sample size: there, the transmitted intensity fluctuates in an apparently random way, but the fluctuations are relatively small, the rms deviation being comparable to the mean. This is expected in the diffusive regime for relatively short samples, where the transmission amplitude itself is expected to behave like a complex random number, whose real and imaginary parts are independent, normally distributed variables. In contrast, in the localized regime shown in plot (b), the fluctuations are much larger, the transmission being most of the time very small with some rare events of exceptionally high transmission, as predicted in Section 2.5.

Visual inspection reveals immediately that plots (a) and (b) are obtained in different regimes. While plot (a) has relatively small fluctuations, characteristic of a diffusive regime, where the fluctuations are comparable to the mean, plot (b) suggests some kind of huge (log-normal) fluctuations, typically associated with the localized or critical regime. The take-home message here is: don't rely solely on exponential decay to prove the existence of localization, look also at the fluctuations, they are better indicators. Since the relative fluctuations are insensitive to moderate absorption, they may even provide a quantitative criterion whether the strong localization threshold has been reached or not, and this under circumstances when the exponentially decreasing transmission alone could not be a reliable signature [31, 32].

4.1.4 The Anderson model: a free (numerical) experiment

Although the Anderson model was originally introduced as a tight binding model for electrons in a disordered crystal, it is of broader interest and has become a paradigm for one-body localization effects.

Up to now, we have considered continuous models where a wave propagates

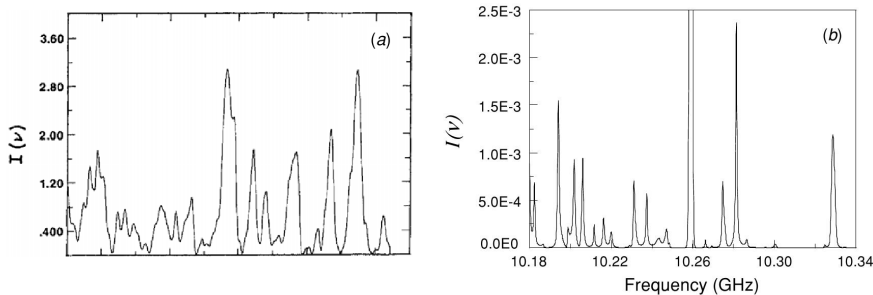


Figure 10: Microwave intensity transmitted across a copper tube filled with scattering aluminium spheres vs. the microwave frequency. In the diffusive regime (a) (frequency around 17 GHz), fluctuations are comparable to the average value. In the localized regime (b), huge fluctuations are visible, a hallmark of Anderson localization. Reprinted from [30] (courtesy of A. Z. Genack).

along a continuous 1d axis, encountering a set of discrete objects that scatter the wave backward and forward. The transfer-matrix game is just to combine the discrete scatterers with the proper phases. One can even go one step further, disregard the ballistic propagation, and build a completely discrete model, where the wave lives on a 1d lattice. One of the simplest discrete models is certainly the Anderson model whose Hamiltonian is

$$H = \sum_{n=-\infty}^{+\infty} (w_n |n\rangle\langle n| + t|n\rangle\langle n+1| + t|n+1\rangle\langle n|) \quad (64)$$

where the state $|n\rangle$ is the occupation amplitude of site n with w_n its on-site energy. t is the so-called “tunneling” matrix element coupling neighboring sites, traditionally taken with numerical value $t = 1$. In a concrete physical realization, typically also the t ’s are random variables and thus define “off-diagonal disorder”. However, it is enough to take diagonal disorder to observe localization. The precise value of t is irrelevant, as long as it is not zero, and may be used to define the energy scale of the problem. If $w_n = 0$, it is easy to check that the eigenstates are discrete plane Bloch waves $\psi_n = \exp ikn$, for $k \in [-\pi, \pi]$, and the energy is given by the dispersion relation $E(k) = 2 \cos k$ of this single-band model.

Disorder is introduced by allowing the on-site energies w_n to be random variables. The standard choice is to take w_n to be uncorrelated random variables uniformly distributed in the interval $[-W/2, W/2]$, with $W^2 = 12\langle w_n^2 \rangle$ measuring the disorder strength. A noteworthy property—simplifying analytic calculations—is that the spatial correlation length of the disorder is zero (see Sec. 5.1.4 for a discussion of spatial correlations arising in optical speckle potentials). Actually, the 1d tight-binding Anderson model can be solved for almost any distribution [33], with simple closed expressions for the Cauchy-Lorentz on-site distribution. The techniques developed in Sec. 5 permit to show that the localization length is at lowest order in W given by

$$\xi_{\text{loc}} = \frac{4 \sin^2 k}{\langle w_n^2 \rangle} = \frac{12(4 - E^2)}{W^2}. \quad (65)$$

Exercise 4 – Few properties of the Anderson model.

- (i) Show that the equations obeyed by an eigenstate of the Anderson model at energy E can be put in the following matrix form:

$$\begin{pmatrix} \psi_{n+1} \\ \psi_n \end{pmatrix} = T_n \begin{pmatrix} \psi_n \\ \psi_{n-1} \end{pmatrix} \quad (66)$$

with a transfer matrix:

$$T_n = \begin{pmatrix} E - w_n & -1 \\ 1 & 0 \end{pmatrix}. \quad (67)$$

Show that the amplitudes of the left and right propagating plane waves in a disorder-free region can be expressed as simple linear combinations of ψ_n and ψ_{n+1} . Show that, in consequence, it is possible to construct a transfer matrix M as in eq. (9). This shows that the general results of section 2.2 can be used and that exponential localization is expected.

- (ii) Consider a continuous model of a 1d particle in a disordered potential $V(z)$. By discretizing the Schrödinger equation on a lattice with sufficiently small spacing (much shorter than the de Broglie wavelength and the correlation length of the potential), show that one recovers the Anderson model, but with spatially correlated w_n .

Numerical simulations of the Anderson model are extremely easy, at least in dimension 1. Indeed, the previous exercise shows that the time-independent Schrödinger equation reduces, for an eigenstate $|\psi\rangle = \sum_n \psi_n |n\rangle$ with energy E , to the three-term recurrence relation

$$\psi_{n+1} + (w_n - E)\psi_n + \psi_{n-1} = 0 \quad (68)$$

which can be solved recursively. In Fig. 11, we give an example of a simple script, written in the Perl language, that solves this equation at some arbitrary energy across a random sample of arbitrary length.

Note that the boundary condition used, $\psi_N = 1$ and $\psi_{N+1} = e^{ik}$, describes a purely outgoing wave with wavevector k and amplitude 1 on the right end of the sample. The boundary condition on the left is actually more complicated, because there the incident wave interferes with the reflected wave, whose amplitude depends on the microscopic realization of disorder of the entire sample. The Schrödinger recursion equation is thus better solved backwards from the far end of the sample, yielding on average an exponentially *increasing* solution toward the left. This is in agreement with the fact, shown in exercise 2(iv) above, that the two eigenvalues of the transfer matrix are of the form $\lambda_{\pm} = e^{\pm 2x}$. So starting with this boundary condition and an arbitrary value of k (and thus E), one has, with probability one, a finite overlap with the eigenvectors of the larger eigenvalue and therefore numerically picks up an exponentially growing solution. This solution is then at the same time physically acceptable for the transmission experiment, viz., decreasing on average exponentially from left to right. Since eq. (68) is linear, one can always normalize the solution to unit incoming flux and thus finally find the transmission probability as the outgoing flux on the right side, calculated as a linear combination of ψ_N and ψ_{N+1} (cf. the perl script and exercise 4(i)).

```

#!/usr/bin/perl
use Math::Trig;
use Math::Complex;
# compute_log_psi2_and_log_T.pl
# Author: Dominique Delande
# Release date: Feb, 24, 2010
# License: GPL3
#-----
# This script models Anderson localization in the Anderson model of disordered 1d systems.
# It computes the transmission across a sample of size $system_size at energy $energy.
# Without disorder, the spectrum is [-2,2], the dispersion relation $energy=2*cos($k).
# Disorder is given by the on-site energies $w_n,
# uncorrelated and uniformly distributed in [-$W/2,$W/2].
# The equations are: \psi_{n+1} + \psi_{n-1} + (w_n-E) \psi_n = 0
# They are solved in the backward direction, starting from a normalized outgoing wave.
# |\psi|^2 is printed in file logpsi2.dat and -log(T) in logT.dat
# for $number_of_realizations independent realizations.
# The localization length is 12*(4-$energy**2)/$W**2 at lowest order in $W.
#-----
$system_size=1250;
$W=0.6;
$energy=0.5;
$k=acos(0.5*$energy);
$exp_i_k=cplx(cos($k),sin($k));
$number_of_realizations=3; # put 1000 or 10000 for a decent histogram
open(LOGT,">logT.dat"); open(LOGPSI2,">logpsi2.dat");
for ($j=1;$j<=$number_of_realizations;$j++) {
    $psi_n_plus_1=$exp_i_k;
    $psi_n=1.0;
    select (LOGPSI2);
    for ($n=$system_size;$n>0;$n--) {
        $w_n=$W*(rand()-0.5);
        $psi_n_minus_1=($energy-$w_n)*$psi_n-$psi_n_plus_1;
        $logpsi2= 2.0*log(abs($psi_n));
        print "$n_$logpsi2\n";
        $psi_n_plus_1=$psi_n;
        $psi_n=$psi_n_minus_1;
    }
    print "\n";
    $psi_n_minus_1=$energy*$psi_n-$psi_n_plus_1;
    $reflected=(0.5*abs($psi_n_minus_1*$exp_i_k-$psi_n)/sin($k))**2;
    $incident=(0.5*abs($psi_n_minus_1-$exp_i_k*$psi_n)/sin($k))**2;
    $minus_log_T=log($incident);
    select (LOGT); print "$j_$minus_log_T\n";
}

```

Figure 11: This perl script, available also at <http://www.spectro.jussieu.fr/-Systemes-desordomes->, can be run in a few seconds on any reasonable computer with a perl interpreter, preferably running a Unix-based operating system, or using a free perl interpreter for the non-free MS-Windows operating system, such as <http://strawberryperl.com/>. Just type `perl compute_log_psi2_and_log_T.pl` in a shell window. The logarithm of the squared wavefunctions will be output (vs. position) in the file `logpsi2.dat` and can be visualized with your favorite plotting tool. (Minus) the logarithms of the transmissions (one for each realization of the disorder) are in the file `logT.dat`; use again your favorite plotting tool to build a histogram.

Figure 12 (left plot) shows the intensity $\ln |\psi_n|^2$ for three different realizations of the disorder at energy $E = 0.5$ and disorder strength $W = 0.6$ for a moderately large sample of 1250 sites, corresponding to a length $L = 10\xi_{\text{loc}}$. Although the decay is on the average exponential, huge fluctuations from one realization to another are visible with the naked eye. Moreover, even for this pure transmission experiment from left to right, the intensity is not monotonously decreasing at all, sometimes increasing by factors larger than 10. The histogram of the extinction (or transmission logarithm) over 10000 realizations is shown in the right plot. Its width clearly visualizes the huge fluctuations characteristic for the localized regime. The agreement with the predicted distribution function, eq. (36), shown with a red full line, is excellent. One also observes the convergence toward the truncated normal distribution (dashed), implying the truncated log-normal distribution (39) for T itself.

The reader is strongly encouraged to play with this script to experiment personally with Anderson localization. We recommend the following numerical experiments:

Exercise 5 – Numerical study of 1d Anderson localization

- (i) Use a single realization of the disorder and look at the wavefunction (or rather $|\psi|^2$) inside the medium. Try different sample lengths and different energies, but avoid the band center $E = 0$. Indeed, the Anderson model is singular at this value. There is still Anderson localization, but the localization length slightly differs from eq. (65), a so-called Kappus-Wegner singularity [33].
- (ii) Using a few hundred or thousand realizations, compute the statistical distribution of the transmission. Compare with the exact prediction eq. (36) as well as with a truncated normal distribution.
- (iii) Modify the script, for example for a Gaussian or Cauchy distribution of disorder and run additional numerical experiments. You may also introduce correlated disorder to simulate e.g. cold atoms in a speckle potential (see [20] for generation of a realization of the disorder with proper correlation functions).

A slightly different approach consist in diagonalizing the Hamiltonian for a large system numerically. Choosing strict boundary conditions on both ends of the sample yields normalizable eigenstates, centered at random positions within the sample and decreasing from there in both directions (similar to Fig. 8(a)), together with the discrete set of corresponding eigenvalues. In the thermodynamic limit, these eigenenergies form a dense, but still pure-point spectrum.

An important message to keep in mind is that there is very little difference between a continuous and a discrete system, as far as localization on large spatial scales is concerned. For example, the exercise shows how a particle in a continuous 1d random potential (e.g., an optical speckle) can be mapped to a variant of the Anderson model. This universality of the Anderson model cannot really surprise because localization is an asymptotic property taking place at large distance; whether the underlying configuration space is discrete or continuous plays only a minor role.

4.2 $d = 2$

Scaling theory predicts $d = 2$ to be the lower critical dimension for Anderson localization. In dimension $d = 2 + \epsilon$ (which can be numerically studied by

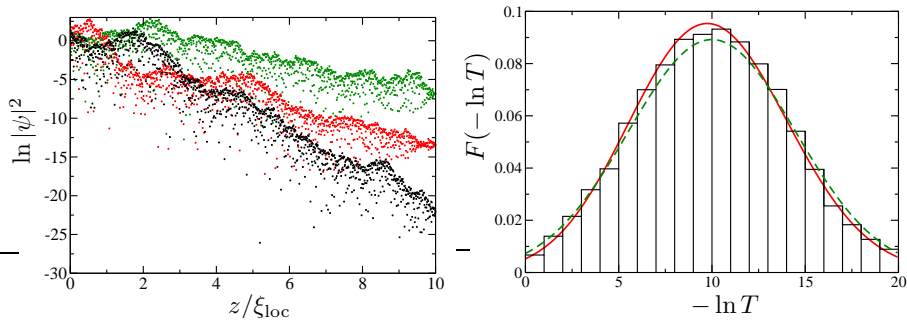


Figure 12: Results of numerical experiments on the 1d Anderson model, with uncorrelated uniform distribution of disorder. The left plot shows the intensity $|\psi(z)|^2$ inside the disordered medium—on a logarithmic scale—for three different realizations of the disorder. Note the overall exponential decrease, decorated by huge fluctuations: the transmission across a sample of size $L = 10\xi_{\text{loc}}$ fluctuates by more than 3 orders of magnitude. This illustrates why the typical transmission differs from the average one. The right plot shows the full probability distribution $F(-\ln(T), t)$ (histogram over 10000 realizations) for $t = z/\xi_{\text{loc}} = 10$, together with the prediction eq. (36) (full red line), which is close to a truncated Gaussian (dashed).

constructing an Anderson model on a fractal set), a critical point should exist where $\beta(g_c) = 0$, separating a diffusive phase from an insulating one. Strictly at $d = 2$, scaling theory predicts localization provided there is a weak localization correction with $c_2 > 0$, see section 3.6. We will see in section 7 that this is indeed what a microscopic approach predicts in spinless time-reversal invariant systems. Scaling theory does not pretend to be an exact theory, there is thus a real interest in knowing whether there is localization in 2 dimensions for specific systems.

Experiments with cold atoms are expected to be much more difficult than in 1d. Indeed, the localization length, eq. (56), is predicted to increase *exponentially* with the parameter kl , instead of linearly in 1d. Detailed theoretical studies [34] have shown that experimental observation requires at the same time a speckle potential with a very short correlation length (comparable to what has been done in 1d, but in 2 directions) and a long atomic de Broglie wavelength, that is very cold atoms. Altogether, satisfying all conditions is far from easy, making 2d Anderson localization of ultra cold atoms an interesting challenge.

A metal-insulator transition has been observed for electrons in clean semiconductor samples [35]. It is generally acknowledged that the Coulomb electron-electron interaction—much stronger than the atom-atom interaction in a dilute cold atomic gas—plays a major role in this transition, which is thus qualitatively different from the pure Anderson transition and sometimes referred to as the Mott-Anderson transition [36].

Other types of waves have been successfully used in 2d systems. For example, using conveniently engineered optical fibers, one can create a 2d “photonic lattice” composed of parallel optical guides along which the light can freely propagate. Thanks to the photorefractive material used, its index of refraction can be adjusted by an external light source. Also the transverse coupling between the optical guides can be adjusted at will, as well as the disorder due to small

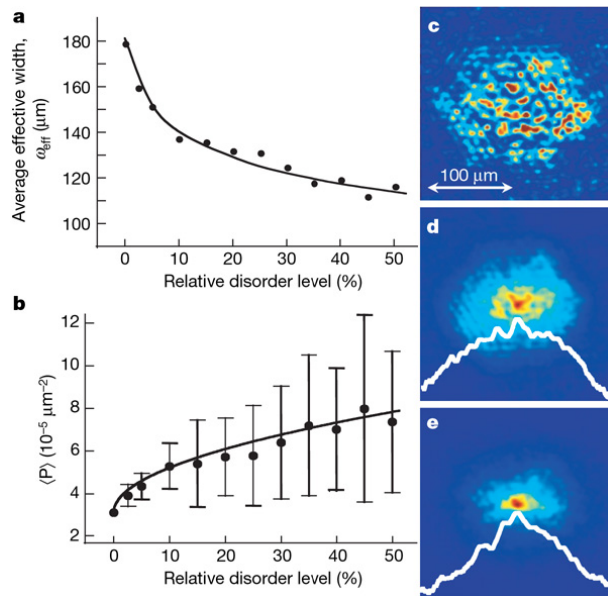


Figure 13: Experimental results on the propagation of light across a transversally disordered 2d lattice of photonic wave guides, mimicking the 2d Anderson model. As the strength of the disorder is increased, the dynamics evolves from ballistic (a and c) to diffusive (b and d), characterized by a Gaussian shape of the wavepacket, and eventually to Anderson localization, with a wavepacket of characteristic exponential shape (e), when the disorder is sufficiently strong to make the localization length comparable to the extension of the wavepacket. Reproduced from [37] (courtesy of S. Fishman).

variations of the index of refraction in each guide. As the light propagates at roughly constant velocity along the guides, the spatial propagation mimics the temporal evolution of the Anderson model, each guiding mode playing the role of a site. Using such a device, the evolution from ballistic motion (on a scale shorter than the mean free path) to diffusive motion and eventually to strong localization has been experimentally observed [37], see Fig. 13.

The Anderson model itself, described in section 4.1.4, can be trivially extended to any dimension by adding hopping terms to nearest neighbors in a (hyper)cubic lattice. The numerical study is slightly more difficult than in 1d. The basic idea is to study first the quasi-1d propagation on a strip with a fixed number M of transverse sites, imposing for example periodic boundary conditions along this direction. One can write a $2M \times 2M$ transfer matrix for this quasi-1d system and calculate its asymptotic properties as the length N goes to infinity, extracting the quasi-1d localization length $\xi_{\text{loc}}(M)$. Next, one studies the behavior of $\xi_{\text{loc}}(M)$ as M is sent to infinity. If $\xi_{\text{loc}}(M)$ diverges without bounds, one concludes that the system is not localized. If on the other hand $\xi_{\text{loc}}(M)$ tends to a finite limiting value, one concludes that the system localizes with $\xi_{\text{loc}} = \lim_{M \rightarrow \infty} \xi_{\text{loc}}(M)$.

Powerful numerical techniques, such as finite-size scaling [38], make it possible to extrapolate properties of the infinite system from numerical experiments

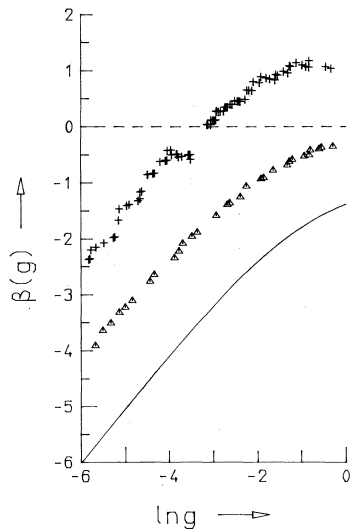


Figure 14: Scaling function $\beta(g)$ reconstructed from numerical simulations of the Anderson model. The solid line is for dimension 1, the triangles for dimension 2 and the crosses for dimension 3. Different sets of microscopic parameters produce data lying on the same curve, which can be considered an “experimental proof” that the scaling approach is valid. In 2d, $\beta(g)$ is always negative, proving that the system is in the localized regime. In 3d, depending on the disorder strength, the system may be localized ($\beta(g) < 0$, strong disorder) or diffusive ($\beta(g) > 0$, weak disorder). Reprinted from [39] (courtesy of A. McKinnon and B. Kramer).

on limited systems. Especially, the scaling function $\beta(g)$ can be reconstructed, see Fig. 14. The fact that various data, computed for various values of the system parameters (energy, disorder strength, system size), lead to the very same $\beta(g)$ strongly indicates that the scaling approach is valid, and thus corroborates the existence of universal properties independent of the microscopic details. In 2d, the numerically computed $\beta(g)$ is always negative, as expected and its shape is in good agreement with the naive prediction, eq. (53).

4.3 $d = 3$

Dimension 3 is arguably the most interesting, because scaling theory there predicts a transition between diffusive behavior for small disorder and Anderson localized behavior at large disorder. Consequently, much experimental and numerical effort has been spent to observe this Anderson transition. Numerical simulations of the 3d Anderson model are a very valuable tool, especially to locate the critical point where $\beta(g_c) = 0$ and to characterize its vicinity. The results in Fig. 14 very clearly show the existence of the two regimes and the fact that $\beta(g)$ behaves smoothly across the transition. This constitutes a clear-cut proof that the Anderson transition is a continuous phase transition of second order. Note the absence of data for g just below g_c ; this corresponds to localized systems with a localization length too large to be reliably measured in the numerical simulations. As shown in Sec. 3.7, the slope $d\beta/d\ln g|_{g_c}$ at the

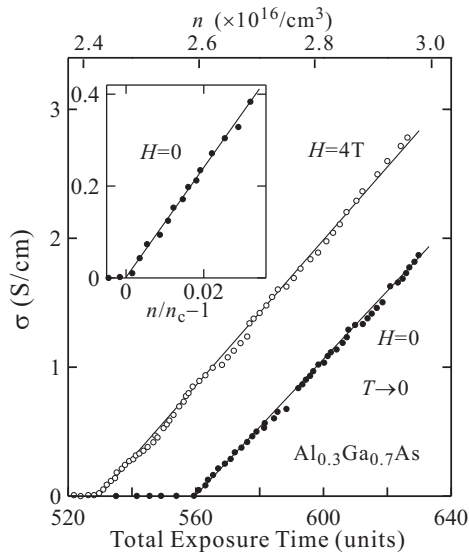


Figure 15: Experimentally measured conductivity of a Si-doped AlGaAs 3d crystal vs. electron concentration (upper horizontal scale), showing a clear metal-insulator transition. The critical exponent is very close to unity, a value not compatible with the universal value $\nu = 1.58$ of the pure 3d Anderson transition. Electron-electron interaction is probably responsible for the difference. Adapted from [40] (courtesy of S. Katsumoto).

critical point is the inverse of the critical exponent ν of the Anderson transition. Although the slope at the critical point cannot be accurately measured on these data, it is without any doubt smaller than unity—the value of the asymptotic slope in the deep localized regime $\ln g \rightarrow -\infty$. This implies that the critical exponent ν is larger than unity. Recent numerical studies on much larger systems fully confirm this point, the current best estimate being $\nu = 1.58 \pm 0.01$ [26, 27].

Direct experimental observation of Anderson localization in 3d is even more difficult than in 2d, because it requires an even more strongly scattering system (kl smaller than 1 from the Ioffe-Regel criterion, eq. (57), instead of kl of the order of few units). Moreover, creation of a sufficiently disordered potential can be technically much more difficult in 3d: for a speckle potential, this would require to send plane waves with random phases from a large solid angle. Thus, Anderson localization of atomic matter waves in a disordered potential has not yet been observed. However, using the equivalence of a quasi-periodically kicked rotor with a 3d Anderson model, the Anderson transition with atomic matter waves has been observed, and its critical exponent experimentally measured, as discussed in section 8.

Electronic transport in solids, the field where localization theory was originally developed, provides also interesting experimental results. Metal-insulator transitions can be observed in solid state samples, but it is never easy to identify the microscopic mechanism. This is because electron-electron interactions play an essential role. Whether the observed transition is a one-body effect like the Anderson transition or a many-body one like the Mott transition [41] is not

easily proved. We are not aware of any unambiguous observation of the pure Anderson transition. Figure 15 shows the experimentally measured conductivity of a Si-doped AlGaAs crystal vs. a parameter essentially representing the electronic Fermi energy. A clear insulator-to-metal transition is observed. It seems that the curve is almost linear in the metallic regime, which—because conductivity is essentially a measure of the diffusion constant—means that the measured critical exponent is $\nu \approx 1$. This markedly differs from the exponent of the pure Anderson transition, indicating that interaction effects are probably important.

One may also turn to other type of waves, for example ultrasonic waves [42] or electromagnetic waves. Direct measurement of the electromagnetic field inside the disordered medium is not straightforward, and transmission experiments are easier. As mentioned earlier, absorption induces an exponential decay of the intensity, which must be carefully discriminated from the same effect being produced by Anderson localization. Thus, experimentalists have turned to measuring tell-tale properties right at the critical point. There, according to scaling theory, the dimensionless conductance has the constant value g_c , independently of the system size, whereas the classical dimensionless conductance, eq. (45), increases linearly with the system size L . This additional power of L makes the total transmission across the sample evolve from a $1/L$ behavior (Ohm's law) in the diffusive regime to a $1/L^2$ scaling law at the critical point, and eventually to the exponential decay in the localized regime. Any spurious absorption is likely to transform the critical $1/L^2$ behavior into an exponential decrease. Thus, the existence of an $1/L^2$ may be considered a sensitive test of observing the Anderson transition. Fig. 16 shows the experimental result obtained on the propagation of microwaves in a disordered medium, in the diffusive and critical regimes. The existence of a range with $1/L^2$ power law—before absorption wins at even larger size—is a convincing proof.

Similar results have been obtained in the optical regime [43], where strong scattering is provided by oxide powders, but the role of absorption has been discussed controversially [44]. Recently, time-resolved transmission experiments, where absorption has less impact, have shown a slowing down of classical transport [45], which gives strong evidence for Anderson localization.

In the last few years, several numerical and laboratory experiments have characterized the fluctuations appearing in the vicinity of the Anderson transition. In particular, numerical experiments on the 3d Anderson model have shown that the critical eigenstates have a multi-fractal structure, implying the coexistence of regions where the wavefunction is exceptionally large together with regions where it is exceptionally small. This is presently a very active field of research [47], whose description is beyond the scope of these lectures. The reader may refer to the recent review paper of Evers and Mirlin [15]. In the near future, it is very likely that experiments on localization of atomic matter waves will concentrate on the existence and properties of fluctuations.

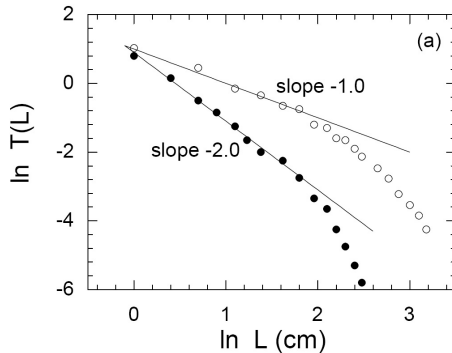


Figure 16: Experimentally measured transmission of microwaves through a 3d strongly scattering medium vs. the size of the medium (doubly logarithmic scale). In the usual diffusive regime (open symbols), a $1/L$ decrease is observed, in agreement with classical transport theory (Ohm’s law). At the critical point of the Anderson transition (filled symbols) a characteristic $1/L^2$ behavior is observed, in agreement with the scaling theory of localization. Note that, because of residual absorption, the signal drops at large size. Reprinted from [46] (courtesy of A.Z. Genack).

5 Microscopic description of quantum transport

5.1 Diagrammatic perturbation theory

In section 2, we have seen that localization in (quasi-)one-dimensional systems can be very efficiently described by a transfer-matrix approach. In higher dimensions, we have resorted to the scaling arguments presented in section 3. We now wish to give an introduction to a microscopic description of quantum transport in disordered systems. The main advantage of diagrammatic perturbation theory lies in its versatility. It applies in arbitrary dimensions d and to any model with a Hamiltonian of the form

$$H = H_0 + V, \quad (69)$$

in which H_0 describes regular propagation in an ordered substrate, and V is the disorder potential that breaks translational invariance. On a microscopic level, “disorder” refers to degrees of freedom whose detailed dynamics are not of interest and whose properties are only known statistically. In the following, we will consider *static* or *quenched* disorder that remains frozen on the timescale of wave propagation under study (as sole exception of this rule, we mention in section 6.3 the dephasing effect of moving impurities).

A first model of type (69) describes a single quantum particle in an external potential,

$$H = \frac{p^2}{2m} + V(r), \quad (70)$$

with direct bearing on experiments with non-interacting matter waves like [4], but equally applicable to other massive particles like electrons, neutrons, etc. Note that the plain Hamiltonian (70) operating in Hilbert space describes the

same single-particle physics as the more fanciful many-body version

$$H = \int d^d r \Psi^\dagger(r) \left[-\frac{\hbar^2}{2m} \nabla^2 + V(r) \right] \Psi(r), \quad (71)$$

defined in terms of particle creation and annihilation operators $\Psi^{(\dagger)}$ in Fock space.

Since we assume that H_0 is translation-invariant (if only by discrete translation on a lattice), the following equivalent formulation in Fourier space is also useful:

$$H = \sum_k \varepsilon_k^0 a_k^\dagger a_k + \sum_{k,q} V_q a_{k+q}^\dagger a_k. \quad (72)$$

Here, wave vectors k are used as good quantum numbers labeling the eigenstates of H_0 . If there is an underlying lattice, one has to include also a Bloch band index. ε_k^0 is the free dispersion relation; for matter waves, $\varepsilon_k^0 = \hbar^2 k^2 / 2m$. Particle annihilators $a_k = L^{-d/2} \int d^d r e^{ik \cdot r} \Psi(r)$ and creators a_k^\dagger fulfill the canonical commutation relations $[a_k, a_{k'}^\dagger]_\pm = \delta_{kk'}$.

The disorder potential breaks translation invariance by scattering particles $k \rightarrow k'$ with an amplitude given by its Fourier component $V_q = \langle k+q | V | k \rangle = L^{-d} \int d^d r e^{-iq \cdot r} V(r)$, conveniently represented by

$$V_q = \begin{array}{c} \vdots \\ \downarrow q \\ \bullet \\ \swarrow k \quad \searrow k+q \end{array} . \quad (73)$$

This model Hamiltonian (72) is not limited to matter waves. By appropriate changes in ε_k^0 , different physical systems can be described. For instance, photons and other mass-less excitations have a linear dispersion $\varepsilon = \hbar c k$ with characteristic speed c . Yet another realization is provided by the elementary excitations of Bose-Einstein condensates, featuring the Bogoliubov dispersion $\varepsilon_k = \sqrt{\varepsilon_k^0 (\varepsilon_k^0 + 2\mu)}$, that interpolates between a linear sound-wave dispersion at low energy and a quadratic particle-like dispersion $\varepsilon_k^0 = \hbar^2 k^2 / 2m$ at high energy. The general formalism to be introduced below applies to all these cases, provided the scattering potential V_q is known.

The basic model can be made richer, depending on the circumstances and effects one wishes to describe. For example, spin often plays an important role, for instance via spin-orbit effects, due to coupling of spin and direction of propagation. Also spin-flip processes can be of interest, as in electronic spin-flips induced by magnetic impurities or photon polarization flips induced by Zeeman-degenerate atomic dipole transitions. A typical spin-flip process $(m, \sigma) \mapsto (m', \sigma')$ changes the spin of the propagating object from σ to σ' , while the impurity spin undergoes $m \mapsto m'$. Processes of this type can store information about the path traveled, and generally act as a source of strong decoherence (as discussed in Sec. 6.3 below).

The main drawback of the diagrammatic Green function approach is its perturbative character. Most results are obtained from an expansion in powers of V and are valid only for small enough potential strength. If one is interested in truly strong-disorder effects, it may be worthwhile to start from the opposite situation where the propagation described by H_0 is small; Anderson's

original method of a “locator expansion” [5] is an example for such a weak-coupling perturbative approach. In any case, it takes considerable effort to derive non-perturbative results using controlled approximations. Yet, the basic diagrammatic technique is a prerequisite for more powerful, field-theoretic methods involving, e.g., replica methods, renormalization-group analysis and supersymmetry [48].

5.1.1 Quantum propagator

Let us then start by calculating the Green function for the single-particle Hamiltonian (70) that determines the time evolution of a state $|\psi\rangle$ in Hilbert space according to the Schrödinger equation $i\hbar\partial_t|\psi\rangle = H|\psi\rangle$. For $t > 0$, the forward-time evolution operator $G^{\text{R}}(t) = -\frac{i}{\hbar}\theta(t)\exp\{-iHt/\hbar\}$ solves the differential equation

$$[i\hbar\partial_t - H]G^{\text{R}}(t) = \delta(t). \quad (74)$$

Obviously, $G^{\text{R}}(t)$ is the retarded Green operator for the Schrödinger equation. It encodes the same information than its many-body version $G_{kk'}^{\text{R}}(t) = -\frac{i}{\hbar}\theta(t)\langle [a_k(t), a_{k'}^\dagger] \rangle$ that one would use starting from (72); in the following, we stick to the simpler form, referring the reader to the literature for the more advanced presentation [49, 50, 51, 52]. Going from time to energy by Fourier transformation, one defines the *resolvent*

$$G^{\text{R}}(E) = \lim_{\eta \rightarrow 0^+} \int dt e^{i(E+i\eta)t/\hbar} G^{\text{R}}(T) = \lim_{\eta \rightarrow 0^+} [E - H + i\eta]^{-1} =: [E - H + i0]^{-1}. \quad (75)$$

The limiting procedure $\eta \rightarrow 0^+$ guarantees that indeed the retarded Green operator is obtained, different from zero only for $t > 0$. The advanced Green operator $G^{\text{A}}(t)$ is obtained by taking $\eta \rightarrow 0^-$. In the basis where H is diagonal, $H|n\rangle = \varepsilon_n|n\rangle$, the resolvent is also diagonal and thus admits the spectral decomposition $G(z) = \sum_n |n\rangle [z - \varepsilon_n]^{-1} \langle n|$ for any argument $z \in \mathbb{C}$ outside the spectrum of H . The resolvent’s matrix elements are called “propagators”. For example, in the position representation $\langle r|n\rangle = \psi_n(r)$,

$$G^{\text{R}}(r, r'; E) = \langle r'|G^{\text{R}}(E)|r\rangle = \sum_n \frac{\psi_n(r')\psi_n^*(r)}{E - \varepsilon_n + i0} = r \longrightarrow r'. \quad (76)$$

This propagator contains precious information: As function of E , it has singularities on the real axis that are precisely the spectrum of H and thus encode all possible evolution frequencies. Furthermore, the residues at these poles provide information about the eigenfunctions.

The total Hamiltonian (70) contains the disorder potential so that we cannot write down its eigenfunctions and eigenvalues analytically (numerically, one may of course calculate eigenfunctions and eigenvalues for each realization of disorder). We start therefore with the free Hamiltonian H_0 . Its resolvent $G_0(z) = [z - H_0]^{-1}$ is diagonal in momentum representation, $\langle k'|G_0(z)|k\rangle = \delta_{kk'}G_0(k, z)$ with

$$G_0^{\text{R}}(k; E) = \frac{1}{E - \varepsilon_k^0 + i0} = \xrightarrow{k}. \quad (77)$$

Now we are ready to describe the perturbation due to the potential V : Using $G(E) = [E - H_0 - V]^{-1} = [(E - H_0)\{1 - (E - H_0)^{-1}V\}]^{-1}$, we express

$$G(E) = [1 - G_0V]^{-1}G_0 \quad (78)$$

$$= G_0 + G_0VG_0 + G_0VG_0VG_0 + \dots \quad (79)$$

as the Born series in powers of V . For notational brevity, we have already suppressed the energy argument on the right-hand side. Still, if one tries to write out a matrix element $\langle k'|G(E)|k\rangle$, the operator products convert into cumbersome expressions that tend to obscure the series' simple structure:

$$\langle k'|G(E)|k\rangle = \delta_{kk'}G_0(k) + G_0(k')V_{k'-k}G_0(k) + \sum_{k''} G_0(k')V_{k'-k''}G_0(k'')V_{k''-k}G_0(k) + \dots \quad (80)$$

At this point, we are well advised to use the graphical representation known as ‘‘Feynman diagrams’’, for which we have already all ingredients at hand:

$$\langle k'|G(E)|k\rangle = \delta_{kk'} \xrightarrow{k} + \xrightarrow{k} \bullet \xrightarrow{k'} + \xrightarrow{k} \bullet \xrightarrow{k''} \bullet \xrightarrow{k'} + \dots \quad (81)$$

Already, we achieve a much more compact notation, aided by the fact that we do not need to label the dangling impurity lines, defined in (73), since their momentum is automatically determined by the incident and scattered momenta. Also, we henceforth use the prescription that all internal momenta have to be summed over, here k'' in the last contribution.

5.1.2 Ensemble average

In principle, the Born series (81) permits to calculate the full propagator perturbatively. However, the result will be different for each realization of disorder. We are really only interested in suitable expectation values and thus have to understand how to perform the ensemble average over the disorder distribution.

The potential $V(r)$ as a function fluctuating in space is a *random process*. As such, it can be completely characterized by its moments or correlation functions $\langle V_1 \rangle$, $\langle V_1V_2 \rangle$, $\langle V_1V_2V_3 \rangle$, etc., with the short-hand notation $V_i = V(r_i)$. We will assume that the process is *stationary* or, preferring the spatial dictionary, *statistically homogeneous*, which means that correlation functions can only depend on coordinate differences $r_{ij} = r_i - r_j$. We can therefore define the following correlation functions and corresponding diagrams:

$$\langle V_1 \rangle = \langle V \rangle \quad (82)$$

$$\langle V_1V_2 \rangle = P(r_{12}) = \begin{array}{c} \bullet \cdots \bullet \\ | \quad | \\ 1 \quad 2 \end{array} \quad (83)$$

$$\langle V_1V_2V_3 \rangle = T(r_{12}, r_{23}) = \begin{array}{c} \bullet \cdots \bullet \cdots \bullet \\ | \quad | \quad | \\ 1 \quad 2 \quad 3 \end{array} \quad (84)$$

and so on for arbitrary n -point correlation functions. Without loss of generality, one may always take $\langle V \rangle = 0$ by defining a centered potential $V \mapsto V - \langle V \rangle$ while redefining the zero of energy $E - \langle V \rangle \mapsto E$. In Fourier representation,

these correlation functions are

$$P(q) = \begin{array}{c} \text{---} q \text{---} \\ \bullet \quad \bullet \\ \vdots \quad \vdots \end{array}, \quad T(q, q') = \begin{array}{c} \text{---} q \text{---} \quad \text{---} q' \text{---} \\ \bullet \quad \bullet \quad \bullet \\ \vdots \quad \vdots \quad \vdots \end{array}, \quad \text{etc.} \quad (85)$$

Depending on the specific type of disorder, these general correlation functions can take different forms, and it may be instructive to discuss two of them in detail.

5.1.3 Gaussian disorder

As a first example, let us consider Gaussian-distributed disorder that is completely defined by its first two moments $\langle V \rangle = 0$ and $P(r) = V_0^2 C(r)$. Here, one conveniently factorizes the one-point variance $V_0^2 = \langle V_1^2 \rangle$ from the spatial correlation function $C(r)$ that obeys $C(0) = 1$ by construction. The characteristic property of a Gaussian process is that all higher-order correlation functions completely factorize into pair correlations. Indeed, a simple property of the Gaussian integral implies that the moments of a normally distributed, centered scalar random variable X are $\langle X^{2n} \rangle = \mathcal{C}_n \langle X^2 \rangle^n$ where $\mathcal{C}_n = (2n)!/(2^n n!)$ is the number of pairs that can be formed out of $2n$ individuals. Similarly, the Gaussian moment theorem applies to a Gaussian-distributed random potential:

$$\langle V_1 \cdots V_{2n} \rangle = \frac{1}{2^n n!} \sum_{\pi} \langle V_{\pi(1)} V_{\pi(2)} \rangle \cdots \langle V_{\pi(2n-1)} V_{\pi(2n)} \rangle \quad (86)$$

where π denotes the $(2n)!$ permutations. Pictorially, this implies also a complete factorization of $2n$ -point potential correlation into products of pair correlations. The first interesting example is $n = 2$ with

$$\begin{array}{c} \text{---} \text{---} \text{---} \text{---} \\ \bullet \quad \bullet \quad \bullet \quad \bullet \\ \vdots \quad \vdots \quad \vdots \quad \vdots \end{array} = \begin{array}{c} \text{---} \text{---} \\ \bullet \quad \bullet \\ \vdots \quad \vdots \end{array} + \begin{array}{c} \text{---} \text{---} \text{---} \\ \bullet \quad \bullet \quad \bullet \\ \vdots \quad \vdots \quad \vdots \end{array} + \begin{array}{c} \text{---} \text{---} \\ \bullet \quad \bullet \\ \vdots \quad \vdots \end{array} \quad (87)$$

and so on for higher orders.

Such a Gaussian potential can be constructed with arbitrary spatial correlation $C(r)$. A popular choice here is often to model it as a Gaussian as well, $C(r) = \exp\{-r^2/2\sigma^2\}$, such as in [53], because this is easy to implement numerically (it suffices to draw uncorrelated random variables V_i on a discrete grid and convolute by a Gaussian correlation function afterwards). Moreover, this choice leads to simple analytical calculations because also the k -space pair correlator is Gaussian, $P(q) = V_0^2 \sigma^d (2\pi)^{d/2} \exp\{-q^2 \sigma^2/2\}$. In the limit of low momenta $q\sigma \ll 1$, the potential details cannot be resolved and it appears δ -correlated. Then, everything can be expressed in terms of $P(0) = (2\pi)^{d/2} \sigma^d V_0^2$.

5.1.4 Speckle

A slightly more interesting example is provided by the optical speckle potential used recently for matter-wave Anderson localization [4, 54]. The atoms are subject to an optical dipole potential $V(r) = K|E(r)|^2$ created by the local field intensity of far-detuned laser light. K contains the frequency-dependent atomic polarizability besides some constants [55]. With a laser beam that is blue-detuned from the optical resonance, one has $K > 0$ and thus expells atoms from high-intensity regions. This potential landscape features repulsive peaks

with $\langle V \rangle > 0$. Conversely, a red-detuned laser leads to $K < 0$, and one finds a potential landscape with attractive wells and $\langle V \rangle < 0$. To create a disorder potential, the laser beam is focused through a diffuse glass plate, whose randomly positioned individual grains act as elementary sources for the emitted field. The electric field $E(r)$ at some far point then is the sum of a large number of complex amplitudes. By virtue of the central limit theorem, it is a *complex Gaussian random variable* with normalized pair correlator

$$\gamma_{ij} = \gamma(r_i - r_j) = \frac{\langle E^*(r_i)E(r_j) \rangle}{\langle |E|^2 \rangle} = \overset{*}{i} \overset{\circ}{j} \quad (88)$$

with the obvious properties $\gamma_{ij}^* = \gamma_{ji}$ and $\gamma_{ii} = 1$. In a 1d-geometry, the pair correlator takes its simplest form in Fourier components:

$$\gamma(q) = \pi\zeta\Theta(1 - |q|/k_\zeta) \quad (89)$$

where $k_\zeta = k\alpha$ is the maximum wave-vector that can be built from a monochromatic laser source with wave vector k seen under an optical aperture α . This eqn (89) simply says that the random field contains all wave vectors inside the allowed interval with equal weight. In real space, this Fourier transforms to $\gamma(r) = \sin(r/\zeta)/(r/\zeta)$ with the correlation length $\zeta = 1/k_\zeta = 1/(\alpha k)$.

Other pair correlations such as $E_i E_j$ and $E_i^* E_j^*$ have uncompensated random phases and average to zero. The Gaussian moment decomposition now applies to arbitrary moments of the speckle disorder potential $V_i = K E_i^* E_i$. An n -point potential correlation is really a $(2n)$ -field correlation, which decomposes into all possible pair correlations (88). As in a conventional ballroom dancing situation involving n couples, all possible heterosexual pairings between the E_i^* s and E_j s are allowed. This gives for the 2-point potential correlator

$$\langle V_1 V_2 \rangle = K^2 \langle E_1^* E_1 E_2^* E_2 \rangle = \langle V \rangle^2 [\gamma_{11} \gamma_{22} + \gamma_{12} \gamma_{21}]. \quad (90)$$

Setting $r_1 = r_2$ shows that $\langle V^2 \rangle = 2\langle V \rangle^2$, which means that the potential variance is equal to its mean square, $\text{var}(V) = \langle V^2 \rangle - \langle V \rangle^2 = \langle V \rangle^2$.

The shift $V \mapsto V - \langle V \rangle$ to the centered potential removes the first term in the bracket in (90). The same applies to all diagrams with field self-contractions:

$$\overset{\circ}{\otimes} = 0. \quad (91)$$

So henceforth, we can neglect those diagrams by considering a centered potential $\langle V \rangle = 0$. Altogether, we have as a first building block the speckle potential pair correlator

$$\langle V_1 V_2 \rangle = P(r_{12}) = V_0^2 C(r_{12}) = V_0^2 \overset{\circ}{\otimes}_1 \overset{\circ}{\otimes}_2 \quad (92)$$

Here, the potential strength $V_0^2 = \text{var}(V)$ is factorized from the dimensionless correlation function $C(r) = |\gamma(r)|^2$ that is normalized to $C(0)=1$. In $d = 1$, from (89), we have the real-space intensity correlator $C(r) = [\sin(r/\zeta)/(r/\zeta)]^2$. In higher dimensions and in an isotropic setting, the Fourier transformation of the simple k -space field correlator yields $C(r) = [2J_1(r/\zeta)/(r/\zeta)]^2$ in $d = 2$ and $C(r) = [\sin(r/\zeta)/(r/\zeta)]^2$ again in $d = 3$ [34].

An interesting effect occurs for potential correlations of odd order $(2n + 1)$. They are really field correlation of twice the order, which is even and thus

different from zero. The first example of this kind is (since the fields $*$ and \circ will always appear together, we note $\otimes = \bullet$ from now on)

$$\langle V_1 V_2 V_3 \rangle = V_0^3 2\text{Re}\{\gamma_{12}\gamma_{23}\gamma_{31}\} = V_0^3 \begin{array}{c} \text{---} \bullet \text{---} \bullet \text{---} \bullet \text{---} \\ \text{---} \bullet \text{---} \bullet \text{---} \bullet \text{---} \\ \text{---} \bullet \text{---} \bullet \text{---} \bullet \text{---} \end{array} \quad (93)$$

Diagrams of this type can only contain closed loops of field correlations (because field self-contractions no longer appear). Since the loops can be closed both clockwise and counterclockwise, there are two contributions complex conjugate of each other.

5.1.5 Average propagator: self-energy

Now we are in position to take the ensemble average of the single-particle propagator (79):

$$\langle G \rangle = G_0 + G_0 \langle V G_0 V \rangle G_0 + G_0 \langle V G_0 V G_0 V \rangle G_0 + \dots \quad (94)$$

or

$$\langle G \rangle = \text{---} + \text{---} \bullet \text{---} \bullet \text{---} + \text{---} \bullet \text{---} \bullet \text{---} \bullet \text{---} + \dots \quad (95)$$

The precise form of potential correlations depends on the model of disorder. As shown by the example of the Gaussian model (87), starting from the fourth-order term there appear completely factorized contributions. Before writing all possible combinations down, we had better introduce one of the cornerstones of diagrammatic expansions: the *self-energy* $\Sigma(E)$ defined by the *Dyson equation*

$$\langle G \rangle = G_0 + G_0 \Sigma \langle G \rangle. \quad (96)$$

Introducing the self-energy invariably prompts the following frequently asked questions:

1. Why is the self-energy convenient for perturbation theory?
2. How do I calculate Σ ?
3. What is the physical meaning of Σ ?
4. Is there a simple example?

Let us answer them in turn.

1. By iterating the Dyson equation (96), one finds that the average propagator expands as

$$\langle G \rangle = \text{---} + \text{---} \textcircled{\Sigma} \text{---} + \text{---} \textcircled{\Sigma} \text{---} \textcircled{\Sigma} \text{---} + \text{---} \textcircled{\Sigma} \text{---} \textcircled{\Sigma} \text{---} \textcircled{\Sigma} \text{---} + \dots \quad (97)$$

By construction, there are no disorder correlations between the different self-energies appearing here. In return, this implies that the self-energy contains *exactly all* correlations that cannot be completely factorized by removing a free propagator G_0 in between. These non-factorizable terms are called “one-particle irreducible” (1PI). Moreover, the self-energy contains only the correlations and internal propagators, but is stripped off the external propagator lines (“amputated”). This makes the self-energy the simplest object describing all relevant disorder correlations.

2. Due to statistical homogeneity, the self-energy is diagonal in momentum and thus only depends on k and E . The self-energy matrix element $\Sigma(k, E)$ is calculated by applying so-called Feynman rules to evaluate the diagrams. As a specific example, let us give the Feynman rules for the self-energy of the retarded single-particle propagator $\langle G^{\text{R}}(k, E) \rangle$ in momentum representation for the case of the speckle potential:

- (i) Draw all amputated 1PI diagrams with incident momentum k :

$$\Sigma(k, E) = \text{---}\overset{\text{---}}{\curvearrowright}\text{---} + \text{---}\overset{\text{---}}{\curvearrowright}\text{---} + \dots \quad (98)$$

- (ii) Convert straight black lines to free propagators

$$\text{---}\underset{k}{\text{---}} = G_0^{\text{R}}(k, E) = [E - \varepsilon_k^0 + i0]^{-1}.$$

- (iii) Convert disorder correlation lines to $\bullet \overset{q}{\text{---}} \bullet = \gamma(q)$. The precise functional dependence $\gamma(q)$ depends on dimension and geometry.

- (iv) For each scattering vertex, multiply by one power of the potential strength and the conservation of momentum:

$$\text{---}\underset{k}{\text{---}} \overset{q}{\text{---}} \overset{q'}{\text{---}} \text{---}\underset{k'}{\text{---}} = V_0 \delta_{k+q, k'+q'} \quad (99)$$

- (v) Sum over all free momenta after respecting momentum conservation.

For other types of disorder, these rules have to be adapted slightly to the precise shape of diagrams, correlation functions and vertex factors. But in all cases, the general idea of writing all possible combinations, respecting momentum conservation and integrating out the free momenta is the same.

3. One can rewrite the Dyson equation (96) as $[1 - G_0 \Sigma] \langle G \rangle = G_0$ and solve formally for the average propagator: $\langle G \rangle = [1 - G_0 \Sigma]^{-1} G_0 = [G_0^{-1} - \Sigma]^{-1}$. Thus, its matrix elements are

$$\langle G^{\text{R}}(k, E) \rangle = \frac{1}{E - \varepsilon_k^0 - \Sigma(k, E)}. \quad (100)$$

We recognize that the self-energy modifies the free dispersion relation. Generally, the self-energy is a complex quantity with a real as well as an imaginary part. The *modified dispersion relation*

$$E_k = \varepsilon_k^0 + \text{Re}\Sigma(k, E_k) \quad (101)$$

is an implicit equation for the new eigen-energy E_k of the mode k . So one effect of the disorder is to shift the energy levels.⁴ But plane waves with fixed k are no longer proper eigenstates of the disordered system. This is encoded in

⁴Alternatively, one can also solve for k_E as the modified k -vector of an excitation with given energy E .

the imaginary part. Writing $\Gamma_k = -2\text{Im}\Sigma(k, E_k)$ and using the fact that the self-energy varies smoothly with k and E , one finds a *spectral density*

$$A(k, E) = -2\text{Im}\langle G^{\text{R}}(k, E) \rangle = \frac{\Gamma_k}{(E - E_k)^2 + \Gamma_k^2/4}. \quad (102)$$

This spectral function is the probability density that an excitation k has energy E . Its wave-number integral is the average density of states per unit volume,

$$N(E) = \frac{1}{2\pi} \int \frac{d^d k}{(2\pi)^d} A(k, E). \quad (103)$$

For the free Hamiltonian, $A_0(k, E) = 2\pi\delta(E - \varepsilon_k^0)$. The disorder introduces a finite spectral width Γ_k , which translates into a finite lifetime $\hbar\Gamma_k^{-1}$. Equivalently, this finite lifetime translates into a finite scattering mean-free path l_s for the spatial matrix elements of the average propagator,

$$\langle G(r - r', E) \rangle = \int \frac{d^d k}{(2\pi)^d} e^{ik \cdot (r' - r)} \langle G(k, E) \rangle = G_0(r - r', E) e^{-|r' - r|/2l_s}, \quad (104)$$

showing an exponential decay with $l_s = k\Gamma_k/(2E)$ evaluated at $k = \sqrt{2mE}/\hbar$.

4. The simplest possible example is the calculation of the lifetime from the lowest-order, so-called *Born approximation*

$$\Sigma(k, E) = \begin{array}{c} \xrightarrow{k-k'} \\ \bullet \xrightarrow{k} \bullet \xrightarrow{k'} \bullet \xrightarrow{k} \bullet \end{array} \quad (105)$$

for some potential with correlation function $P(q)$. To lowest order in V_0 , we can use $E_k = \varepsilon_k^0$ and thus find

$$\frac{\Gamma_k}{2\varepsilon_k^0} = \frac{1}{kl_s} = \pi \int \frac{d^d k'}{(2\pi)^d \varepsilon_k^0} P(k - k') \delta(\varepsilon_k^0 - \varepsilon_{k'}^0) = \frac{\pi P(0) N_0(\varepsilon_k^0)}{\varepsilon_k^0} \quad (106)$$

in terms of the free density of states $N_0(\varepsilon)$ and the low- k limit $P(0)$ of potential correlation, eq. (85), that is appropriate for the δ -correlated limit. This is precisely the result that one gets from a straightforward application of Fermi's Golden Rule for the average probability of scattering out of the mode k by the external potential V_q . The interest of the full-fledged diagrammatic expansion is of course that one is in principle able to calculate corrections to the lowest-order estimate, and to tackle more complicated potentials. There exist literally hundreds of other applications in the most diverse physical systems. Let us mention two examples from our own experience.

For two-dimensional Gaussian correlated potentials such as the one introduced in section 5.1.3, the scattering rate evaluates to

$$\frac{1}{kl_s} = \frac{\Gamma_k}{2\varepsilon_k^0} = \frac{2\pi V_0^2}{k^2 \sigma^2 E_\sigma^2} e^{-k^2 \sigma^2} I_0(k^2 \sigma^2) \quad (\text{Gauss}, d = 2) \quad (107)$$

where $E_\sigma = \hbar^2/m\sigma^2$ is a characteristic correlation energy and I_0 a modified Bessel function.

For matter waves in a one-dimensional speckle potential, we can use (105) and (106) with the speckle potential correlation function (92). In $d = 1$, the only contributions can come from forward scattering $k' = k$ and backward scattering $k' = -k$, such that

$$\frac{1}{kl_s} = \frac{\Gamma_k}{2\varepsilon_k^0} = \frac{V_0^2 k}{\varepsilon_k^0{}^2} [P(0) + P(2k)] \quad (\text{speckle, } d = 1) \quad (108)$$

in terms of the k -space pair correlator $P(2k) = \pi\zeta(1 - |k\zeta|) \Theta(1 - |k\zeta|)$.

The estimates (107) and (108) can only be trusted if $\Gamma_k/\varepsilon_k^0 \ll 1$ or equivalently $kl_s \gg 1$, otherwise the assumption of a small correction to the free dispersion is no longer valid. Since the scattering rates diverge at low k , we find that the perturbative approach breaks down at low energy. A closer analysis shows that a sufficient criterion for weak disorder is $E_k \gg V_0^2/E_\sigma$ [34].

Sometimes, also the real part of the self-energy is of importance. For example, one can calculate the speed of sound in interacting Bose-Einstein condensates, and especially the shift due to correlated disorder by the same Green function formalism [56]. Incidentally, for sound waves the scattering mean-free path grows as $k \rightarrow 0$, and the perturbative approach stays valid even at very low energy.

5.2 Intensity transport

We would like to calculate the ensemble-averaged density $n(r, t) = \langle\langle r|\rho(t)|r\rangle\rangle$ (or, its many-body form $\langle\langle \Psi^\dagger(r)\Psi(r)\rangle\rangle$) in the limit of long time. In the Schrödinger picture, the state evolves as $\rho(t) = U^\dagger(t)\rho_0 U(t)$. After transforming the time evolution operators to Green functions as in (75), we need a theory for the ensemble-averaged product $\langle G^A(E)G^R(E')\rangle$. This is known as the average intensity propagator. In most experimental situations—be it with electromagnetic or matter waves—one measures intensities (see for example the average transmission through a 1d disordered system of length L studied in section 2); the average intensity propagator is thus the fundamental quantity of interest. Before going into details, we propose to have a look at what we should expect to be the result.

5.2.1 Density response

The generic behavior that one may expect for transport in a disordered environment is *diffusion*. Indeed, diffusion follows from two very basic and rather innocuous hypotheses. Firstly, one generally has a local conservation law, for instance for particle number, taking the form of a *continuity equation*:

$$\partial_t n + \nabla \cdot j = s \quad (109)$$

where $j(r, t)$ is the current density associated with $n(r, t)$, and $s(r, t)$ is some source function. Secondly, one assumes a *linear response* in the form of Fourier's law

$$j = -D\nabla n, \quad (110)$$

saying that a density gradient induces a current that tries to reestablish global equilibrium. The diffusion constant D appears here as a linear response coefficient. Inserting (110) into (109), we immediately find as a consequence the

diffusion equation

$$[\partial_t - D\nabla^2]n(r, t) = s(r, t). \quad (111)$$

This equation can be solved by Fourier transformation⁵. The solution for a unit source $s(r, t) = \delta(r)\delta(t)$ is the Green function for this problem, viz., the density relaxation kernel

$$\Phi_0(q, \omega) = \frac{1}{-i\omega + Dq^2}. \quad (112)$$

Its temporal version

$$\Phi_0(q, t) = \int \frac{d\omega}{2\pi} e^{-i\omega t} \Phi_0(q, \omega) = \theta(t) \exp\{-Dq^2 t\} \quad (113)$$

shows that the relaxation $\exp\{-t/\tau_q\}$ with characteristic time $\tau_q = 1/Dq^2$ becomes very slow in the large-distance limit $q \rightarrow 0$ because of the local conservation law. In real space and time, the relaxation kernel reads

$$\Phi_0(r, t) = \int \frac{d^d q}{(2\pi)^d} e^{iq \cdot r} \Phi_0(q, \omega) = \theta(t) [4\pi Dt]^{-d/2} \exp\{-r^2/4Dt\}. \quad (114)$$

This relaxation kernel describes diffusive spreading with $\langle r^2 \rangle = 2dDt$.

This is the “hydrodynamic” description of dynamics on large distances and for long times, accessed by small momentum q and frequency ω . A microscopic theory is then only required to calculate the linear response coefficient D .

5.2.2 Quantum intensity transport

In complete analogy to the Dyson equation (96) for the average single-particle propagator, one may write a structurally similar equation for the intensity propagator $\Phi = \langle G^R G^A \rangle$, known as the Bethe-Salpeter equation:

$$\Phi = \langle G^R \rangle \langle G^A \rangle + \langle G^R \rangle \langle G^A \rangle U \Phi. \quad (115)$$

Here, one splits off the known evolution with uncorrelated, average amplitudes

$$\langle G^R(k, E) \rangle \langle G^A(k', E') \rangle = \frac{\overrightarrow{k}}{\overleftarrow{k'}}. \quad (116)$$

The upper part of intensity diagrams describes the retarded propagator, called “particle channel” in condensed-matter jargon, whereas the lower part contains the advanced propagator or “hole channel”. All scattering events that couple these amplitudes are contained in the intensity scattering operator U . By construction, this “particle-hole irreducible” vertex contains exactly all diagrams that cannot be factorized by removing a propagator pair (116). Its detailed form again depends on the model of disorder. In all cases, $U_{kk'}(E)$ is essentially

⁵which was invented right for this purpose by Joseph Fourier, namesake of the French university in Grenoble hosting the Les Houches school.

the differential cross-section for scattering from k to k' and generally has the following structure:

$$U(k, k'; E) = \begin{array}{c} \begin{array}{ccc} k \rightarrow & & k' \\ \leftarrow & & \leftarrow \\ k & & k' \end{array} \\ \text{---} \end{array} = \begin{array}{c} \bullet \\ \vdots \\ \bullet \end{array} + \begin{array}{c} \bullet \quad \bullet \\ \text{---} \\ \bullet \quad \bullet \\ \vdots \\ \bullet \quad \bullet \end{array} + \begin{array}{c} \bullet \quad \bullet \\ \text{---} \\ \bullet \quad \bullet \\ \vdots \\ \bullet \quad \bullet \end{array} + \begin{array}{c} \bullet \quad \bullet \\ \text{---} \\ \bullet \quad \bullet \\ \vdots \\ \bullet \quad \bullet \end{array} + \dots \quad (117)$$

Linear-response theory shows that this scattering vertex permits to calculate the transport mean-free path l , in close analogy to the calculation of the scattering mean-free path l_s from the self-energy. Their ratio is expressed as

$$\frac{l_s}{l} = 1 - \langle \cos \theta \rangle_U \quad (118)$$

where θ is the scattering angle between k and k' , and the brackets $\langle \cdot \rangle_U$ indicate an average over the scattering cross-section U . The physical interpretation of the transport mean free path l is the following: while the scattering mean free path l_s measures the distance after which the memory of the initial phase of the wave is lost, l is the distance over which the direction of propagation is randomized.

5.2.3 Diffusion

The scattering processes encoded in U are perhaps more easily visualized in real space. We will draw a full line for every amplitude ψ propagated by G^R (upper lines in (117)) and a dashed line for every ψ^* propagated by G^A (lower lines in (117)). Impurities are represented by black dots as before. Then, the first contribution to U describes the single-scattering process

$$U_B : \begin{array}{c} r \\ \swarrow \\ \bullet \\ \searrow \\ r_1 \\ \swarrow \\ \bullet \\ \searrow \\ r' \end{array} \quad (119)$$

in which both ψ and ψ^* are being scattered by the same impurity at position r_1 . This process is insensitive to phase variations and could just as well take place for classical particles. So this Boltzmann contribution U_B describes classical diffusion with diffusion constant

$$D_B = \frac{vl_B}{d} \quad (120)$$

The Boltzmann transport mean-free path is calculated by inserting $U_{Bkk'} = V_0^2 P(k - k')$ into (118):

$$\frac{l_s(k)}{l_B(k)} = 1 - \frac{\int d\Omega_d \cos \theta P(2k|\sin(\theta/2)|)}{\int d\Omega_d P(2k|\sin(\theta/2)|)} \quad (121)$$

Depending on the microscopic scattering process, l_B can be longer than l_s , if forward scattering is dominant, $\langle \cos \theta \rangle_{U_B} > 0$. This is the case for matter waves in spatially correlated potentials. For isotropic scattering with $\langle \cos \theta \rangle_{U_B} = 0$, these two length scales coincide, $l_s = l_B$.

By combining eq. (121) with eq. (106) giving the scattering mean free path, one can easily compute, in the Born approximation, the transport mean free path and consequently the classical Boltzmann diffusion constant, using only microscopic ingredients: the dispersion relation of the free wave and the correlation function of the scattering potential.

5.2.4 Localization length in 1d systems

As we have already seen repeatedly in previous sections, in 1d the transport mean free path is (up a factor 2) equal to the localization length, $\ell = \xi_{\text{loc}}/2$, an identity that can also be verified microscopically [57], at least to lowest order V_0^2 in perturbation theory.⁶ So now we are in a position to give a microscopic prediction for the 1d localization length for arbitrarily correlated potentials, namely taking twice the backscattering contribution from (108), selected by the $(1 - \cos \theta)$ -factor in (121):

$$\frac{1}{k\xi_{\text{loc}}} = \frac{V_0^2 k}{4\varepsilon_k^0{}^2} P(2k). \quad (122)$$

Figure 17, taken from [4], shows this prediction for $L_{\text{loc}} = 2\xi_{\text{loc}}$ as a dashed line together with the results of a fit to the intensity measured in the real experiment (see Fig. 8). Here $P(2k) = \pi\zeta(1 - k_{\text{max}}\zeta)\Theta(1 - k_{\text{max}}\zeta)$ with k_{max} the largest k -value present in the expanding wave packet, resulting in:

$$\xi_{\text{loc}} = \frac{\hbar^4 k_{\text{max}}^2}{\pi m^2 V_0^2 \zeta (1 - k_{\text{max}}\zeta)}. \quad (123)$$

There is no adjustable parameter, and the agreement is rather satisfactory. Significant deviations are visible both for small disorder (there the localization length becomes too large and experimental limitations start to show) and for large disorder, where the lowest-order theoretical estimate, or Born approximation (123) becomes insufficient. Moreover, for strong disorder, atom-atom interaction for the strongly localized cloud may no longer be negligible and induce some delocalization.

An interesting scenario occurs in speckle potentials when the fastest atoms have a wave vector k_{max} larger than the most rapid spatial fluctuations, with wave vector $1/\zeta$. Then, $P(2k_{\text{max}}) = 0$, and (123) predicts *prima facie* $\xi_{\text{loc}} = \infty$ or absence of localization, which would signal the existence of a mobility edge in this 1d random potential, contradicting rigorous mathematical theorems stating that all states are exponentially localized [58]. In fact, exponential localization still prevails, but requires more than a single scattering event by the smooth random potential. Going to higher orders in perturbation theory, beyond the Born approximation, one can show in excellent quantitative agreement with numerics, that the localization length is always finite [21, 20]. However, for weak disorder, the localization length can become much larger than the system size, such that numerical or experimental results show an *apparent mobility edge*. For other types of long-range correlations, one does find mobility edges [59]. There seems to be no obvious way of deciding, for a certain class of potentials, whether true exponential localization exists or not, and correlated potentials are still actively investigated in different contexts, see [60] and references therein.

⁶Whether this holds to all orders in perturbation theory is to our knowledge an open, and also interesting question, especially in optical speckle potentials [20].

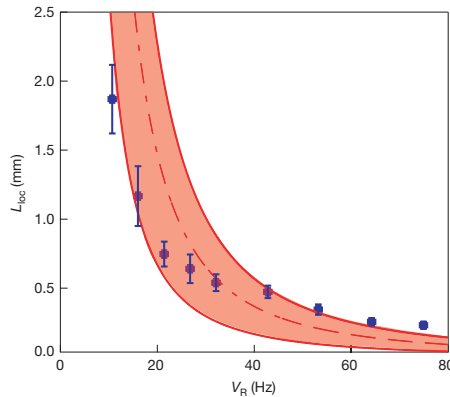


Figure 17: Comparison between the experimentally measured localization length for a quasi-1d atomic wave-packet launched in the disordered optical potential created by a speckle pattern, and the theoretical prediction, eq. (123), when the strength of the disordered potential is varied. There is no adjustable parameter. Reprinted from [4] (courtesy of Ph. Bouyer).

Despite the nice agreement shown in Fig. 17, some caution is indicated. The experimental observation involves averaging over k , and also over several different realizations of the disorder (single-shot results look similar, just more noisy). This means that the experimental data resembles the average transmission $\langle T(z) \rangle$ as a function of sample thickness z .⁷ In section 2.2.3, we showed that it is the *typical* transmission $T_{\text{typ}}(z) = \exp(\langle \ln T(z) \rangle)$ which decays exponentially, not the average transmission. At very large z , this can make a huge difference, see section 2.5. Fortunately, for z of the order of the localization length (t or order unity in the language of 2.5), the fluctuations have not yet built up, and the difference between the typical and the average value is still small, $\ln \langle T(z) \rangle \approx -z/\xi_{\text{loc}}$, making the pure exponential decay an acceptable approximation. Further in the wings, one expects deviations of the average density from a pure exponential decay, see eq. (38). This takes place however in the region where fluctuations are huge, so that a typical experiment may not measure the *average* value of the density, but rather its *typical* value.

5.2.5 Weak-localization correction

The first corrections to the classical, incoherent scattering process (119) shown in (117) involve one more scatterer and several possibilities of intermediate propagation. The most well-known type of correction stems from the diagram with

⁷The situation is actually more complicated, because this expansion experiment strictly speaking does not measure the transmission across a sample. Instead, one starts with an atomic density inside the medium and see how it propagates. The boundary conditions are thus different from those of a transmission experiment with its connection to outside leads. Still, huge fluctuations must exist in the localized regime, implying that the average transmission deviates from a pure exponential, as discussed in Section 2.5.

two crossed lines. In real space, the scattering process is



This is an interference correction with a phase shift $\Delta\varphi$ between ψ and ψ^* that depends on the impurity positions r_1 and r_2 . Contributions of this type are ensemble-averaged to zero—or rather, almost averaged to zero. Indeed, if the starting and final point of propagation come close, $r \approx r'$, the phase shift picked up by the two counter-propagating amplitudes becomes smaller:



At exact backscattering $r = r'$ and in the absence of any dephasing mechanisms, the phase difference is exactly zero. Vanishing phase difference means constructive interference and therefore enhanced backscattering probability to stay at the original position. This holds true no matter how many scatterers are visited on the path. One is led to consider all maximally crossed diagrams:

$$U_C = \begin{array}{c} \bullet \quad \bullet \\ \diagdown \quad \diagup \\ \bullet \quad \bullet \\ \diagup \quad \diagdown \\ \bullet \quad \bullet \end{array} + \begin{array}{c} \bullet \quad \bullet \quad \bullet \\ \diagdown \quad \diagup \quad \diagdown \\ \bullet \quad \bullet \quad \bullet \\ \diagup \quad \diagdown \quad \diagup \\ \bullet \quad \bullet \quad \bullet \end{array} + \dots \quad (126)$$

These diagrams were first considered in the electronic context [61] and became known as the *Cooperon* contribution. This contribution is peaked around backscattering $k = -k'$. Therefore, one may resort to a diffusion approximation and sum up all contributions with the help of the diffusion kernel (112):

$$\frac{1}{l} = \frac{1}{l_B} \left[1 + \frac{1}{\pi N_0} \int \frac{d^d q}{(2\pi)^d} \frac{1}{-i\omega + D_B q^2} \right]_{\omega \rightarrow 0} \quad (127)$$

Writing this in terms of the diffusion constant, one arrives at the weak-localization correction

$$\frac{1}{D} = \frac{1}{D_B} \left[1 + \frac{1}{\pi N_0 D_B} \int \frac{d^d q}{(2\pi)^d} \frac{1}{q^2 - i0} \right] \quad (128)$$

The quantum correction of the Cooperon makes $D < D_B$, and we have thus found the microscopic reason for the weak-localization correction that was first mentioned in the scaling section 3.5. Before looking in more details at this correction in section 7, we should like to understand it better by selectively probing the Cooperon contribution. In Optics, this is indeed possible and is developed in the next section.

6 Coherent backscattering (CBS)

One can probe the specific geometry of scattering paths like (124) by using a source of plane waves together with a collection of randomly positioned scatterers in a half-space geometry (fig. 18). Hereafter, we suppose normal incidence

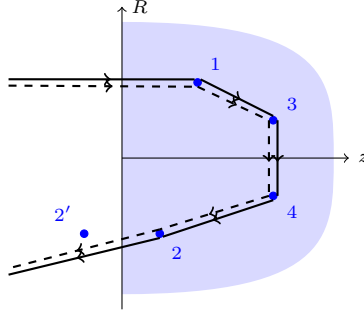


Figure 18: Half-space geometry of a backscattering experiment with cylindrical coordinates $r = (R, z)$. $2'$ is the image point of the exit scatterer 2 used to construct the half-space propagator for the incoherent intensity. As an example, the contribution of scattering from four scatterers is depicted.

and detection close to the backscattering direction; generalizing to arbitrary incident and detection angles changes nothing to the central argument.

6.1 Theory

The picture in Fig. 18 shows scattering by four impurities, contributing to the incoherently transported intensity. The corresponding intensity diagram is

(129)

The sum of all such diagrams with a distinct ladder topology yields the intensity propagator or *diffuson*, whose long-distance and long-time form is precisely the diffusion kernel (112), evaluated with the Boltzmann diffusion constant.

$$\Phi_B = \frac{1}{-i\omega + D_B q^2}. \quad (130)$$

The total back-scattered diffuse intensity per unit surface is given by summing contributions from all possible starting and end points:

$$I_L \propto \int dz_1 e^{-z_1/l_s} \int dz_2 e^{-z_2/l_s} \int d^2R \Phi_B(r_1, r_2). \quad (131)$$

The exponential attenuation factors describe the propagation of intensities from the surface to the first scatterer and back out again with average propagator $\langle G^R(z_i) \rangle$, (104), featuring the scattering mean free path l_s . Moreover, translation invariance along the surface direction has been used, leaving only the surface integral over the lateral distance $R = R_1 - R_2$.

The propagation inside an infinite disordered medium would occur with the bulk kernel (130) and thus have a time-integrated diffusion probability of $\Phi_B(r) = \int dt \Phi_B(r, t) = [4\pi D_B r]^{-1}$. This expression leads to a diverging integral over R in (131). But the starting and end points r_1 and r_2 lie rather close to the surface, namely typically one scattering mean-free path l_s away from it.

So for calculating the back-scattered intensity (131), we have to worry about appropriate boundary conditions. The complete integral equation for intensity propagation in a half-space geometry of a scalar wave and isotropic scatterers, known by the name Milne equation, can be solved exactly [62, 63], albeit with considerable mathematical effort. For a simple solution involving the diffusive bulk propagator valid far from the boundary, one can employ the method of images that is often used in electrostatics. Since photons reaching the surface would escape prematurely from the medium, one can exclude these events by subtracting the contribution of propagation to an image point $r_{2'} = (R_2, -z_2)$ mirrored to the outside of the sample:

$$\Phi_B(r_1, r_2) = \frac{1}{4\pi D_B} \left[\frac{1}{r_{12}} - \frac{1}{r_{12'}} \right]. \quad (132)$$

This half-space propagator behaves like R^{-3} at large R and thus permits to carry out the integration. The final result is some number I_L and gives the incoherent background on top of which we now study the interference contribution.

Each multiple-scattering diagram like (129) has an interference-correction counterpart such as



in which the conjugate amplitude travels along the same scatterers, but in opposite direction. The contribution of such maximally crossed diagrams to the back-scattered intensity can be accounted for along the same lines. First of all, incident and scattered amplitudes now pick up a phase between the surface and the scattering end points. Namely, the amplitude ψ picks up $\exp\{ik \cdot r_1\}$ at the entrance and $\exp\{ik' \cdot r_2\}$ at the exit of the medium. The path-reversed complex conjugate amplitude picks up $\exp\{-i[k \cdot r_2 + k' \cdot r_1]\}$. So after all, there is a total phase difference of $\Delta\varphi = (k + k') \cdot (r_1 - r_2)$. Exactly toward the backscattering direction, $k' = -k$, this phase difference vanishes. Close to backscattering, for a small angle $\theta \ll 1$, one has $|k + k'| \approx k_\perp = k \sin \theta \approx k\theta$, and the phases differ by $\Delta\varphi = kR\theta$.

Thus, each path acts like Young double-slit interferometer with the two end-point scatterers playing the role of the two slits. The larger the transverse distance R between the scatterers, the finer the interference fringes. The only point where all fringes are bright is the symmetry point $\theta = 0$ toward backscattering. Sufficiently far away from this direction, the sum of random fringe patterns averages out to zero. The sum of all interference term is again the integral over all end points with the appropriate weight furnished by the intensity propagator (132) (which must be modified if some additional dephasing processes are at work, see section 6.3 below). This simple calculation predicts a relative interference enhancement over the background

$$\frac{I_C(\theta)}{I_L} \approx \frac{1}{(1 + kl|\theta|)^2} \quad (134)$$

The interference-induced enhancement, shown in figure 19 as a dashed blue line, survives in an angular range $\Delta\theta = 1/kl = \lambda/(2\pi l)$ around backscattering. Very characteristically, this peak features a triangular cusp at backscattering (plotted

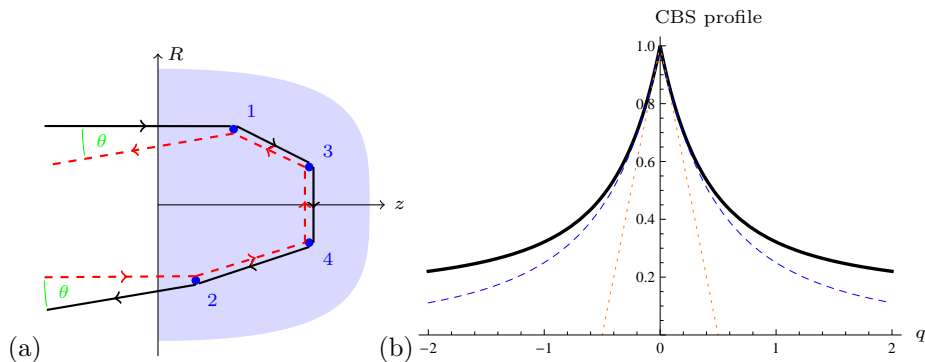


Figure 19: Coherent backscattering (CBS) (a) Schematic picture of a four-scatterer path; the constructive interference of path-reversed amplitudes in the backscattering direction $\theta = 0$ leads to an observable intensity enhancement. Away from backscattering, the phase differences average out and leave only the background intensity. (b) CBS profile as function of reduced scattering angle $q = kl\theta$, normalized to the value at $\theta = 0$. Solid black: exact solution (136). Dashed blue: Diffusive solution (134). Dotted orange: Linear solution (135) with characteristic slope discontinuity at backscattering.

in dotted orange),

$$\frac{I_C(\theta)}{I_L} = 1 - 2|q| + O(q^2) \quad (135)$$

where $q = kl\theta$ is the reduced momentum transfer.

The exact solution for scalar waves and isotropic point scatterers can be calculated solving the Milne equation of intensity transport. The CBS profile can then be expressed as the integral [63]

$$\frac{I_C(\theta)}{I_L} = \frac{1}{C} \exp \left\{ -\frac{2}{\pi} \int_0^{\pi/2} d\beta \ln \left[1 - \frac{\arctan \sqrt{q^2 + \tan^2 \beta}}{\sqrt{q^2 + \tan^2 \beta}} \right] \right\} \quad (136)$$

where $q = kl\theta$ and a constant $C = \exp \left\{ -\frac{2}{\pi} \int_0^{\pi/2} d\beta \ln [1 - \beta \cot \beta] \right\} \approx 8.455$ such that at the origin $I_C(0) = I_L$. This profile is plotted as a black curve in Fig. 19. It becomes apparent that the diffusive solution (134) gives a very good description for small scattering angles. Notably, its slope at $\theta = 0$ is precisely equal to the exact value that can be extracted from (136). This was to be expected since diffusion should be valid for long-distance bulk propagation, and long scattering paths have widely separated end points that contribute to the small transverse momenta making up the top of the CBS peak. Indeed, the diffusion prediction (134) is precisely recovered by replacing the exact propagation kernel under the logarithm by its diffusion approximation:

$$A(Q) = \arctan(Q)/Q \approx 1 - \frac{1}{3}Q^2 \quad (137)$$

valid at small $Q = \sqrt{q^2 + \tan^2 \beta}$.

The agreement between the diffusive profile (134) and the exact result (136) deteriorates at larger angle $q = kl\theta$. This discrepancy is due to low scattering orders that are not accurately captured by the diffusion approximation and the

imaging method used to mimic the exact boundary conditions. Indeed, only the very tip of the CBS peak stems from long paths reaching far into the bulk. The larger part of the total signal is due to contributions from rather short paths, for which scattering inside the surface skin layer is crucial.

One can calculate the contribution of scattering orders $n = 1, 2, \dots$ to the total incoherently back-scattered intensity, measured in units of the incident flux by the so-called bistatic coefficient $\gamma(\cos \theta', \cos \theta)$ [64] that depends on the angles θ' and θ of incidence and observation. For exact backscattering and normal incidence ($\theta = \theta' = 0$), one has $\gamma = \sum_{n \geq 1} \gamma_n$. The largest contribution comes from single scattering with $\gamma_1 = 1/2$ followed by double-scattering with $\gamma_2 = \ln(2)/2 \approx 0.35$ and so on, with an asymptotic decrease as $\gamma_n \sim n^{-3/2}$ [63].

When the CBS peak was first observed in the beginning of the 1980's [65, 66, 67], the diffusive theory used an image point placed at $z_{2'} = -(2z_0 + z_2)$ such that the diffuse propagator vanishes at a distance $z_0 = 2/3$ outside the sample. This translates to the boundary condition that the total incident diffusive flux on the surface vanishes [62, 68] and leads to a diffusive CBS peak shape of

$$\frac{I_C(q)}{I_L} = \frac{1}{(1 + |q|)^2} \frac{1}{1 + 2z_0} \left[1 + \frac{1 - \exp\{-2z_0|q|\}}{|q|} \right]. \quad (138)$$

This diffusive solution predicts a different slope at the origin, viz., $-2[1 + z_0^2/(1 + 2z_0)]$, which is off by more than 20% from the exact value, although one would expect the diffusion solution to get this value right [63]. This is all the more disturbing as fits to the diffuse CBS peak shape are generally used to measure the transport mean-free path. Also at larger angles this solution cannot convince because the diffusion profile decays as q^{-2} , whereas the exact solution decreases like $|q|^{-1}$. This asymptotic behavior is known to come from the double-scattering contribution.

Bart van Tiggelen has noticed [69] that the diffusion approximation becomes virtually exact if single- and double scattering are included separately since

$$\frac{1}{1 - A(q)} = 1 + A(q) + \frac{A(q)^2}{1 - A(q)} \approx 1 + A(q) + \frac{3\alpha}{q^2} \quad (139)$$

both for *small and large* q , with a numerical coefficient $\alpha = 1$ for $q \rightarrow 0$ and $\alpha = \pi^2/12 \approx 0.822$ for $q \rightarrow \infty$. Therefore, the best approximation to the exact solution is obtained by first taking the exact double-scattering profile [63, 70]

$$\gamma_2(q) = \frac{1}{\pi} \int_0^{\pi/2} d\beta A \left(\sqrt{q^2 + \tan^2 \beta} \right) = \frac{2 \cosh^{-1}(1/|q|) - \cosh^{-1}(1/q^2)}{2\sqrt{1 - q^2}} \quad (140)$$

where $\cosh^{-1}(x)$ is the inverse hyperbolic cosine function, then adding the diffusive solution

$$\gamma_{\text{diff}}(q) = \frac{3\alpha}{2(1 + |q|)^2} \left[1 + \frac{1 - \exp\{-2z_0|q|\}}{|q|} \right] \quad (141)$$

and finally fitting the extrapolation length z_0 and diffusion-constant multiplica-
tor α such that height and slope are equal to the exact values at the origin. Doing
this, we find $\alpha^* \approx 0.86$ within the expected interval $[0.822, 1]$ and $z_0^* \approx 0.81$.
Figure 20 shows the exact CBS profile (with the single-scattering contribution

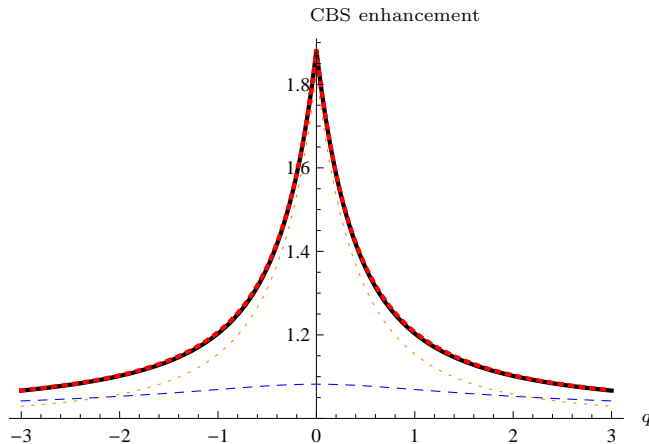


Figure 20: CBS intensity enhancement in units of the background intensity as function of reduced scattering angle $q = kl\theta$. Solid black: exact solution (136) minus the single-scattering value $\gamma_1 = 1/2$. Dashed blue: double scattering contribution (140). Dashed red: sum of double scattering and best diffusive solution, (141) with $\alpha^* \approx 0.86$ and $z_0^* \approx 0.81$. Dotted orange: Traditional diffusive CBS peak, eq. (141), with $\alpha = 1$ and $z_0 = 2/3$ shown for comparison. Even for this time-reversal invariant case, the backscattering enhancement is slightly smaller than 2 because of the single-scattering contribution to the background that is absent in the CBS signal.

subtracted as required) together with the double scattering contribution plus the full approximated diffusive CBS profile that turns out to be in excellent agreement, both for small and large angles.

The full width at half height of the CBS profile is $\Delta q \approx 0.73kl \approx 4.59l/\lambda$, and observing the CBS peak can be used to measure the transport-mean free path quite accurately. The explicit occurrence of the wavelength λ emphasizes that CBS is a genuine interference effect. In many circumstances, the mean-free path is much longer than the wavelength, such that $kl \sim 10^2 \dots 10^3$, and $\Delta\theta$ is at most a couple of mrad. This makes CBS difficult to observe with the naked eye, together with the constraint that one has to look exactly toward the backscattering direction, but it can be easily imaged using standard optics, as schematically shown in Fig. 21.

6.2 Live experiment

Because the CBS cone is typically very narrow and its maximum height at best equal to the average background, a source with large angular dispersion will broaden the signal too much and reduce enhanced backscattering. Thus, it is highly desirable to use a quasi-parallel beam obtained from a laser source, with angular divergence smaller than a fraction of mrad. This in turn requires a large spot, with a diameter larger than the mean free path, which is easily obtained by expanding the output beam of a commercial diode laser with a telescope. The scattering medium should scatter efficiently and must not absorb the light: a bright white object is thus chosen. A piece of ordinary paper turns out to give the best results. A sheet of paper is about $100 \mu\text{m}$ thick and obviously

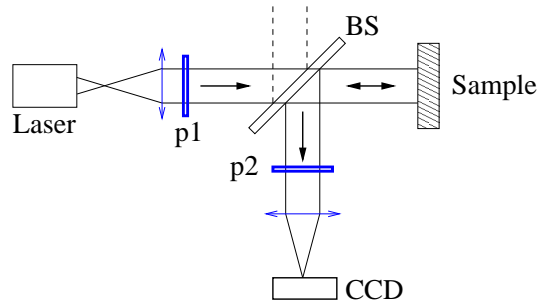


Figure 21: Schematic view of a table-top CBS experiment. Light from a wide laser beam with small angular dispersion is directed onto a disordered sample. The diffuse retro-reflected intensity is sent by a beam-splitter (BS) in the focal plane of a lens and recorded by a CCD camera, thus imaging the angular distribution. Polarization elements (p1 and p2) select a suitable polarization channel; generally, the helicity-preserving channel of opposite circular polarization is recommended.

scatters most of the incoming beam, meaning that the mean free path does not exceed a few tens of μm . A piece of teflon could also be used, but the mean free path is significantly larger, meaning a narrower CBS cone, much harder to detect. White paint or milk make also good samples, with the advantage that the concentration and thus the mean free path can be varied and that the thermal motion of scatterers inside the solvent provides us with configuration averaging for free; however, these samples must be put inside some transparent container whose surface can produce specular reflection that is easily confounded with the CBS signal.

A semitransparent plate (beamsplitter) can be used to send the back-reflected light into a 1280×1024 pixel CCD camera with pixel size around $5 \mu\text{m}$, located about 20 cm from the scattering medium, thus ensuring a 0.025 mrad angular resolution. Fig. 22 (left) shows the image recorded from a fixed piece of paper. This situation corresponds to a single realization of the disorder. The electric field on each pixel is the coherent sum of the field amplitudes radiated by each point of the sheet of paper. Because of its disordered nature, each contribution picks a random amplitude and phase, resulting in a characteristic speckle pattern on the CCD camera, the “optical fingerprint” of the paper. The angular size of the speckle grain is of the order of $1/kL$ where L is the size of the illuminated spot on the sheet of paper. For our case, it is about 0.1 mrad , i.e. slightly larger than the pixel size, in agreement with the experimental observation. The attentive reader may notice that the bright spots look slightly brighter in a roughly circular area on the right side of the figure. In order to see the CBS cone, one should perform configuration averaging. This is easily done by mounting the piece of paper on a rotating device (in our case a battery-powered computer fan). On the time-averaged intensity, shown in Fig. 22 (right), the fluctuating speckle pattern has been washed out, leaving a uniform background, on top of which appears a smooth bright spot of approximate width 10 mrad due to coherent backscattering. The effect is perhaps not dramatic, as the enhancement factor cannot be larger than 2 (it is 1.6 in this live experiment), but clearly present and visible with the naked eye.

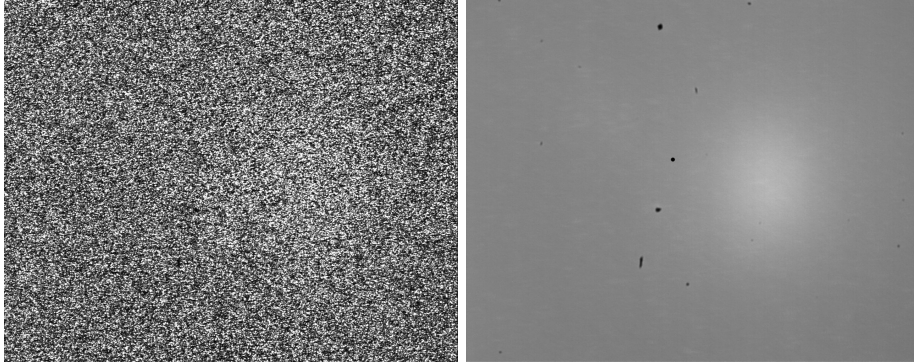


Figure 22: Intensity around the back-scattered direction for a piece of paper exposed to a parallel laser beam. For a fixed paper (left figure), one observes a characteristic speckle pattern, due to random interference of phase-coherent light scattered by a single configuration of disorder. By averaging over various parts of the paper, small-scale random variations are averaged out, but an enhanced intensity is clearly visible around exact backscattering. Original data from an experiment performed during the Les Houches Summer School in Singapore on July, 15th, 2009. Special thanks to David Wilkowski, Kyle Arnold, and Lu Yin from the Center for Quantum Technologies, National University of Singapore, for generous support and invaluable help in setting up the experiment.

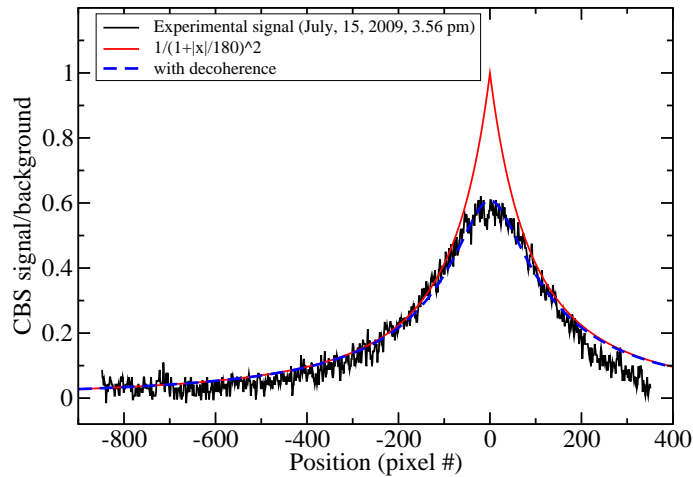


Figure 23: Experimentally measured coherent backscattering signal, together with a fit to the simplest theoretical formula, (134) (full red line), and to (146) with phenomenological decoherence included (dashed blue). From the angular width of the CBS signal, one can extract the transport mean free path inside the sheet of paper, here $25 \mu\text{m}$. Experimental imperfections limit the coherence of the phenomenon and are responsible for the deviation from the peaked shape at the center of the cone. When properly taken into account (dashed curve), the agreement is very good.

A cut across the spot center is presented in Fig. 23 together with a fit to the simplest theoretical formula, eq. (134). The fit is quite good in the wings and allows us to extract the mean free path inside the piece of paper, in our case $25\ \mu\text{m}$. The fact that the top of the CBS peak is rounded can be attributed to various experimental imperfections such as the finite angular resolution, geometrical aberrations, finite thickness and residual absorption of the piece of paper, but could in principle also highlight the presence of a decoherence mechanism.

6.3 Dephasing/decoherence

The CBS phenomenon presented so far relies on perfect phase coherence of the multiply scattered wave. What happens if some external agent—such as some degree of freedom inside the paper coupled to the wave—affects the scattered amplitude in an uncontrolled way? Qualitatively, it is clear that amplitudes of long scattering paths are more fragile than those of shorter paths. As very long paths are responsible for the characteristic triangular shape of the CBS cone around the exact backscattering direction, it is important to understand the effect of decoherence on the CBS signal. In return, the CBS enhancement factor can serve as a sensitive measure for phase coherence.

There is no universal way of breaking phase coherence, and the effect on CBS can be different depending on the specific mechanism at work. Nevertheless, a simple phenomenological approximation may often be used, and we will see below that several physical processes are well described by this approximation. This assumption is that phase coherence is lost at a constant rate, characterized by a phase-coherence time τ_ϕ , also called dephasing time. Then, interference terms associated with paths who are visited in a time t have to be multiplied by a factor $\exp(-t/\tau_\phi)$. An example of such a situation is provided by a Michelson interferometer operated with a classical light source, where the interference disappears once the optical path length difference exceeds $c\tau_\phi$, with τ_ϕ the longitudinal coherence time of the source. Note that these phenomena are typically called “dephasing” in the context of classical waves, and “decoherence” for quantum mechanical matter waves. The bottom line is simply that interference is lost by coupling to some external degree of freedom.

The exponential attenuation of interference as $\exp(-t/\tau_\phi)$ applies especially often to the Cooperon contribution. In Fourier space, the effect is simply tantamount to the replacement

$$\omega \mapsto \omega + \frac{i}{\tau_\phi} \quad (142)$$

or, in the diffusive propagator (112):

$$\frac{1}{-i\omega + D_B q^2} \mapsto \frac{1}{-i\omega + \frac{1}{\tau_\phi} + D_B q^2} = \frac{1}{-i\omega + D_B \left(q^2 + \frac{1}{D_B \tau_\phi} \right)} \quad (143)$$

which can be also be obtained via the replacement

$$q^2 \mapsto q^2 + \frac{1}{L_\phi^2}. \quad (144)$$

The phase coherence length,

$$L_\phi = \sqrt{D_B \tau_\phi}, \quad (145)$$

is the average distance over which the wave propagates *diffusively* before losing its phase coherence.

This simple replacement can be used to calculate the shape of the CBS cone in the presence of decoherence effects. Indeed, Sec 6.1 discusses several approximate expressions for the shape, all expressed as a function of the transverse momentum $k_{\perp} \approx k|\theta|$, which is nothing but the sum of the incoming and outgoing momenta (in the limit of small angles $\theta \ll 1$). The substitution $k_{\perp}^2 \mapsto k_{\perp}^2 + 1/D_B\tau_{\phi}$ in eq. (134) yields

$$\frac{I_C(\theta)}{I_L} \approx \frac{1}{\left[1 + \sqrt{(kl\theta)^2 + l^2/L_{\phi}^2}\right]^2}. \quad (146)$$

This expression is now a smooth function of θ (no cusp at $\theta = 0$ anymore). In the limiting case $l \ll L_{\phi}$, one recovers the previous expression, only slightly perturbed near the tip. In the opposite limit $L_{\phi} \ll l$, the CBS cone disappears completely, which is quite natural as interference effects are washed out before the wave travels a single mean free path. The relative height of the CBS peak, compared to the background at $kl|\theta| \gg 1$, is

$$\frac{I_C(0)}{I_L} = \frac{1}{[1 + l/L_{\phi}]^2} \approx 1 - 2\frac{l}{L_{\phi}} = 1 - 2\sqrt{\frac{\tau_l}{\tau_{\phi}}} \quad (147)$$

where the last two expressions are valid in the limit of weak decoherence $l \ll L_{\phi}$. Here, $\tau_l = \sqrt{D_B/l^2}$ is the mean free time separating two consecutive scattering events. This expression emphasizes the sensitivity of the CBS cone to dephasing effects. Indeed, if the dephasing time is say 10 times larger than the mean free time, its effect on the CBS cone is still very noticeable, reducing its height by almost 50%. For example, the experimentally observed CBS cone in the live experiments is well fitted by eq. (146), with a decoherence time $\tau_{\phi} = 12.5\tau_l$.

Several other types of decoherence have been studied in great detail in connection with light and cold atoms. In the following, we present a few of them qualitatively, referring to the literature for more details.

6.3.1 Polarization

For simplicity, we have up to now considered a scalar complex wave, describing e.g. a spinless atomic matter wave. Many real atoms, all electrons and also electromagnetic waves are more complicated because of their spin/polarization. Especially light scattering does not preserve polarization, as is obvious from the requirement of transversality. Thus the light back-scattered along the direct and reverse paths generically emerges from the medium with different polarization. But orthogonal polarizations do not interfere, and thus one may expect a reduced enhancement factor.

Technically, one has to dress the multiple-scattering Cooperon contribution with the polarization structure. Two independent polarizations of the propagating intensity must be taken into account (one in the retarded, one in the advanced Green function), leading to a tensorial structure for diffuson and Cooperon alike. The complete calculation of this effect is possible by decomposing the intensity kernel into irreducible tensor moments [72]. To make a long story short, it is enough to say that each contribution has a kernel of the

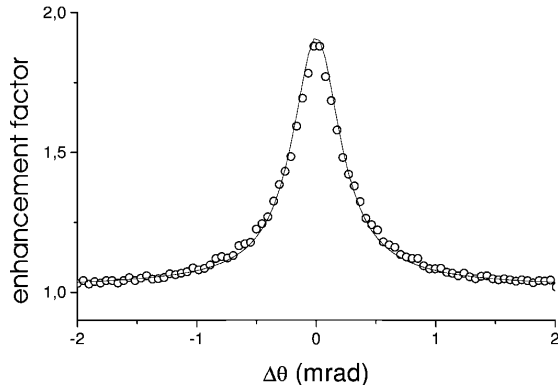


Figure 24: CBS of light by cold Strontium atoms [71]. The backscattering enhancement is close to 2, which indicates full phase coherence. Signal observed in the helicity preserving channel (incoming light circularly polarized, detection in the opposite circular polarization). Solid line: the result of a calculation taking into account the finite geometry and inhomogeneous density of the atomic cloud.

type (143), with its own τ_ϕ of the order of τ_l . The physical interpretation is clear: because scattering will on average lead to depolarization, all channels associated with specific polarization correlations must decay during propagation. Only the one channel measuring the total intensity is protected by conservation of energy, with $1/\tau_\phi = 0$, and propagates diffusively.

If the system is additionally time-reversal invariant, the same conserved intensity channel also exists for the Cooperon. The population of the various contributions depends on the specific choices for the incoming and outgoing polarizations used for recording the CBS signal. Using the same linear polarization for excitation and analysis populates the conserved mode and ensures an optimal interference contrast for long scattering paths, at least for classical point-like objects (such as dye molecules) acting as Rayleigh scatterers (we will discuss in Sec. 6.3.4 the more general case). The same is true if the incident field has circular polarization and the opposite circular polarization is used for detection (helicity-preserving channel), with the additional advantage that the single scattering background of the diffuson is filtered out, allowing in principle the observation of a perfect CBS enhancement by a factor of 2 [73, 71].

6.3.2 Residual velocity of the scatterers

The previous derivation assumed quenched disorder, i.e. scatterers at fixed positions. Moving scatterers are a cause of decoherence: as light travels along two reciprocal paths, it visits the same scatterers, but in opposite order, i.e. at different times. If, during the time delay separating the scattering events on the direct and reversed path, the atom has moved by at least one wavelength, the phase coherence between the two paths will be lost. This phenomenon can alternatively be interpreted in the frequency domain, where moving scatterers induce a Doppler shift of the scattered photon which is different along the direct and reversed path. Although this phenomenon does not lead to a strict exponential decay of the phase coherence [74], it reduces the enhancement factor,

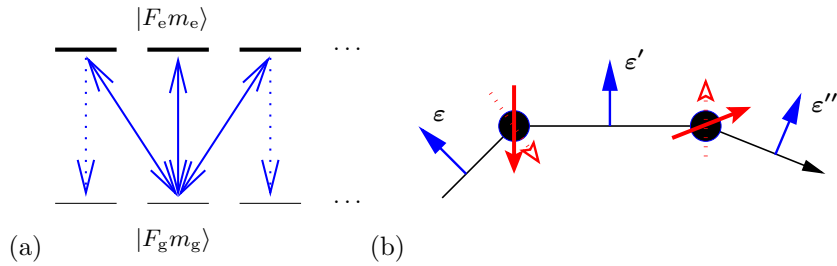


Figure 25: (a) Light scattering by a degenerate atomic dipole transition $F_g \leftrightarrow F_e$ can either preserve spin (Rayleigh transition, full arrows) or change the spin (degenerate Raman transition, dotted arrows). (b) Multiple light scattering by randomly placed atoms with internal spin states involves depolarization/decoherence from both spin-orbit (transversality) and spin-flip effects.

which has been notably observed with cold atoms [75].

In general, interference of waves is suppressed once the environment has acquired knowledge of the path taken by the scattered object. This can be most simply seen in experiments of the Young's double-slit type [76], but applies equally to the CBS by light from moving atoms, where moreover the storage of which-path information in the atomic recoil has been studied [77].

6.3.3 Non-linear atom-light interaction

Because atoms have extremely narrow resonance lines, they have large polarisabilities and already quite low laser intensities can saturate an atomic transition, in which case the atom scatters photons inelastically. It is easy to understand that such a non-linear inelastic process will reduce the phase coherence of the scattered light and the enhancement factor. This indeed has been observed [78]. A full quantitative understanding of multiple inelastic scattering is still not available. For a model system of two atoms driven by a powerful laser field, a rather complete understanding of the CBS signal has been achieved (see [79, 80] and references therein).

In the context of matter waves, one may study coherent backscattering of interacting matter waves, obeying a non-linear equation such as the Gross-Pitaevskii equation, evolving in a random optical potential. It has been shown that already a moderate non-linearity induces a phase-shift between the direct and reversed paths and thus a decrease of the height of the CBS peak, and may in some cases even create a negative contribution in the backward direction [53]. These theoretical predictions still await experimental realization.

6.3.4 Internal atomic structure/spin-flip

The preceding description treats atoms as Rayleigh point scatterers that radiate a purely dipolar electromagnetic field, with an induced dipole directly proportional to the incoming electric field. This is an excellent approximation for atoms with a non-degenerate electronic ground state, such as Strontium. The situation is radically different if the atomic ground state is degenerate: indeed, when scattering a photon, the atom may stay in the same atomic state (Rayleigh

transition) or change to another state with the same energy (degenerate Raman transition), see Fig. 25(a).

The basic rules of quantum mechanics imply that orthogonal final state cannot interfere. In other words, two multiple scattered paths will interfere only if they are associated with *the same initial and final states of all atoms*.⁸ Note that there is no need for the initial and final states to be identical, so that Raman transitions can very well contribute to interference terms, if and only if the same Raman transitions occur along the interfering paths.⁹ A commonly encountered situation is that the degeneracy of the atomic ground state is due to its non-zero total angular momentum, see Fig. 25(a): Raman transitions then involve different Zeeman sub-states. The detailed calculation of the scattering vertex requires to incorporate also the angular momentum, i.e. the polarization, of the light. Then, the whole structure of the diffuson and the Cooperon boils down to various kernels of type (143), where the various depolarization/decoherence rates are rotational invariants that depend only on the angular momenta F_g, F_e [70, 83].

For a typical alkali atom like ^{85}Rb with a $F_g = 3 \rightarrow F_e = 4$ resonance line, the longest decoherence time for the Cooperon is $\tau_\phi = \frac{19}{21}\tau_l$ [72], meaning that the CBS interference is quite efficiently killed already by very few scattering events. An immediate consequence is that the CBS cone observed on a cold Rb gas has a much reduced enhancement factor [85]. A less trivial feature is that the best Rb CBS signal is not observed in the same channels than with Sr. Detailed calculations can be performed and an excellent agreement between the measured and the calculated CBS signals is observed [84], see Fig. 26.

The internal atomic degrees of freedom are here responsible for the loss of coherence. Information flows from the light to the atoms; as long as we do not precisely measure the internal state of each atom, this information is lost and the interference contrast is reduced. This information-theoretic argument can be made quantitative by investigating how much which-path information is stored within the atomic internal degrees of freedom. A quantitative measure of this wave-particle-duality, developed originally in the context of Mach-Zehnder-type interferometers [86], can be investigated analytically in the simplest cases and highlights the rôle of which-path information in the loss of CBS interference visibility [87].

A simple way to restore phase coherence is to lift the atomic degeneracy by applying an external magnetic field. Fields as small as a few Gauss are enough to detune some of the atomic transitions far from resonance, thus reducing the effect of Raman transitions. It has been experimentally observed and theoretically explained how this can increase the enhancement factor [88]. We here face a seemingly paradoxical situation (in view of the negative magneto-resistance discussed in Sec. 7), where adding an external magnetic field, which should break the time-reversal symmetry, has the effect of increasing the interference between time-reversed paths! Similarly, strong magnetic fields in electronic samples have been used to align free magnetic impurities, reduced thus spin-flip effects and

⁸Not taking this into account may lead to incorrect results, see for example [81], corrected in [82].

⁹Thus, one must take statements like “Raman scattered light is incoherent”, often made by quantum opticians, with great care. It is true that Raman scattered light does not interfere with the incoming reference beam—because the final states of the atom are different—but a single Raman-scattered photon along two different paths does very well interfere with itself.

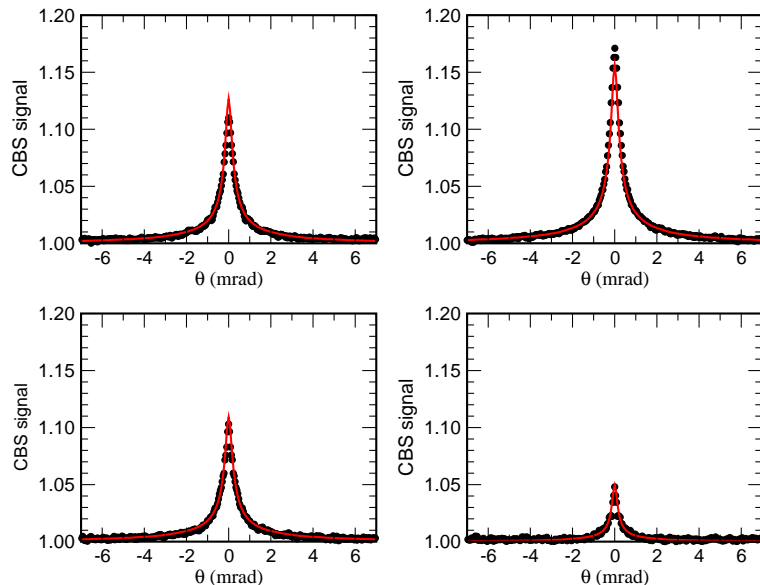


Figure 26: CBS by a cloud of cold Rubidium atoms, in four polarization channels (upper/lower left: parallel/perpendicular linear polarization; upper/lower right: circular polarization with non-preserving/preserving helicity). Solid red line: calculation taking into account the geometry of the atomic cloud. [84]. The enhancement factor is strongly reduced compared to ideal Rayleigh scatterers such as Strontium, Fig. 24. This is due to the internal Zeeman structure of the Rubidium atom, Fig. 25a). Note in particular that the helicity preserving channel—where the largest enhancement is found for point scatterers such as Strontium—gives here the smallest enhancement.

restore Aharonov-Bohm interference [89, 90].

7 Weak localization (WL)

As discussed in the preceding section, the Cooperon is responsible for enhanced backscattering, which implies an increased probability to return to the starting point. In the bulk of a disordered system, diffusive transport is thus hindered. This phenomenon, known as weak localization, is quantitatively expressed by a reduction of the diffusion constant (or dimensionless conductance/conductivity) with respect to the classical diffusion constant expected for phase-incoherent transport.

The weak-localization effect of the Cooperon is expressed by eq. (128). For the sake of concreteness, we will take in the following quantitative estimates the example of atomic matter waves with a quadratic dispersion relation $\varepsilon = \hbar^2 k^2 / 2m$. The free density of states (103) is

$$N_0(\varepsilon) = \frac{S_d}{(2\pi)^d} \frac{mk^{d-2}}{\hbar^2} \quad (148)$$

where $S_d = 2\pi^{d/2}/\Gamma(d/2)$ is the area of the unit sphere in dimension d : $S_1 = 2$, $S_2 = 2\pi$, $S_3 = 4\pi$. The Boltzmann diffusion constant $D_B = \hbar k l / dm$ is

directly proportional to the transport mean free path l . Because the Cooperon is isotropic, the d -dimensional integral in (128) can be reduced to a trivial $(d-1)$ -dimensional angular integral and a radial integral over momentum q , such that

$$\frac{1}{D} = \frac{1}{D_B} \left(1 + \frac{\hbar}{\pi m k^{d-2} D_B} \int_0^\infty \frac{q^{d-1} dq}{q^2 - i0} \right). \quad (149)$$

The result of the q -integral depends crucially on the dimensionality of the system. This is a consequence of the fact, well known from classical random walks, that the return probability to the origin is the higher, the lower the spatial dimension d . Therefore, weak—and consequently also strong—localization are immediately seen to have the largest impact in low dimensional systems.

7.1 $d = 1$

In dimension $d = 1$, the integral (149) diverges for small q . However, for a system of size L , the momentum q cannot take arbitrary small values, and a lower cutoff of the order of $1/L$ must be used. A simple way of implementing it—following the recipe of Sec. 6.3 for including decoherence effects—consists in replacing q^2 by $q^2 + 1/L^2$. One then gets:

$$\frac{1}{D} = \frac{1}{D_B} \left(1 + \frac{L}{2l} \right). \quad (150)$$

This expression is valid only if the weak localization contribution is a small correction, i.e. for $L \ll l$. To lowest order, we recover $D \approx D_B(1 - L/2l)$, which is the exact result (49) already derived for 1d systems in Sec. 3.3. The interest of the present approach is that a full microscopic theory provides us with the weak localization correction and thus puts the scaling theory of localization on firm grounds.

7.2 $d = 2$

In dimension 2, the integral diverges both for small and large q . A suitable cutoff at small q is again $1/L$, the inverse of the system size. Diffusive transport is a long time, large distance behavior. It is not expected to give an accurate description on a scale shorter than the mean free path. Performing the integral with a natural cutoff $1/l$ at large q thus leads to

$$D \approx D_B \left[1 - \frac{2}{\pi k l} \ln \left(\frac{L}{l} \right) \right]. \quad (151)$$

In terms of the dimensionless conductance $g = 2mD/\hbar$, this implies the following scaling relation:

$$\beta(g) = \frac{d \ln g}{d \ln L} = -\frac{2}{\pi g}. \quad (152)$$

Our microscopic calculation thus gives an explicit prediction that can be readily incorporated into scaling theory, as anticipated in Sec. 3.6.

How can weak localization be observed experimentally? A priori, any measured diffusion constant incorporates already all interference corrections to the

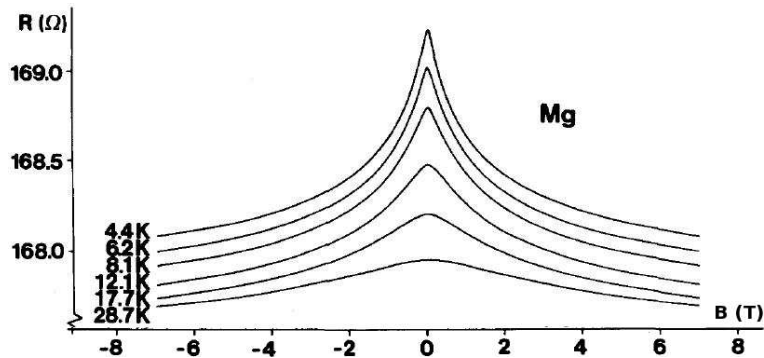


Figure 27: Experimentally measured resistance of a thin Mg film exposed to a perpendicular magnetic field. The magnetic field breaks the constructive interference of waves counter-propagation along closed loops, reduces the weak localization effect, and thus results in *negative magneto-resistance*. Similarly, larger temperatures reduce the phase coherence of the electronic wavefunction, and also reduce weak localization corrections. Adapted from [91] (courtesy of G. Bergmann).

classically expected value. Fortunately, the Cooperon contribution to weak localization is due to the constructive interference between a multiply scattered path and its time-reversal. If one breaks time-reversal symmetry on purpose, then the delicate interference is likely to disappear, and an enhancement of diffusive transport should be observed.

For charged particles—such as electrons in solid state samples—the simplest way is to add a magnetic field perpendicular to the sample. In the presence of a vector potential \vec{A} , a charged particle picks an additional phase $\int e\vec{A}\cdot d\vec{l}/\hbar$ along a closed loop. This is nothing but e/\hbar times the enclosed magnetic flux. Along each closed loop, this additional phase appears in the Cooperon contribution. If this phase fluctuates largely from one loop to the other, the resulting interferential contribution will vanish. As the smallest area enclosed by a diffusive loop is l^2 , the weak localization correction is expected to vanish above $B \approx \hbar/el^2$. For a typical mean free path of a fraction of μm , this is in the Tesla range. Figure 27 shows the measured resistance of a 2D Mg film vs. magnetic field at various temperatures [91]. At the lowest temperature, propagation is almost fully phase coherent and one observes a decreasing resistance, i.e. a increasing conductance, when a magnetic field is applied. This *negative magneto-resistance* was a mystery when first observed and only later explained as a manifestation of weak localization. When temperature increases, the phase coherence of the electrons diminishes, and the weak localization correction gets smaller. This is, in a different context, analogous to decoherence phenomena discussed for coherent backscattering in Sec. 6.3. Note that, from such experimental data, it is possible to measure the transport mean free path (via the width of the weak localization peak) as well as the temperature-dependence of the decoherence time. In recent times, weak localization measurements have been used as very sensitive detectors for minute concentrations of magnetic impurities, which induce spin-flip decoherence and are responsible for finite decoherence times even at zero temperature [92, 90, 93].

7.3 $d = 3$

In dimension 3, the integral in eqn (149) requires only a cutoff at large q , which we take again as $1/l$ and obtain

$$D \approx D_B \left(1 - \frac{3}{\pi(kl)^2} \right). \quad (153)$$

This diffusive Cooperon contribution to weak localization is found to scale as $1/(kl)^2$. However, this is not the whole story, because other diagrams, not included in the simple diffusive Cooperon, give contributions that are actually more important for small disorder $kl \gg 1$. Just as for the CBS cone discussed in Sec. 6.1, also here the double-scattering diagrams appearing in eqn (117) contribute to leading order $1/kl$. In $d = 3$, the *static* electronic conductivity was found to be given by [36]

$$\frac{\sigma(\omega = 0)}{\dot{\sigma}} = 1 - \frac{2\pi}{3kl} - \frac{\pi^2 - 4}{(kl)^2} \ln(kl) + O((kl)^{-2}). \quad (154)$$

As long as $kl \gg 1$, the weak localization is only a small correction, again providing us with a macroscopic ground for the scaling theory of localization. It also gives an approximate criterion for the onset of Anderson localization, which should set in approximately when the right hand sides of eqns (153) or (154) vanish, i.e. $(kl)_c = O(1)$. This is Ioffe-Regel criterion, eq. (57). However, the precise calculation of the critical point is a delicate endeavor. What precisely happens at the $1/l$ scale is not universal. The same is true for the Ioffe-Regel criterion, but the latter nonetheless yields a first estimate on where to expect the Anderson transition.

7.4 Self-consistent theory of localization

Weak localization describes how diffusive transport is affected by interference. In essence, however, weak localization is a perturbative result: first, because the Cooperon contribution is evaluated using a diffusive kernel valid in the absence of interference; second, because this simple approach takes into account only a specific type of diagrams. The first assumption is especially questionable in 1d, where diffusive transport actually never occurs, because localization appears at the very same scale (the localization length) than diffusion (the mean free path). Concerning the second point, the dominant rôle of the Cooperon in large systems was recognized already by Gorkov et al. [94] and Abrahams et al. [19]. However, a weak-disorder perturbation theory in powers of $1/kl$ alone would never be able to describe the Anderson transition (in 3d) for strong disorder, nor the crossover from weak to strong localization in 1d and 2d systems.

The self-consistent theory of localization, developed by Vollhardt and Wölfle in the 1980s [95, 96, 97], is an attempt to escape this seemingly hopeless situation by applying a suitable self-consistency scheme, as often employed with success to describe phase transitions in statistical physics. Rather than a theory with rigorously controlled approximations, it must thought of as a guess, albeit highly educated, about the most important contributions of diagrams to all orders. The basic observation is that the diffusive contribution of large closed loops in eq. (149) must itself be modified by weak localization: inside a large loop,

the wave explores smaller loops, leading to a decreased diffusion constant for propagation along the large loop. This argument can of course be repeated: one should take into account loops within loops within loops..., all the way down to the smallest loops, stopping at the scale of the transport mean free path.

The whole description must now be self-consistent, describing what happens at every scale from the mean free path up to the size of the system—or toward infinity in the bulk. The simplest idea would be to replace the static Boltzmann diffusion constant D_B in the integral of (149) by the renormalized diffusion constant D itself, thus providing us with an implicit equation for D . It turns out that this is not enough: indeed, a single number—the static diffusion constant D —cannot describe the full dynamics both for short times, where it is diffusive, and for long times where localization may eventually set in. So we require a scale-dependent diffusion constant, and it turns out that it is simpler to consider various time scales rather than various spatial scales. We thus consider a diffusion constant $D(\omega)$ which depends on frequency ω . The self-consistent expression for $D(\omega)$ just derives from (149) by re-introducing the ω dependence and replacing D_B by $D(\omega)$ in the integral:

$$D(\omega) + \frac{\hbar}{\pi m k^{d-2}} \int \frac{q^{d-1} dq}{q^2 - (i\omega/D(\omega))} = D_B. \quad (155)$$

In the short-time limit $\omega \rightarrow \infty$, the contribution of the integral vanishes and one gets back to classical Boltzmann diffusive propagation, as expected. The most interesting part takes place at long times, i.e. in the limit $\omega \rightarrow 0$, whose consequences again depend crucially on the dimension.

7.4.1 $d = 1$

At finite ω , the integral in (155) does not need any regularization, it is simply $\frac{\pi}{2} \sqrt{D(\omega)/(-i\omega)}$, and the implicit equation for $D(\omega)$ is easily solved [98]:

$$\frac{D(\omega)}{D_B} = \frac{\sqrt{1 - 16i\omega\tau_l} - 1}{\sqrt{1 - 16i\omega\tau_l} + 1} \quad (156)$$

where $\tau_l = l^2/D_B$ is the mean free time between two scattering events. This function is plotted in the left panel of Fig. 28 as function of $-i\omega$.¹⁰ In the limit of small ω , it behaves linearly $D/D_B \approx -4i\omega\tau_l$. This in turns implies that the propagation kernel $1/(-i\omega + D(\omega)q^2)$ is just $1/(-i\omega) \times 1/(1 + 4l^2q^2)$. When going back from momentum to configuration space by inverse Fourier transform, it implies that the intensity kernel is proportional to $\exp(-|z|/2l)$ at long times. It successfully describes exponential localization with the localization length $\xi_{\text{loc}} = 2l$, i.e. the exact result for the localization length! The elementary ingredients used for obtaining this important result are: quantum kinetic theory, microscopic calculation of the weak localization correction in the perturbative regime and its self-consistent extension. That the exact result is eventually obtained is a strong hint that the self-consistent approach catches an important part of the physics of localization.

¹⁰Imaginary frequency is only used for convenience, as it makes the diffusion constant purely real and thus easier to plot. The most important transport property is the small- $|\omega|$ behavior, which is linear in the localized regime, both for real or imaginary ω .

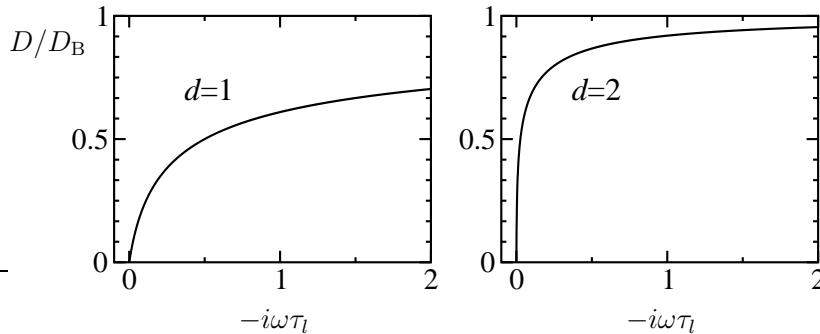


Figure 28: Diffusion constant vs. (imaginary) frequency, in units of Boltzmann diffusion constant and mean free time, respectively, as predicted by the self-consistent theory of localization, in 1d (left) and 2d (right, for $kl=1.5$). At large ω (short time), one recovers the classical Boltzmann diffusive behavior. At small ω , the dependence is linear, which implies exponential localization in configuration space, in agreement with scaling theory, numerical and experimental observations (in 1d). In 2d, the localized regime is reached at much smaller frequency because the localization length and time are exponentially large.

But beware! This triumph is somewhat tarnished by the fact that it is the *typical* intensity that decays with ξ_{loc} , whereas the *average* intensity calculated here should asymptotically decay with $4\xi_{\text{loc}}$, as shown in Sec. 2.5. The precise source for this discrepancy escapes our present understanding. Clearly, the self-consistent theory is built for the average intensity kernel $\langle G^R G^A \rangle$ and thus cannot describe the huge fluctuations in the localized regime. One lacks a diagrammatic expansion for the typical transmission, which would require to calculate contributions of advanced and retarded Green functions to all orders.

Decoherence effects can be easily included in the self-consistent approach by the replacement $-i\omega \mapsto -i\omega + 1/\tau_\phi$ explained in Sec. 6.3. In Figure 28, this replacement simply translates the curve horizontally to the left. One immediately finds that the diffusion constant no longer vanishes at $\omega = 0$, but takes a finite value, implying diffusive motion at long times. In the limit of weak decoherence $\tau_l \ll \tau_\phi$, the residual diffusion constant is $D \approx 4\tau_l D_B / \tau_\phi = \xi_{\text{loc}}^2 / \tau_\phi$. It is much smaller than the Boltzmann diffusion constant and allows for a simple physical interpretation: a phase-breaking event, occurring on average every τ_ϕ , destroys the delicate interference responsible for localization. This implies a restart of diffusion during time τ_l after which localization sets in again, until the next phase breaking event, etc.

7.4.2 $d = 2$

In 2d, the integral in (155) diverges in the large- q limit, requiring a regularization. The natural short-distance cut-off is the mean free path l . Elementary manipulations shows that $D(\omega)$ is implicitly determined by

$$\frac{D(\omega)}{D_B} = 1 - \frac{1}{\pi kl} \ln \left(1 - \frac{D(\omega)}{D_B} \frac{1}{2i\omega\tau_l} \right). \quad (157)$$

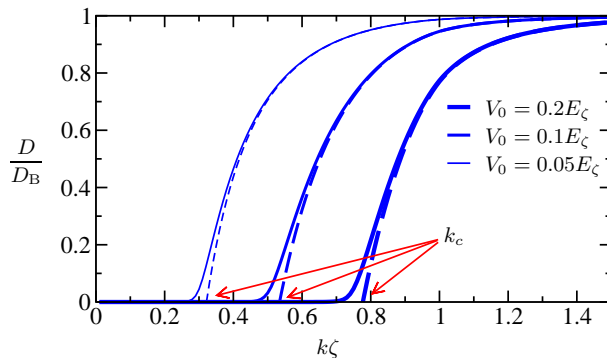


Figure 29: Diffusion constant (normalized to the Boltzmann diffusion constant) computed from the self-consistent theory of localization, for atomic matter waves with wave vector k exposed to a 2d speckle potential with correlation length ζ and different amplitudes V_0 . A stronger potential means a smaller value of kl . Dashed lines are the prediction of the simple perturbative weak localization correction, eqn (151), solid lines the result of the self consistent approach, eqn (157), including residual decoherence due to spontaneous emission implemented via eqn (142). A rather sharp cross-over between the Boltzmann diffusive behavior at high energy and the quasi-localized behavior at low energy is observed around a critical value k_c [99].

In contrast with the 1d case, D/D_B is not a universal function, it depends on the parameter kl . The right panel of Fig. 28 plots it for $kl = 1.5$. It displays the classical diffusive behavior $D \approx D_B$ at large ω (short times), and localization at long times. Indeed, for $\omega \rightarrow 0$, one finds $D(\omega) \approx -i\omega\xi_{\text{loc}}^2$, i.e. exponential localization with the localization length

$$\xi_{\text{loc}} = l\sqrt{\exp(\pi kl) - 1} \approx l \exp\left(\frac{\pi kl}{2}\right). \quad (158)$$

This provides us with a microscopic derivation of the result of scaling theory, eq. (56). The self-consistent approach describes correctly the exponentially large localization length in 2d.¹¹ Note that, even for strong disorder with a rather small value $kl = 1.5$, the linear regime in Fig. 28 is observed only at very small ω , i.e. for very long times.

Decoherence can be taken into account exactly like in 1d. Instead of a true metal-insulator transition, one observes a cross-over from classical diffusion at large kl towards a residual diffusion (triggered by decoherence) at small kl . Explicit calculations have been carried out in [99] for the case of atomic matter waves in a speckle potential, where residual spontaneous emission is one source of decoherence that can be experimentally tuned. Figure 29 shows typical results. Because of the exponential dependence in 2d, the cross-over from quasi-localized behavior at small k to diffusive behavior at large k is rather rapid. In any case, a crucial requirement is to have very cold atoms, with de Broglie wavelength shorter than the speckle correlation length.

Considering an expanding BEC wave packet released from a harmonic trap, one can calculate the expected stationary (for negligible decoherence) density

¹¹The same caveats than in 1d exist, concerning average versus typical quantities.

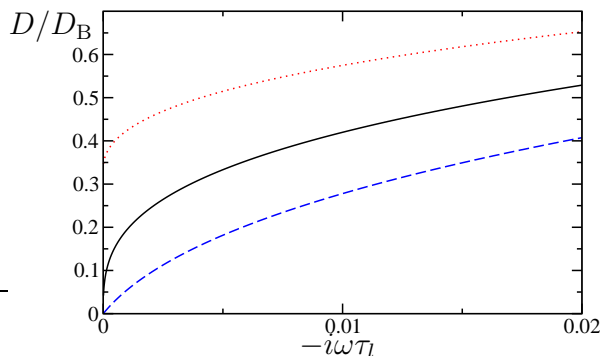


Figure 30: Diffusion constant vs. (imaginary) frequency, in units of Boltzmann diffusion constant and mean free time, respectively, computed from the self-consistent theory of localization in 3d, eqn (159). Dotted red line: metallic regime $kl = 1.2$ with finite diffusion constant at long times. Dashed blue line: insulating regime $kl = 0.8$ with a finite localization length. Solid black line: critical point $kl = (kl)_c = \sqrt{3/\pi}$ of the metal-insulator Anderson transition, where the diffusion constant scales like $(-i\omega)^{1/3}$, implying an anomalous diffusion $\langle r^2(t) \rangle \propto t^{2/3}$ at long times.

distribution along the lines of (63). Just as in 1d, the asymptotic decay is governed by the wave vector k_{\max} of the fastest atoms, and the density is predicted to be $\langle |\psi(r)|^2 \rangle \approx Cr^{-5/2} \exp\{-r/\xi_{\text{loc}}(k_{\max})\}$ [99].

7.4.3 $d = 3$

In 3d, the same short-distance regularization than in 2d is necessary, leading to the following implicit equation, valid in the limit $\omega\tau_l \ll 1$:¹²

$$\frac{D(\omega)}{D_B} + \frac{3}{\pi(kl)^2} \left(1 - \frac{\pi}{2} \sqrt{\frac{-3i\omega\tau_l}{D(\omega)/D_B}} \right) = 1. \quad (159)$$

The behavior of the solution, shown in Fig. 30, depends on the Ioffe-Regel parameter kl and defines three distinct regimes:

Diffusive regime: For $kl > (kl)_c = \sqrt{3/\pi}$, D/D_B tends to a constant value in the limit $\omega \rightarrow 0$, which means that the system behaves always diffusively, albeit with a diffusion constant smaller than the Boltzmann diffusion constant. This is the regime of weak localization.

Localized regime: For $kl < (kl)_c$, it is easy to see that $D/D_B \rightarrow 0$ in the limit $\omega \rightarrow 0$. More precisely, one has exponential localization:

$$D(\omega) \approx -i\omega\xi_{\text{loc}}^2 \quad \text{with} \quad \xi_{\text{loc}} \sim \frac{1}{(kl)_c - kl} \quad (160)$$

¹²This formula features only the static Cooperon contribution, which suffices for qualitative predictions, but should be extended to include the full interference terms appearing in (154) when quantitative precision is necessary.

immediately below the Anderson transition, on the insulating side. This means, see eq. (58), that the critical exponent deduced from the self-consistent approach is $\nu = 1$, quite far from the true value $\nu = 1.58$ known from numerical simulations [26]. The reason lies in the approximate character of the self-consistent approach, which disregards the huge fluctuations in the vicinity of the critical point. Field-theoretic approaches can in principle capture the effect of fluctuation and have been quantitatively tested in $d = 2 + \epsilon$ dimensions [15]. For $d = 3$, however, to our knowledge no analytical theory is available that makes a better quantitative prediction than the self-consistent theory.

Critical regime: At the critical point $kl = (kl)_c$, it is easy to see that the solution of eq. (159) scales like $D(\omega) \sim (-i\omega)^{1/3}$. Consequently, the critical behavior is anomalous diffusion where the squared extension increases subdiffusively at long times: $\langle r^2(t) \rangle \propto t^{2/3}$. This anomalous diffusion has been experimentally observed with the quasi-periodically kicked rotor, see Sec. 8.

8 Kicked rotor

The physics of Anderson localization is, as amply discussed in the preceding sections, highly dependent on the dimension of the system. While the 1d situation is fairly well understood—localization is the generic behavior, the localization length is comparable to the mean free path, and the fluctuation properties in the localized regime are essentially well understood—the physics of higher dimensions is much richer still. Dimension 3 is especially interesting, as one expects a so-called mobility edge, separating, in the continuum case, localized states at low energy/strong disorder from extended states at high energy/weak disorder.

As explained in Sec. 4.3, it is very difficult to find a clean experimental system to observe this metal-insulator Anderson transition unambiguously. Cold atomic matter waves are very attractive because they can be directly observed, and because most experimental imperfections as well as atom-atom interactions can be precisely controlled, if not reduced to a minimum. The main difficulty consists in reaching the Ioffe-Regel threshold $kl = O(1)$, eq. (57), i.e. preparing a sufficiently small k (low energy, large de Broglie wavelength) and short mean free path l . Indeed, the latter cannot be shorter than the correlation length of the disordered potential, i.e. of the order of $1 \mu\text{m}$ for optical speckle.

This limitation on the mean free path can be overcome using a different approach, where disorder is not provided by an external potential in configuration space, but by classically chaotic dynamics in momentum space. This idea has been realized experimentally with the atomic kicked rotor, and Anderson localization in 1d has been observed as early as 1994 [100], 14 years prior to the widely noticed Anderson localization in configuration space [4]! A key advantage of the kicked rotor is that it does not require ultra-cold atoms from a Bose-Einstein condensate: a standard magneto-optical trap suffices to prepare the initial state. The kicked rotor also has permitted the clean observation of the metal-insulator Anderson transition in 3D, and the first experimental measurement of the critical exponent, with non-interacting matter waves [101].

8.1 The classical kicked rotor

We consider a one-dimensional rotor whose position can be described by the angle x (defined modulo 2π) and the associated momentum p , and kick it periodically with a position-dependent amplitude. In properly scaled units, the Hamiltonian function can be written as

$$H = \frac{p^2}{2} - k \cos x \sum_{n=-\infty}^{+\infty} \delta(t - nT) \quad (161)$$

where T and k are period and strength of the kicks, respectively.

Because of the time-dependence, energy is not conserved, but thanks to the time-periodicity, we can analyze the motion stroboscopically and build a Poincaré map picturing the evolution once every period. This map relates the phase space coordinates just before kick $n + 1$ to the coordinates just before kick n :

$$\begin{cases} I_{n+1} = I_n + K \sin x_n \\ x_{n+1} = x_n + I_{n+1} \end{cases} \quad (162)$$

where $K = kT$ and $I_n = Tp_n$. This is nothing but the celebrated standard map (also known as the Chirikov map) that has been widely studied [102, 103]: it is almost fully chaotic and ergodic around $K = 10$ and above.

When the stochasticity parameter K is very large, each kick is so strong that the positions of the consecutive kicks can be taken statistically uncorrelated. By averaging, one thus gets:

$$\langle p_{n+1}^2 \rangle \simeq \langle p_n^2 \rangle + k^2 \langle \sin^2 x_n \rangle \simeq \langle p_n^2 \rangle + \frac{k^2}{2} \quad (163)$$

It follows that the motion in momentum space is diffusive ($\langle p^2 \rangle$ increases linearly with time) with diffusion constant

$$D = \frac{k^2}{2T}. \quad (164)$$

Numerical experiments [102] show that this expression works well for $K \geq 10$. Note that the kicked rotor is a perfectly deterministic system, without any randomness. It is the chaotic nature of the classical motion, and thus its extreme sensitivity to perturbations, which renders the deterministic classical motion diffusive *on average*.

8.2 The Quantum Kicked Rotor

The quantum Hamiltonian is obtained from the classical one, eq. (161), through the canonical replacement of p by $-i\hbar\partial_x$. The evolution operator over one period is the product of the free evolution operator and the instantaneous kick operator:

$$U = U(T, 0) = \exp\left(-\frac{i}{\hbar} \frac{p^2 T}{2}\right) \exp\left(\frac{i}{\hbar} k \cos x\right) \quad (165)$$

The long-time dynamics is generated by successive iterations of U . Thus, one can use the eigenstates of U as a basis set. U being unitary, its eigenvalues are complex numbers with unit modulus:

$$U|\phi_i\rangle = \exp\left(-\frac{iE_i T}{\hbar}\right) |\phi_i\rangle \quad (166)$$

with $0 < E_i \leq 2\pi\hbar/T$ are defined modulo $2\pi\hbar/T$. They are not exactly the energy levels of the system—the $|\phi_i\rangle$ are not stationary states of the time evolution, but are only periodic—and are called quasi-energy levels, the $|\phi_i\rangle$ being the Floquet eigenstates. This Floquet description is the time-analog of the Bloch theorem that applies to spatially periodic potentials.

8.3 Dynamical Localization

The quantum dynamics of the kicked rotor can be quite simply studied numerically by repeated application of the one-period evolution operator U to the initial state, alternating free propagation phases with instantaneous scattering events in momentum space induced by the kicks. The free evolution between kicks, $\exp(-ip^2T/2\hbar)$, is diagonal in momentum representation, such that each momentum eigenstate, characterized by its momentum $m\hbar$ with integer m , picks up a different phase shift. The kick operator $\exp(ik \cos \theta/\hbar)$, in contrast, is diagonal in position representation and couples different momenta. Being unitary, it plays the role of a scattering matrix in momentum space and contains the quantum amplitude for changing an incoming initial momentum in an outgoing one, under the influence of one kick; k is the parameter controlling the scattering strength. The dynamics of the kicked rotor can be seen as a sequence of scattering events interleaved with free propagation phases.

For sufficiently large $K = kT$, the classical dynamics is diffusive in momentum space, but it should come as no surprise to the reader now familiar with 1d Anderson localization, that the quantum dynamics may be localized at long times. This localization was baptized “dynamical localization” when it was observed in numerical simulations [104]. Only later, people realized that it is nothing but the Anderson scenario of 1d localization, as explained below.

Dynamical localization has been experimentally observed in the dynamics of a Rydberg electron exposed to an external microwave field [105]. Arguably the simplest observation uses a cold atomic gas, prepared in a standard magneto-optical trap with a typical velocity spread of few recoil velocities [100, 106, 101]. After the trap is switched off, a periodic train of laser pulses is applied to the atoms. Each pulse is composed of two far-detuned counter-propagating laser beams producing a spatially modulated optical potential. Each laser pulse thus produces a kick on the atom velocity, whose amplitude is proportional to the gradient of the optical potential.

If the kicks are infinitely short, we recover exactly the kicked rotor, eq. (161), where the position of the atom in the standing wave plays the role of the x variable and its velocity is the p variable. The kick strength k is proportional to the laser intensity divided by the detuning. The spatial dimensions perpendicular to the laser beams do not play any role in the problem, so that we have an effectively one-dimensional time-dependent problem. The mapping of the dimensionfull Hamiltonian for cold atoms to the kicked rotor Hamiltonian, eq. (161), shows that the effective Planck’s constant of the problem [107] is $\hbar_{\text{eff}} = 4\hbar k_L^2 T/M = 8\omega_r T$ where k_L is the laser wavenumber and M the atomic mass. Up to a numerical factor, it is the ratio of the atomic recoil frequency ω_r to the pulse frequency, and can be easily varied in the experiment, from the semiclassical regime $\hbar_{\text{eff}} \ll 1$ to the quantum regime $\hbar_{\text{eff}} \sim 1$.

After the series of pulses is applied, the momentum distribution is measured either by a time of flight technique [100] or velocity selective Raman transi-

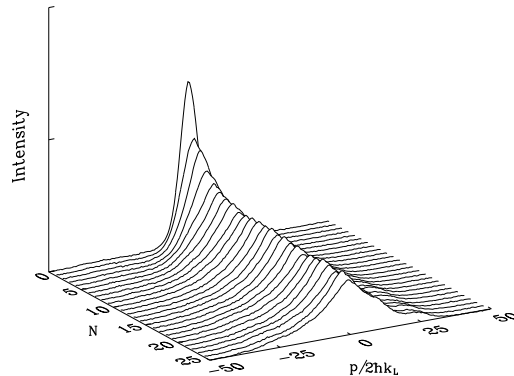


Figure 31: Experimental time evolution of the momentum distribution of the atomic kicked rotor [100], from the initial Gaussian distribution until the exponentially localized distribution at long time; N is the number of kicks (courtesy of M. Raizen).

tions [101]. Figure 31 shows the momentum distribution as a function of time. While, at short time, the distribution is Gaussian—as expected for a classical diffusion—, its shape changes around the localization time and evolves toward an exponential shape $\exp(-|p|/\xi_{\text{loc}})$ at long time, a clear-cut manifestation of Anderson/dynamical localization.

Adding decoherence on the system—either by adding spontaneous emission [106] or by weakly breaking the temporal periodicity [108]—induces some residual diffusion at long time, in accordance with the discussion in Sec. 6.3 and 7.4. This is another proof that dynamical localization is based on delicate destructive interference.

8.4 Link between dynamical and Anderson localizations

So far, we have only made plausible that dynamical localization with the quantum kicked rotor is similar to Anderson localization in a spatially disordered medium. We now demonstrate the connection between the two phenomena, following [109]. Consider the evolution operator, eq. (165), and the associated eigenstate $|\phi\rangle$ with quasi-energy E . The part of the evolution operator associated with the kick can be written as:

$$\exp\left(\frac{i}{\hbar} k \cos x\right) = \frac{1 + iW(x)}{1 - iW(x)} \quad (167)$$

where $W(x)$ is a periodic Hermitean operator which can be Fourier-expanded:

$$W(x) = \sum_{r=-\infty}^{\infty} W_r \exp(irx). \quad (168)$$

Similarly, the kinetic part can be written as:

$$\exp\left[-\frac{i}{\hbar} \left(\frac{p^2}{2} - E\right) T\right] = \frac{1 + iV}{1 - iV} \quad (169)$$

The operator V is diagonal in the eigenbasis of p , labeled by the integer m (see above). If one performs the following expansion in this basis set,

$$\frac{1}{1 - iW(x)}|\phi\rangle = \sum_m \chi_m |m\rangle, \quad (170)$$

it is straightforward to show that the eigenvalue-equation (166) can be rewritten as

$$\epsilon_m \chi_m + \sum_{r \neq 0} W_r \chi_{m-r} = -W_0 \chi_m \quad (171)$$

where

$$\epsilon_m = \tan \left[\left(E - \frac{1}{2} m^2 \hbar^2 \right) T / 2\hbar \right]. \quad (172)$$

Equation (171) is the time-independent Schrödinger equation for a one-dimensional Anderson model, cf. (68), with site index m , on-site energy ϵ_m , coupling W_r to the nearest sites and total energy W_0 . Compared to (68), there are two new ingredients: firstly, there are additional hopping amplitudes to other neighbors. But since they decrease sufficiently fast at large distance, they do not play a major role. Secondly, the ϵ_m values, determined deterministically by (172), are not really random variables, but only pseudo-random¹³ with a Lorentzian distribution.¹⁴ Still, localization is expected and indeed observed. The computation of the localization length follows the general lines explained in section 5, and is in good agreement with experimental observations.

It should be emphasized that space and time play different roles in the Anderson model and in dynamical localization. What plays the role of the sites of the Anderson model are the momentum states. This is why dynamical localization is not observed in configuration space, but in momentum space.

8.5 The quasi-periodically kicked rotor

How can the kicked rotor be used to study Anderson localization in more than one dimension? The first idea is to use a higher-dimensional rotor with a classically chaotic dynamics and to kick it periodically. It turns out that this is not easily realized experimentally, as it requires to build a specially crafted spatial dependence[110]. Yet, remember that time and space have switched roles, and so a simpler idea is to use additional temporal dimensions rather than spatial dimensions. Instead of kicking the system periodically with kicks of constant strength, one may use a temporally quasi-periodic excitation. Various schemes have been used [111], but the one allowing to map on a multi-dimensional Anderson model uses a quasi-periodic modulation of the kick strength, the kicks being applied at fixed time interval [112].

¹³As is well known, “random-number generators” implemented in computers also generate deterministic, merely pseudo-random sequences; most of them use formulae analogous to (172).

¹⁴The non-random character appears for example, when the product $\hbar T/2$ is chosen as an integer multiple of 2π . Then all ϵ_m are equal, the motion is ballistic and localization is absent. Similarly, when $\hbar T$ is commensurate with π (the so-called quantum resonances), the sequence ϵ_m becomes periodic, and Anderson localization does not take place, giving way to Bloch-band transport.

We will be interested in a 3d Anderson model, obtained by adding two quasi-periods to the system:¹⁵

$$\mathcal{H}_{\text{qp}} = \frac{p^2}{2} + \mathcal{K}(t) \cos x \sum_n \delta(t - n), \quad (173)$$

with

$$\mathcal{K}(t) = K [1 + \varepsilon \cos(\omega_2 t + \varphi_2) \cos(\omega_3 t + \varphi_3)]. \quad (174)$$

Now where is the three dimensional aspect in the latter Hamiltonian? The answer lies in a formal analogy between this quasi-periodic kicked rotor and a 3d kicked rotor with the special initial condition of a “plane source”, as follows.

Take the Hamiltonian of a 3d, periodically kicked rotor:

$$\mathcal{H} = \frac{p_1^2}{2} + \omega_2 p_2 + \omega_3 p_3 + K \cos x_1 [1 + \varepsilon \cos x_2 \cos x_3] \sum_n \delta(t - n), \quad (175)$$

and consider the evolution of a wavefunction Ψ with the initial condition

$$\Psi(x_1, x_2, x_3, t = 0) \equiv \psi(x_1, t = 0) \delta(x_2 - \varphi_2) \delta(x_3 - \varphi_3). \quad (176)$$

This initial state, perfectly localized in x_2 and x_3 and therefore entirely delocalized in the conjugate momenta p_2 and p_3 , is a “plane source” in momentum space [98]. A simple calculation shows that the stroboscopic evolution of Ψ under (175) coincides exactly with the evolution of the initial state $\psi(x = x_1, t = 0)$ under the Hamiltonian (173) of the quasi-periodically kicked rotor (for details, see [107]). An experiment with the quasi-periodic kicked rotor can thus be seen as a localization experiment in a 3d disordered system, where localization is actually observed in the direction perpendicular to the plane source. In other words, the situation is comparable to a transmission experiment where the sample is illuminated by a plane wave and the exponential localization is only measured along the wave vector direction. Therefore, the behavior of the quasi-periodic kicked rotor (173) matches *all* dynamic properties of the quantum 3d kicked rotor.

The classical dynamics has been shown to be a chaotic diffusion, provided the parameter ε is sufficiently large to ensure efficient coupling between the 3 degrees of freedom [113]. As for the standard 3d kicked rotor (175), its quantum dynamics can be studied using the Floquet states via mapping to a 3d Anderson-like model:

$$\epsilon_{\mathbf{m}} \Phi_{\mathbf{m}} + \sum_{\mathbf{r} \neq 0} W_{\mathbf{r}} \Phi_{\mathbf{m}-\mathbf{r}} = -W_{\mathbf{0}} \Phi_{\mathbf{m}}, \quad (177)$$

where $\mathbf{m} \equiv (m_1, m_2, m_3)$ labels sites in a 3d cubic lattice, the on-site energy $\epsilon_{\mathbf{m}}$ is

$$\epsilon_{\mathbf{m}} = \tan \left\{ \frac{1}{2} \left[\omega - \left(\hbar \frac{m_1^2}{2} + \omega_2 m_2 + \omega_3 m_3 \right) \right] \right\}, \quad (178)$$

and the hopping amplitudes $W_{\mathbf{r}}$ are the Fourier expansion coefficients of

$$W(x_1, x_2, x_3) = \tan [K \cos x_1 (1 + \varepsilon \cos x_2 \cos x_3) / 2\hbar]. \quad (179)$$

¹⁵In this section, we take the kicking period T as unit of time

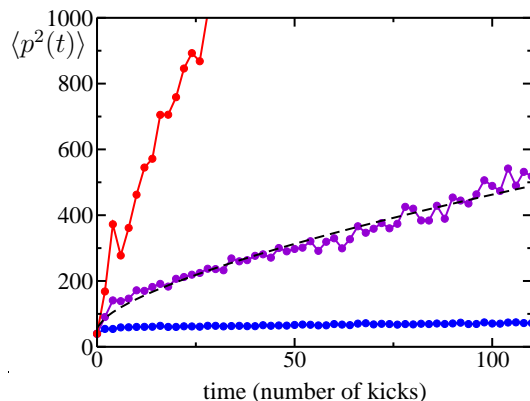


Figure 32: Experimentally measured temporal dynamics of the quasi-periodically kicked rotor, for increasing values of the kick strength. The average kinetic energy $\langle p^2(t) \rangle$ tends to a constant in the localized regime (lower curve, $K = 4$, $\varepsilon = 0.1$), increases linearly with time in the diffusive regime (upper curve, $K = 9$, $\varepsilon = 0.8$). At the critical point $K = K_c \approx 6.4$ (middle curve), anomalous diffusion $\langle p^2(t) \rangle \sim t^{2/3}$ (dashed curve) is clearly observed.

A necessary condition for localization is obviously that $\epsilon_{\mathbf{m}}$ not be periodic. This is achieved if $(\hbar, \omega_2, \omega_3, \pi)$ are incommensurate. When these conditions are verified, localization effects as predicted for the 3d Anderson model are expected, namely either a diffusive or a localized regime. Localized states would be observed if the disorder strength is large compared to the hopping. In the case of the model (177), the amplitude of the disorder is fixed, but the hopping amplitudes can be controlled by changing the stochasticity parameter K (and/or the modulation amplitude ε): $W_{\mathbf{r}}$ is easily seen to increase with K . In other words, the larger K , the smaller the disorder. One thus expects to observe diffusion for large stochasticity K and/or modulation amplitude ε (small disorder) and localization for small K and/or ε (large disorder). It should be emphasized that *stricto sensu* there is no mobility edge in our system that would separate localized from delocalized eigenstates. Depending on the parameters $K, \hbar, \varepsilon, \omega_2, \omega_3$, either *all* Floquet states are localized or all are delocalized. The boundary of the metal-insulator transition is in the $(K, \hbar, \varepsilon, \omega_2, \omega_3)$ -parameter space. As seen below, K and ε are the primarily important parameters.

In the experiment performed at the University of Lille [101], kicks are applied to atoms with an initially narrow momentum distribution, and the final momentum distribution is measured using velocity-selective Raman transitions.¹⁶ Figure 32 shows the experimental data. For large disorder, one clearly sees the initial diffusive phase and the freezing of the quantum dynamics in the localized regime (lower curve). In the diffusive regime (upper curve), $\langle p^2(t) \rangle$ is seen to increase linearly with time. The intermediate curve displays an anomalous

¹⁶Measuring the average $\langle p^2(t) \rangle$ is tedious and very sensitive to noise in the wings of the momentum distribution. It is much easier to measure the atomic population $\Pi_0(t)$ at zero momentum. Because of atom number conservation, $\langle p^2(t) \rangle$ is roughly proportional to $1/\Pi_0^2(t)$. The proportionality factor depends on the shape of the distribution, but does not show large changes. As we are interested in scaling properties, $1/\Pi_0^2(t)$ or $\langle p^2(t) \rangle$ are essentially equivalent.

diffusion $\langle p^2(t) \rangle \sim t^{2/3}$. The anomalous exponent $2/3$ is exactly the prediction of the self-consistent theory of localization, section 7.4.3, which also fully agrees with the scaling theory of localization. Time here plays the role of the system size L in the scaling theory: going to longer times means following the renormalization flow in fig. 7. Only exactly at the unstable critical point will the anomalous diffusion subsist for arbitrarily long times. At slightly larger (resp. smaller) K , the motion will eventually turn diffusive (resp. localized) at long time. Experimental constraints prevent the observation beyond 150-200 kicks. Numerical simulations may extend much beyond: it has been checked that the anomalous diffusion with exponent $2/3$ is followed for at least 10^8 kicks [107].

Since in numerical or experimental practice one always works in finite-size systems, we should emphasize that there is an important difference between a true metal-insulator transition and a cross-over between two limiting behaviors. For example, consider the simplest 1d situation where the dynamics eventually localizes for sure, with a localization time depending on the kick strength K . Over a finite experimental time, one may observe an apparently diffusive behavior if the localization time is longer than the duration of the experiment.¹⁷ An intermediate situation with the localization time comparable to the duration of the experiment could produce data looking like anomalous diffusion. However, this could be only a transient behavior and a longer measurement will eventually show localization. In contrast, the $t^{2/3}$ behavior at the critical point of the Anderson transition is not a transient behavior, it extends to infinity, highlighting the scale-free behavior with fluctuations of all sizes present right at the critical point.

The unavoidable experimental limitation by finite size can also be turned into a powerful tool of analysis. It is known as finite-size scaling [38] and has its roots in the scaling properties observed in the vicinity of the transition. The idea is that all results, obtained for various values of parameters and time, are described by a universal scaling law depending on a single parameter, namely, the distance to the critical manifold. Close to the transition, there is only one characteristic length (which diverges at the critical point) and all details below this scale are irrelevant. Such an approach has been extremely successful to extract critical parameters from numerical simulations of the Anderson model for various system sizes. The approach has been transposed to the kicked rotor—see [107, 114] for details—and makes it possible to extract the localization length (in momentum space) from numerical or experimental data acquired over a restricted time interval.

The results are shown in Fig. 33 for both numerical simulations and experimental observations. One clearly sees the divergence of the characteristic length (the localization length on the insulator side) in the vicinity of the transition. The divergence is smoothed by experimental imperfections and the finite duration of numerical and real experiments. The smoothing is much more important in the latter case than in the former one, because the duration of the real experiment (110 kicks maximum) is about 4 orders of magnitude shorter than in

¹⁷This also occurs for 1d Anderson localization in a speckle potential [4], as already pointed out in Sec. 5.2.4: Because the localization length and time vary rapidly with energy, one observes localization at low energy and apparently diffusive behavior at high energy. In between, an apparent mobility edge appears [20], which should not be confounded with the true Anderson metal-insulator transition taking place in the thermodynamic limit, although the experimental signatures may be similar.

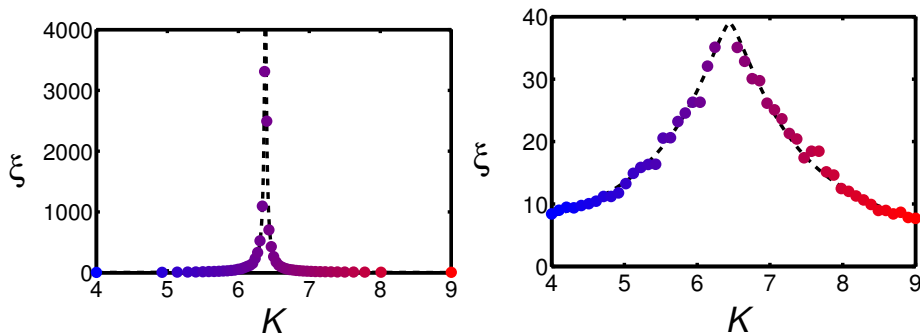


Figure 33: Characteristic length (for localization in momentum space) extracted from numerical (left) and real (right) experiments on the quasi-periodically kicked rotor, in the vicinity of the metal-insulator Anderson transition [101]. Finite-size scaling is used. The characteristic length is proportional to the localization length on the insulating side, and to the inverse of the diffusion constant on the metallic side. It has an algebraic divergence $1/|K - K_c|^\nu$ at the transition, smoothed by finite size and decoherence, which are more important in the real experiment (limited to 110 kicks) than in the numerical calculations (up to one million kicks). In both cases, it is possible to extract a rather precise estimate of the critical exponent $\nu \approx 1.5$.

numerical experiments. It is nevertheless possible to extract the critical exponent of the transition. For the numerical experiments, one finds $\nu = 1.58 \pm 0.01$ in perfect agreement with the best determination on the Anderson model. Moreover, it has been checked that this exponent is universal, i.e. independent of the microscopic details such as the choice of the parameters $\hbar, \omega_2, \omega_3$ [27]. This is an additional confirmation that the transition observed is actually the metal-insulator Anderson transition.

The critical exponent can also be determined—albeit with reduced accuracy—from the experimental data [101]. For the data of Fig. 33, one obtains:

$$\nu_{\text{exp}} = 1.4 \pm 0.3 \quad (180)$$

These values are in excellent agreement with the numerical results. The key point is that the exponent significantly differs from unity, which is the value deduced from solid state measurements, see Fig. 15, and the prediction of the self-consistent approach.

Since the atom-atom contact interaction in a cold dilute gas is much smaller than the electron-electron Coulomb interaction in a solid sample, and since atoms are less easily lost than photons, cold atoms appear particularly suitable for precise measurements of the Anderson transition. Moreover, the possibility to picture wave functions directly opens the way to studies of fluctuations in the vicinity of the critical point [113], and may even permit to observe multifractal behavior [47] with matter waves. The flexibility of the kicked rotor could also be used to study the Anderson transition in lower dimensions (by reducing the number of quasi-periods) or, why not, even higher dimensions (by increasing it beyond 3). In any case, it is an attractive alternative to experiments on spatially disordered systems.

References

- [1] N. Goldenfeld and L. P. Kadanoff, “Simple Lessons from Complexity”, *Science*, **284**, 87 (1999).
- [2] P. W. Anderson, “More Is Different”, *Science*, **177**, 393 (1972).
- [3] W. Thirring, “Exact results for the scattering of three charged particles”, in *Few Body Systems and Nuclear Forces II*, Lect. Notes Phys. **78**, 353-361 (Springer, 1978).
- [4] J. Billy, V. Josse, Z. Zuo, A. Bernard, B. Hambrecht, P. Lugan, D. Clément, L. Sanchez-Palencia, Ph. Bouyer and A. Aspect, “Direct observation of Anderson localization of matter waves in a controlled disorder”, *Nature* **453**, 891-894 (12 June 2008); Ph. Bouyer *et al.*, “Anderson localization of matter waves”, Proceedings of the XXI ICAP Conference, R. Coté, Ph. L. Gould, M. Rozman and W. W. Smith eds., World Scientific (2008).
- [5] P. W. Anderson, “Absence of Diffusion in Certain Random Lattices”, *Phys. Rev.* **109**, 1492 (1958).
- [6] P. A. Mello and N. Kumar, *Quantum Transport in Mesoscopic Systems: Complexity and Statistical Fluctuations* (Oxford, 2004).
- [7] Y. Imry, *Introduction to mesoscopic physics* (Oxford University Press, 2002).
- [8] S. Datta, *Electronic transport in mesoscopic systems* (Cambridge University Press, 2002).
- [9] C. W. J. Beenakker, “Random matrix theory of quantum transport”, *Rev. Mod. Phys.* **69**, 731 (1997).
- [10] P. A. Mello, “Theory of Random Matrices: Spectral Statistics and Scattering Problems”, in: E. Akkermans et al. (eds), *Mesoscopic Quantum Physics*, Les Houches 1994 Session LXI (North-Holland, Elsevier, 1995).
- [11] S. Godoy, “Landauer diffusion coefficient: A classical result”, *Phys. Rev. E* **56**, 4884 (1997).
- [12] H. Furstenberg, “Noncommuting Random Products”, *Trans. Am. Math. Soc.* **108**, 377 (1963).
- [13] N. G. van Kampen, *Stochastic Processes in Physics and Chemistry*, (Elsevier, Amsterdam, 2007).
- [14] A. A. Abrikosov, “The paradox with the static conductivity of a one-dimensional metal”, *Solid State Comm.* **37**, 997 (1981).
- [15] F. Evers and A. D. Mirlin, “Anderson Transitions”, *Rev. Mod. Phys.* **80**, 1355 (2008).
- [16] L. P. Kadanoff et al., “Static Phenomena Near Critical Points: Theory and Experiment”, *Rev. Mod. Phys.* **39**, 395 (1967).

- [17] K. G. Wilson, “The renormalization group and critical phenomena”, *Rev. Mod. Phys.* **55**, 583 (1983).
- [18] F. Wegner, “Electrons in disordered systems. Scaling near the mobility edge”, *Z. Phys. B* **25**, 327 (1976).
- [19] E. Abrahams, P. W. Anderson, D. C. Licciardello and T. V. Ramakrishnan, “Scaling Theory of Localization: Absence of Quantum Diffusion in Two Dimensions”, *Phys. Rev. Lett.* **42**, 673 (1979).
- [20] P. Lugan, A. Aspect, L. Sanchez-Palencia, D. Delande, B. Grémaud, C.A. Müller and C. Miniatura, “One-dimensional Anderson localization in certain correlated random potentials”, *Phys. Rev. A* **80**, 023605 (2009).
- [21] E. Gurevich and O. Kenneth, “Lyapunov exponent for the laser speckle potential: A weak disorder expansion”, *Phys. Rev. A* **79**, 063617 (2009).
- [22] P. W. Anderson, D. J. Thouless, E. Abrahams, and D. S. Fisher, “New method for a scaling theory of localization”, *Phys. Rev. B* **22**, 3519 (1980).
- [23] R. Landauer, “Electrical resistance of disordered one-dimensional lattices”, *Phil. Mag.* **21**, 863 (1970).
- [24] M. E. Peskin and D. S. Schroeder, *An Introduction to Quantum Field Theory* (Addison-Wesley, 1995).
- [25] Y. Lahini, R. Pugatch, F. Pozzi, M. Sorel, R. Morandotti, N. Davidson and Y. Silberberg, “Direct observation of a localization transition in quasi-periodic photonic lattices”, *Phys. Rev. Lett.* **103**, 013901 (2009).
- [26] K. Slevin and T. Ohtsuki, “Corrections to Scaling at the Anderson Transition”, *Phys. Rev. Lett.* **82**, 382 (1999).
- [27] G. Lemarié, B. Grémaud and D. Delande, “Universality of the Anderson transition with the quasiperiodic kicked rotor”, *Europhys. Lett.* **87**, 37007 (2009).
- [28] L. Sanchez-Palencia, D. Clément, P. Lugan, P. Bouyer, G. V. Shlyapnikov, A. Aspect, “Anderson Localization of Expanding Bose-Einstein Condensates in Random Potentials”, *Phys. Rev. Lett.* **98**, 210401 (2007).
- [29] M. V. Berry and S. Klein, “Transparent mirrors: rays, waves and localization”, *Eur. J. Phys.* **18**, 222 (1997).
- [30] A.Z. Genack and A.A. Chabanov, “Signatures of photon localization”, *J. Phys. A: Math. Gen.* **38**, 10465 (2005).
- [31] A. A. Chabanov, M. Stoytchev and A. Z. Genack, “Statistical signatures of photon localization”, *Nature* **404**, 850 (2000).
- [32] A. A. Chabanov and A. Z. Genack, “Photon localization in resonant media”, *Phys. Rev. Lett.* **87**, 153901 (2001).
- [33] J.M. Luck, “Systèmes désordonnés unidimensionnels”, Commissariat à l’énergie atomique (1992), in french.

- [34] R.C. Kuhn, O. Sigwarth, C. Miniatura, D. Delande, C.A. Müller, “Coherent Matter Wave Transport in Speckle Potentials” [New J. Phys. **9**, 161 \(2007\)](#) .
- [35] S.V. Kravchenko, G.V. Kravchenko, J.E. Furneaux, V.M. Pudalov and M. D’Iorio, “Possible metal-insulator transition at $B = 0$ in two dimensions”, [Phys. Rev. B **50**, 8039 \(1994\)](#).
- [36] D. Belitz and T. R. Kirkpatrick, “The Anderson-Mott-transition”, [Rev. Mod. Phys. **66**, 261 \(1994\)](#).
- [37] T. Schwartz, G. Bartal, S. Fishman and M. Segev, “Transport and Anderson localization in disordered two-dimensional photonic lattices”, [Nature **446**, 52-55 \(2007\)](#).
- [38] M.E. Fisher and M.N. Barber, “Scaling Theory for Finite-Size Effects in the Critical Region”, [Phys. Rev. Lett. **28**, 1516 \(1972\)](#).
- [39] A. MacKinnon and B. Kramer, “One-Parameter Scaling of Localization Length and Conductance in Disordered Systems”, [Phys. Rev. Lett. **47**, 1546 \(1981\)](#).
- [40] S. Katsumoto, F. Komori, N. Sano and S. Kobayashi, “Fine tuning of metal-insulator transition in $\text{Al}_{0.3}\text{Ga}_{0.7}\text{As}$ using persistent photoconductivity”, [J. Phys. Soc. Jap. **56**, 2259 \(1987\)](#).
- [41] M. Greiner et al., “Quantum phase transition from a superfluid to a Mott insulator in a gas of ultracold atoms”, [Nature **415**, 39 \(2002\)](#).
- [42] H. Hu, A. Strybulevych, J.H. Page, S.E. Skipetrov and B.A. van Tiggelen, “Localization of ultrasound in a three-dimensional elastic network”, [Nature Physics **4**, 945 \(2008\)](#).
- [43] D.S. Wiersma, P. Bartolini, A. Lagendijk and R. Righini, “Localization of light in a disordered medium”, [Nature **390**, 671, \(1997\)](#).
- [44] F. Scheffold, R. Lenke, R. Tweer, G. Maret, “Localization or classical diffusion of light?” [Nature **398**, 206, \(1999\)](#).
- [45] M. Störzer, P. Gross, G.M. Aegerter and G. Maret, “Observation of the Critical Regime Near Anderson Localization of Light”, [Phys. Rev. Lett. **96**, 063904 \(2006\)](#).
- [46] A.Z. Genack, “Statistical approach to photon localization” in *Waves and Imaging through complex media*, P. Sebbah (ed.) (Kluwer, 2001).
- [47] S. Faez, A. Strybulevych, J.H. Page, A. Lagendijk and B.A. van Tiggelen, “Observation of multifractality at the Anderson localization transition of ultrasound in open three-dimensional media”, [Phys. Rev. Lett. **103**, 155703 \(2009\)](#).
- [48] K.B. Efetov, “Supersymmetry and theory of disordered metals”, [Advances in Physics **32**, 53 \(1983\)](#).

- [49] H. Bruus and K. Flensberg, *Many-Body Quantum Theory in Condensed Matter Physics* (Oxford University Press, 2004).
- [50] J. W. Negele and H. Orland, *Quantum Many-Particle Systems* (Westview Press, 1998).
- [51] G. D. Mahan, *Many-Particle Physics* (Kluwer, 2000).
- [52] A. Altland and B. Simons, *Condensed Matter Field Theory* (Cambridge University Press, 2006).
- [53] M. Hartung, T. Wellens, C. A. Müller, K. Richter, and P. Schlagheck, “Coherent backscattering of Bose-Einstein condensates in two-dimensional disorder potentials”, *Phys. Rev. Lett.* **101**, 020603 (2008).
- [54] D. Clément, A.F. Varón, J.A. Retter, L. Sanchez-Palencia, A. Aspect, P. Bouyer, “Experimental study of the transport of coherent interacting matter-waves in a 1D random potential induced by laser speckle”, *New J. Phys.* **8**, 165 (2006) .
- [55] L. Allen and J. H. Eberly, *Optical resonance and two-level atoms* (Dover Publications, New York, 1987).
- [56] C. Gaul, N. Renner, and C. A. Müller, “Speed of sound in disordered Bose-Einstein condensates”, *Phys. Rev. A* **80**, 053620 (2009). C. Gaul, and C. A. Müller, “Bogoliubov excitations of disordered Bose-Einstein condensates”, *Phys. Rev. A* **83**, 063629 (2011).
- [57] D. J. Thouless, “Localization distance and mean free path in one-dimensional disordered systems”, *J. Phys C.:Solid State Phys.* **6**, L49 (1973).
- [58] S. Kotani and B. Simon, “Localization in general one-dimensional random systems”, *Commun. Math. Phys.* **112**, 103 (1987).
- [59] F. A. B. F. de Moura and M. L. Lyra, “Delocalization in the 1D Anderson model with long-range correlated disorder”, *Phys. Rev. Lett.* **81**, 3735 (1998).
- [60] F. M. Izrailev and N. M. Makarov, “Anomalous transport in low-dimensional systems with correlated disorder”, *J. Phys. A: Math. Gen.* **38**, 10613 (2005).
- [61] J. S. Langer and T. Neal, “Breakdown of the concentration expansion for the impurity resistivity of metals”, *Phys. Rev. Lett.* **16**, 984 (1966).
- [62] P. M. Morse and H. Feshbach, *Methods of Theoretical Physics* (McGraw-Hill, 1953).
- [63] T. M. Nieuwenhuizen and J. M. Luck, “Skin layer of diffusive media”, *Phys. Rev. E* **48**, 569-588 (1993).
- [64] A. Ishimaru, *Wave Propagation and Scattering in Random Media* (Academic, New York, 1978), Vols. I and II.

- [65] Y. Kuga and A. Ishimaru, “Retroreflectance from a dense distribution of spherical particles”, *J. Opt. Soc. Am. A* **1**, 831-835 (1984).
- [66] M. P. van Albada and A. Lagendijk , “Observation of Weak Localization of Light in a Random Medium”, *Phys. Rev. Lett.* **55**, 2692 (1985).
- [67] P. E. Wolf and G. Maret, “Weak Localization and Coherent Backscattering of Photons in Disordered Media”, *Phys. Rev. Lett.* **55**, 2696 (1985).
- [68] E. Akkermans and G. Montambaux, *Mesoscopic Physics of Electrons and Photons*, (Cambridge University Press, 2007).
- [69] B. A. van Tiggelen, *Multiple Scattering and Localization of Light*, PhD thesis, University of Amsterdam (1992).
- [70] C. A. Müller, T. Jonckheere, C. Miniatura and D. Delande, “Weak localization of light by cold atoms: the impact of quantum internal structure”, *Phys. Rev. A* **64**, 053804 (2001).
- [71] Y. Bidet, B. Klappauf, J.-C. Bernard, D. Delande, G. Labeyrie, C. Miniatura, D. Wilkowski and R. Kaiser, “Coherent light transport in a cold strontium cloud”, *Phys. Rev. Lett.* **88**, 203902 (2002).
- [72] C. A. Müller and C. Miniatura “Multiple scattering of light by atoms with internal degeneracy”, *J. Phys. A: Math. Gen.* **35**, 10163 (2002).
- [73] D. S. Wiersma, M. P. van Albada, B. A. van Tiggelen and A. Lagendijk, “Experimental Evidence for Recurrent Multiple Scattering Events of Light in Disordered Media”, *Phys. Rev. Lett.* **74**, 4193 (1995).
- [74] A. A. Golubentsev, “Suppression of interference effects in multiple scattering of light”, *JETP* **59**, 26 (1984).
- [75] G. Labeyrie, D. Delande, R. Kaiser, and C. Miniatura, “Light Transport in Cold Atoms and Thermal Decoherence”, *Phys. Rev. Lett.* **97**, 013004 (2006).
- [76] W. M. Itano, J. C. Bergquist, J. J. Bollinger, D. J. Wineland, U. Eichmann, M. G. Raizen, “Complementarity and Youngs interference fringes from two atoms”, *Phys. Rev. A* **57**, 4176 (1998).
- [77] C. Wickles and C.A. Müller, “Thermal breakdown of coherent backscattering: a case study of quantum duality”, *Europhys. Lett.* **74**, 240 (2006).
- [78] T. Chanelière, D. Wilkowski, Y. Bidet, R. Kaiser, and C. Miniatura, “Saturation-induced coherence loss in coherent backscattering of light”, *Phys. Rev. E* **70**, 036602 (2004).
- [79] V. Shatokhin, T. Wellens, C. A. Müller, A. Buchleitner, “Coherent backscattering of light from saturated atoms”, *Eur. Phys. J. Special Topics* **151**, 51 (2007).
- [80] V. Shatokhin, T. Wellens, B. Grémaud, A. Buchleitner, “Spectrum of coherently backscattered light from two atoms”, *Phys. Rev. A* **76**, 043832 (2007).

- [81] O. Assaf and E. Akkermans, “Intensity Correlations and Mesoscopic Fluctuations of Diffusing Photons in Cold Atoms”, [Phys. Rev. Lett. **98**, 083601 \(2007\)](#); [Phys. Rev. Lett. **100**, 199302 \(2008\)](#).
- [82] B. Grémaud, D. Delande, C. A. Müller, C. Miniatura, “Comment on ‘Intensity correlations and mesoscopic fluctuations of diffusing photons in cold atoms’”, [Phys. Rev. Lett. **100**, 199301 \(2008\)](#).
- [83] C. A. Müller, C. Miniatura, E. Akkermans, G. Montambaux, “Mesoscopic scattering of spin s particles”, [J. Phys. A: Math. Gen. **35**, 10163 \(2002\)](#).
- [84] G. Labeyrie, D. Delande, C.A. Müller, C. Miniatura, and R. Kaiser, “Coherent backscattering of light by cold atoms: Theory meets experiment”, [Europhys. Lett. **61**, 327 \(2003\)](#).
- [85] T. Jonckheere, C. A. Müller, R. Kaiser, C. Miniatura, D. Delande, “Multiple scattering of light by atoms in the weak localization regime”, [Phys. Rev. Lett. **85**, 4269 \(2000\)](#).
- [86] B.-G. Englert, “Fringe visibility and which-way information: an inequality”, [Phys. Rev. Lett. **77**, 2154 \(1996\)](#).
- [87] C. Miniatura, C. A. Müller, Y. Lu, G. Wang, B.-G. Englert, “Path Distinguishability in Double Scattering of Light by Atoms”, [Phys. Rev. A **76**, 022101 \(2007\)](#).
- [88] O. Sigwarth, G. Labeyrie, T. Jonckheere, D. Delande, R. Kaiser, and C. Miniatura, “Magnetic field enhanced coherence length in cold atomic gases”, [Phys. Rev. Lett. **93**, 143906 \(2004\)](#).
- [89] S. Washburn and R. Webb, “Aharonov-Bohm effect in normal metal: Quantum coherence and transport”, [Adv. Phys. **35**, 375 \(1986\)](#).
- [90] F. Pierre and N.O. Birge, “Dephasing by extremely dilute magnetic impurities revealed by Aharonov-Bohm oscillations”, [Phys. Rev. Lett. **89**, 206804 \(2002\)](#).
- [91] G. Bergmann, “Weak localization in thin films”, [Phys. Rep. **107**, 1 \(1984\)](#).
- [92] C. A. Müller, “Diffusive spin transport”, in: A. Buchleitner, C. Viviescas, and M. Tiersch (Eds.), *Entanglement and Decoherence. Foundations and Modern Trends*, [Lect. Notes Phys. **768**, 277-314 \(Springer, 2009\)](#).
- [93] F. Pierre, A.B. Gougam, A. Anthore, H. Pothier, D. Estève, and N. Birge, “Dephasing of electrons in mesoscopic metal wires”, [Phys. Rev. B **68**, 085413 \(2003\)](#).
- [94] L. P. Gor’kov, A. I. Larkin, and D. E. Khmel’nitskiĭ, [Pis’ma Zh. Eksp. Teor. Fiz. **30**, 248 \(1979\) \[JETP Lett. **30**, 228 \(1979\)\]](#).
- [95] D. Vollhardt and P. Wölfle, “Diagrammatic, self-consistent treatment of the Anderson localization problem in $d \leq 2$ dimensions”, [Phys. Rev. B **22**, 4666 \(1980\)](#).

- [96] D. Vollhardt and P. Wölfle, “Scaling equations from a self-consistent theory of Anderson localization”, *Phys. Rev. Lett.* **48**, 699 (1982).
- [97] D. Vollhardt and P. Wölfle, “Self-consistent theory of Anderson localization”, in: W. Hanke and Y. V. Kopayev, editors, *Electronic phase transitions* (Elsevier, Amsterdam, 1992).
- [98] O.I. Lobkis and R.L. Weaver, “Self-consistent transport dynamics for localized waves”, *Phys. Rev. E* **71**, 011112 (2005).
- [99] C. Miniatura, R.C. Kuhn, D. Delande, C. A. Müller, “Quantum diffusion of matter waves in 2D speckle potentials”, *Eur. Phys. J. B* **68**, 353 (2009).
- [100] F.L. Moore, J.C. Robinson, C. Bharucha, P.E. Williams and M.G. Raizen, “Observation of Dynamical Localization in Atomic Momentum Transfer: A New Testing Ground for Quantum Chaos”, *Phys. Rev. Lett.* **73**, 2974 (1994); F. L. Moore, J. C. Robinson, C. F. Bharucha, B. Sundaram, and M. G. Raizen, “Atom Optics Realization of the Quantum δ -Kicked Rotor”, *Phys. Rev. Lett.* **75**, 4598 (1995).
- [101] J. Chabé, G. Lemarié, B. Grémaud, D. Delande, P. Szriftgiser and J.C. Garreau, “Experimental observation of the Anderson metal-insulator transition with atomic matter waves”, *Phys. Rev. Lett.* **101**, 255702 (2008).
- [102] A.J. Lichtenberg and M.A. Lieberman, *Regular and stochastic motion*, Springer-Verlag, New-York (1983).
- [103] G. Casati, I. Guarneri and D. Shepelyansky, “Classical chaos, quantum localization and fluctuations: A unified view”, *Physica A* **163**, 205 (1990) and references therein.
- [104] G. Casati, B.V. Chirikov, J. Ford and F.M. Izrailev, “Stochastic Behavior of Classical and Quantum Hamiltonian Systems”, *Lecture Notes in Physics*, **334**, G. Casati and J. Ford eds., Springer, New York (1979).
- [105] A. Buchleitner, D. Delande and J.C. Gay, “Microwave ionization of 3-d hydrogen atoms in a realistic numerical experiment”, *J. Opt. Soc. Am. B* **12**, 505 (1995).
- [106] H. Ammann, R. Gray, I. Shvarchuck and N. Christensen, “Quantum Delta-Kicked Rotor: Experimental Observation of Decoherence”, *Phys. Rev. Lett.* **80**, 4111 (1998).
- [107] G. Lemarié, J. Chabé, P. Szriftgiser, J.C. Garreau, B. Grémaud and D. Delande, “Observation of the Anderson Metal-Insulator Transition with Atomic Matter Waves: Theory and Experiment”, *Phys. Rev. A* **80**, 043626 (2009).
- [108] B.G. Klappauf, W.H. Oskay, D.A. Steck and M.G. Raizen, “Observation of Noise and Dissipation Effects on Dynamical Localization”, *Phys. Rev. Lett.* **81**, 1203 (1998).
- [109] D.R. Grempel, R.E. Prange and S. Fishman, “Quantum dynamics of a nonintegrable system”, *Phys. Rev. A* **29**, 1639 (1984).

- [110] J. Wang and A.M. Garcia-Garcia, “The Anderson transition in a 3d kicked rotor”, *Phys. Rev. E* **79**, 036206 (2009).
- [111] H. Lignier, J. Chabé, D. Delande, J.C. Garreau and P. Szriftgiser, “Reversible destruction of dynamical localization”, *Phys. Rev. Lett.* **95**, 234101 (2005).
- [112] G. Casati, I. Guarneri and D.L. Shepelyansky, “Anderson transition in a one-dimensional system with three incommensurable frequencies”, *Phys. Rev. Lett.* **62**, 345 (1989).
- [113] G. Lemarié, H. Lignier, D. Delande, P. Szriftgiser and J.C. Garreau, “Critical State of the Anderson Transition: Between a Metal and an Insulator”, *Phys. Rev. Lett.* **105**, 090601 (2010).
- [114] G. Lemarié, “Transition d’Anderson avec des ondes de matière atomiques”, PhD thesis, Université Pierre et Marie Curie, Paris (2009), <http://tel.archives-ouvertes.fr/tel-00424399/fr/>